12-2021

Investigation of Mirror Satellite Concept to Augment Natural Lighting Conditions on Orbit

Daniel M. Dombrowski

INVESTIGATION OF MIRROR SATELLITE CONCEPT TO AUGMENT NATURAL LIGHTING CONDITIONS ON ORBIT

THESIS

Daniel Dombrowski, Second Lieutenant, USAF

AFIT-ENY-MS-21-D-065

DEPARTMENT OF THE AIR FORCE
AIR UNIVERSITY

AIR FORCE INSTITUTE OF TECHNOLOGY

Wright-Patterson Air Force Base, Ohio

AFIT-ENY-MS-21-D-065

INVESTIGATION OF MIRROR SATELLITE CONCEPT TO AUGMENT NATURAL LIGHTING CONDITIONS ON ORBIT

THESIS

Presented to the Faculty

Department of Aeronautics and Astronautics

Graduate School of Engineering and Management

Air Force Institute of Technology

Air University

Air Education and Training Command

In Partial Fulfillment of the Requirements for the

Degree of Master of Science in Astronautical Engineering

Daniel Dombrowski, BS

Second Lieutenant, USAF

December 2021

AFIT-ENY-MS-21-D-065

INVESTIGATION OF MIRROR SATELLITE CONCEPT TO AUGMENT NATURAL LIGHTING CONDITIONS ON ORBIT

Daniel Dombrowski, BS

Second Lieutenant, USAF

Approved:

_____	_____
Robert Bettinger, Maj, USAF (Chairman)	Date
_____	_____
Dr. Andrew Keys, Civ, USAF (Member)	Date
_____	_____
David Meyer, Civ, USAF (Member)	Date

Abstract

A method of augmenting on orbit lighting conditions for rendezvous and proximity operations through the use of solar reflectors is presented. Proximity operations are a necessity in the evolution of space servicing and inspection missions. Natural lighting conditions subject these complex missions to considerable restrictions that must be accounted for in the mission design. As the number of resident space objects (RSOs) continues to grow, techniques are needed to simplify these mission designs and remove the reliance on a single Sun vector for appropriate lighting conditions. This research summarizes and applies the historical basis of solar reflectors to the proximity operation issues encountered today. Building on this past research, a simulation has been created to test the efficacy of reflectors in facilitating less complex servicing/inspection missions. Initial testing has shown promising results for low mass membrane mirrors in augmenting illumination conditions with particular benefit in the geosynchronous orbital regime.

Through the course of this research, a novel method of initial orbit determination has also been developed. By observing the shadow of a RSO projected onto the surface of the Earth or a similar planetary body, the inertial position vector of the RSO can be calculated analytically. The inertial velocity can then be calculated using any number of techniques common in orbit determination algorithms. A large solar reflector could be used as the energy point source required by this technique. A computer vision-based program was created and tested to examine the accuracy and applicability of this method. Initial results are promising; however, significant further work must be accomplished to filter and weight measurements.

Acknowledgments

I would like to express my sincere appreciation to my faculty advisor, Major Bettinger. His continued support of my endeavors, whether academic, military, or personal has been an incredible asset in my graduate education. I have been inspired and learned so much from your example of as both an officer, academic, and leader. I would also like to extend a debt of gratitude to the Gwaltney family. Whether debugging code or pondering the greater mysteries of life you were always willing to lend an ear. And to my parents, thank you. From a young age you inspired a lifelong hunger for knowledge and adventure, driven by a desire to understand the beauty of the natural world. And to the countless friends I have made along the way, a most sincere thank you.

Daniel M. Dombrowski

Table of Contents

Page

List of Figures

Page

List of Tables

Page

List of Symbols

A_r	Mirror cross sectional area
$C_\odot$	Shadow centroid position in the LVLH frame
D_r	Instantaneous direction of travel
E_r	Energy of the reflected light
I_0	Radiation flux density
$R_\oplus$	Scalar radius of the Earth
Δ	Change in a quantity
μ	Standard primary gravitational parameter of Earth
a	Ellipse semi-major axis
b	Ellipse semi-minor axis
d	Scalar distance between two objects
e	Eccentricity
h	Altitude
k	Numbered run or trial, denoting place in sequence
l	True longitude
n	Mean motion of chief
P	Period of a satellite
R	Displacement
r	Reflector radius
V	velocity
x	Position along the x-axis of the chief's LVLH frame

y	Position along the y-axis of the chief's LVLH frame
z	Position along the z-axis of the chief's LVLH frame
α	Light source half angle of divergence
γ	Angle of incidence
δ	Turning angle, total angular change in direction of reflected illumination
η	Mirror coefficient of reflectivity
ν	True anomaly
ρ	Relative position vector of a deputy in a chief's LVLH frame
τ	Scalar distance from the shadow centroid to resident space object
χ	Areal density
ψ	Mirror surface figure coefficient

Constants

$\alpha \cong 0.00465$ rad	Half angle of solar illumination divergence
$\pi \cong 3.1416$	Pi, ratio
$I_0 \cong 1358 \frac{W}{m^2} \cong 136700$ lux	Radiation flux density near Earth
$\mu \cong 398600.5 \frac{km^3}{s^2}$	Standard gravitational parameter of Earth

Superscripts

I	Measured with respect to an inertial frame
LVLH	Measured with respect to a LVLH frame
$\dot{c}$ [dot]	Derivative with respect to time
$\bar{c}$ [bar]	Vector quantity
$\hat{c}$ [hat]	Unit vector quantity

List of Acronyms

AFIT	Air Force Institute of Technology
AFRL	Air Force Research Laboratory
CASpR	Control and Autonomy Space proximity Robot
CCD	Charge-coupled Device
COE	Classic Orbital Elements
DARPA	Defense Advanced Research Project Agency
ECI	Earth-centered Inertial
GEO	Geosynchronous Earth Orbit
HCW	Hill Clohessey Wiltshire Equations of Motion
IOD	Initial Orbit Determination
IR	Infrared
JWST	James Webb Space Telescope
LEO	Low Earth Orbit
LVLH	Local-Vertical-Local-Horizontal
MOI	Moment(s) of Inertia
NASA	National Aeronautics and Space Administration
NMC	Natural Motion Circumnavigation
RSO	Resident Space Object
SDA	Space Domain Awareness
SRC	Space Regatta Consortium
SSPIDR	Space Solar Power Incremental and Demonstrations Research
STK	Systems Tool Kit
SWaP	Size, Weight, and Power

INVESTIGATION OF MIRROR SATELLITE CONCEPT TO AUGMENT NATURAL LIGHTING CONDITIONS ON ORBIT

I. Introduction

The imaging and inspection of Resident Space Objects (RSOs) is an increasingly important mission as space-faring nations and commercial enterprises alike seek to develop means to repair and refuel satellites, as well as de-orbit RSOs in order to reduce orbital debris. The lighting conditions for imaging and inspection are not always advantageous for a servicing satellite and can place extensive restrictions on mission requirements. These restrictions can raise mission complexity, delay mission schedules, and increase mission costs. This research seeks to provide relief to these stringent requirements through the use of solar reflectors to augment the natural lighting conditions on-orbit.

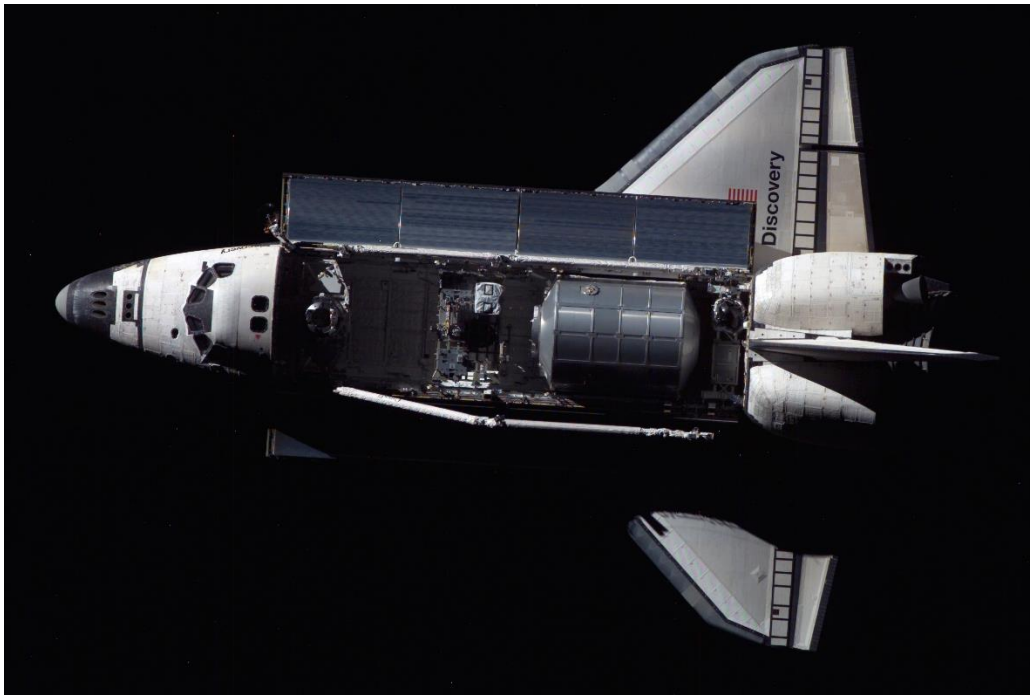

Figure 1. Self-Cast Shadows on Shuttle during Proximity Operations [1]

The proposed research seeks to further space-based mirror research through numerical simulation to determine basic techniques and procedures for augmented lighting proximity operations. The effectiveness of mirror satellites in reflecting solar energy to target RSOs will be examined for a variety of orbital conditions. Factors that will be considered are the mirror satellite's effective range, magnitude and consistency of target illumination, and appropriate orbital geometries. The research will advance the ongoing development of satellite servicing and Space Domain Awareness missions within the near-Earth orbital domain. The analytical focus on using dedicated mirror satellites to provide sources of augmented illumination is novel and could enable unique lighting opportunities to improve the current characterization of both natural and man-made objects in the near-Earth space environment. The output of this research will be a quantification of the benefits of a space-based mirror satellites for satellite servicing and SDA.

1.1 Primary Research Tasks and Scope

The main purpose of this research is to quantify the costs and benefits of using redirected solar radiation for the illumination and inspection of dimly lit orbital objects. Using solar reflectors for redirecting energy towards Earth has been studied extensively, however applying this technique to on-orbit inspection/servicing missions is novel.

In order to place reasonable bounds on the design space of this problem, four primary design considerations are examined: relative position, illumination, time, and fuel use. Every mission has specific needs and requirements that drive the mission concept and design, making a universal mission design impossible. Instead, this research will focus on meeting mission requirements that would be prohibitively strict given natural on-orbit

lighting conditions. Using the four design considerations the following research goals are developed. A reflector constellation and inspector trajectory should be designed such that it can:

1. Image all six sides of a target for full inspection ability
2. Constrain the incident illumination to within +/- 45 degrees from the line normal to each side of the target spacecraft to limit shadow lengths
3. Perform this maneuver within one period of the target spacecraft (to conserve time)
4. Perform this maneuver under natural motion (as defined by the classic two body problem) to conserve fuel

1.2 Secondary Research Tasks and Scope

As mentioned, the body of solar reflector research available is primarily concerned with redirecting solar energy to Earth. During the initial stages of this research, it was realized that should these solar reflectors be used in orbit, a method of initial orbit determination could be developed for satellites in low Earth orbit. As such, the initial research focus was placed on developing this IOD method. This research provided an opportunity to develop much of the optics, astrodynamics, and programming skills that would prove vital in the primary research. To this end the task of this secondary research was to develop the algorithm behind this IOD technique and begin initial testing to examine the accuracy and applicability of this method.

1.3 Primary Research Methodology

In order to design a constellation and inspector trajectory that can accomplish the research tasks both theoretical and numerical analysis will be used. In the design of the

inspector spacecraft's trajectory, the Hill Clohessey Wiltshire (HCW) equations are used as a starting point. The HCW equations are derived from a linearized solution, which assumes that two body gravity is the only force acting, that the inspector remains close to the target, and that the target is in a circular orbit. The simulation propagates motion using a numerical solution to the classic Two Body Problem. This means that any inconsistencies in the HCW assumptions other than two-body gravity will be modeled. In scope however, this research will focus on scenarios with a circular chief orbit. For the purposes of identifying line of sight and eclipse times, a spherical Earth model is assumed. For the purposes of this research, only translational motion is modeled. Attitude considerations will be discussed, however there is minimal constraining effect on the design space.

1.4 Secondary Research Methodology

Initial orbit determination algorithms vary widely in their fidelity. Since this technique is still in its infancy, a simple two-body model is used to perform the orbit determination as well as create the video file upon which this method will be tested. In addition, this technique assumes that the point light source has a constant illumination divergence angle, the size of the RSO is far smaller than its projected shadow, and the flat-Earth assumption applies over the size of the shadow's projected ground ellipse.

1.5 Thesis Overview

This chapter serves to provide an overview of the research tasks and objectives. Chapter II highlights solar reflector projects of the past, the designs and technology that were used, and modern technology that can be leveraged for innovative solar reflector designs. A brief introduction to IOD techniques will also be provided, with special attention

given to short-arc high data density techniques that could prove essential in the proposed method. Chapter III details the methodology behind the solar reflector designs as well as the proposed proximity maneuver. Chapter IV contains the testing results and analysis. Chapter V and VI transition to an overview of the secondary research. Chapter V examines the methodology behind the IOD algorithm and details the software implementation. Chapter VI contains the testing results and analysis of the IOD method. Finally, Chapter VII summarizes and provides conclusions for the total body of research, provides recommendations for future work, and discusses the relevance of the present research.

II. Literature Review

2.1 Introduction

For all spacecraft, illumination is a valuable asset, however it is also exceptionally variable, with lighting conditions changing dependent on altitude or seasonal variations. Carrying onboard active illumination sources to augment the natural lighting conditions on orbit is costly in terms of size, weight, and especially power (SWaP), if even feasible over the often-vast distances required. This is clearly evident in rendezvous and proximity operations. Although it is possible to model the natural lighting conditions and subsequent sensor response, these conditions can require extensive evaluation and can pose extreme hindrances on mission operations resulting in prohibitively strict mission requirements [2].

The Defense Advanced Research Projects Agency (DARPA) found this to be the case in the Orbital Express program. This program was meant to showcase advances in technology that may aid in satellite rendezvous and proximity operations and satellite servicing [3]. In the post mission NASA Engineering and Safety Center Technical Assessment Report, additional IR cameras and calibration issues were cited as lessons learned and recommendations in trying to combat the unanticipated changes to on-orbit lighting conditions [4]. These unanticipated or off nominal lighting conditions can cause bloom and glint on the CCD arrays, thus requiring robust dynamic range cameras [4]. If more desirable and consistent lighting conditions on orbit can be achieved with little to no impact on spacecraft SWaP, then it would yield vastly simpler and more efficient proximity operations missions.

This chapter will discuss the previous historical accomplishments of space-based solar reflectors at tackling illumination scarcity, the technology that allowed these past programs to be feasible, and modern technology that could prove effective in advancing current efforts. An exciting novel use for solar reflectors as a means of initial orbit determination will also be introduced.

2.2 Historical Space Based Reflector Programs

The Space Race between the United States and the Soviet Union during the mid-Twentieth Century produced major advancements in technology as both superpowers strove to carve out a foothold in the high ground of space. As early as 1968, space-based reflectors were investigated for efficacy in scenarios involving terrestrial illumination at night [5]. As technology advanced more audacious applications and projects were examined to provide illumination for farming, enhancing photosynthesis, solar power, Space Shuttle nighttime operations, and emergency operations [6] [7] [8]. The United States conducted significant research into large space-based reflectors, however no experiments ever made it to orbit [6] [9].

In the 1990's, the Russian Space Federation took the experimentation process further through the Znamya project. There were three iterations to the project named Znamya 2, Znamya 2.5, and Znamya 3, though the last was never built. Znamya 2 was a reflector spacecraft that had a diameter of 20 meters and used an eight-segment sparse aperture design as shown in Figure 2 [10]. The mirrors surface was comprised of aluminized PETF film, a Russian version of mylar, 5-μm in thickness [11]. This experiment did not use a rigid supporting structure to keep the reflector's shape but instead

the platform was spun to apply centripetal tension forces. This spinning and attitude control was provided from the Progress resupply vehicle as the crew aboard the Mir space station observed the deployment. The Space Regatta Consortium (SRC), in charge of the project, reported that the illumination disk on Earth was approximately 5-km in diameter as it traveled over northern Europe. Though covered in clouds many people reported seeing a flash of light and the SRC estimated the brightness of the illuminated spot to be approximately that of a full moon [12].

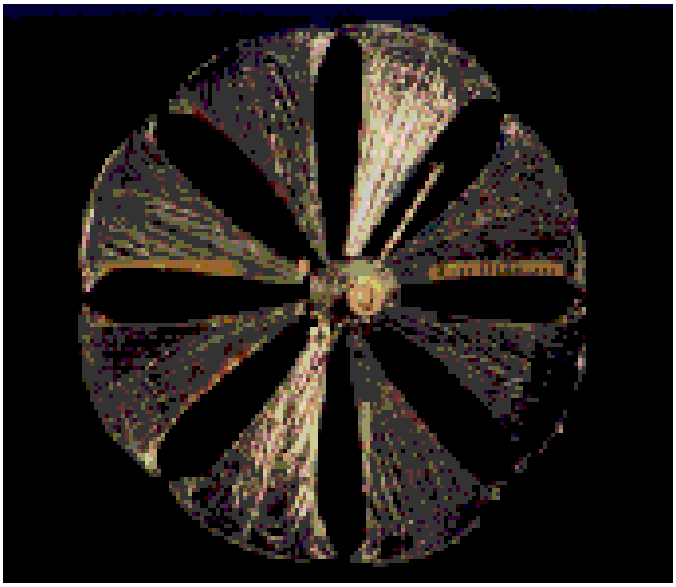

Figure 2. Znamya 2 on Orbit as seen from the Mir Space Station [12]

Znamya 2.5 was larger with a diameter of 25-m and was intended to test improvements to the film structure and a new attitude control system. Unfortunately, Znamya 2.5 did not deploy correctly from the Progress resupply vehicle due to mission operations and software failures [12]. An antenna on the vehicle failed to receive a command to retract prior to unfurling the reflector. The reflector then got tangled around

the deployed antenna. Attempts were made to retract the antenna and correct the issue but to no avail. Znamya 2.5 re-entered the atmosphere shortly thereafter.

Znamya 3 was planned to be built by the year 2000 and was proposed to be far larger than its successors with a diameter of 60-70 meters. A major advancement in the 3 series mirrors is that the mirror would not be segmented, but instead be one large monolithic structure. The Progress vehicle would also have to be greatly modified to handle the increased moments of inertia (MOI). A mirror this size would dwarf the Mir space station as shown in Figure 3. The Znamya project was cancelled before the design was ever realized.

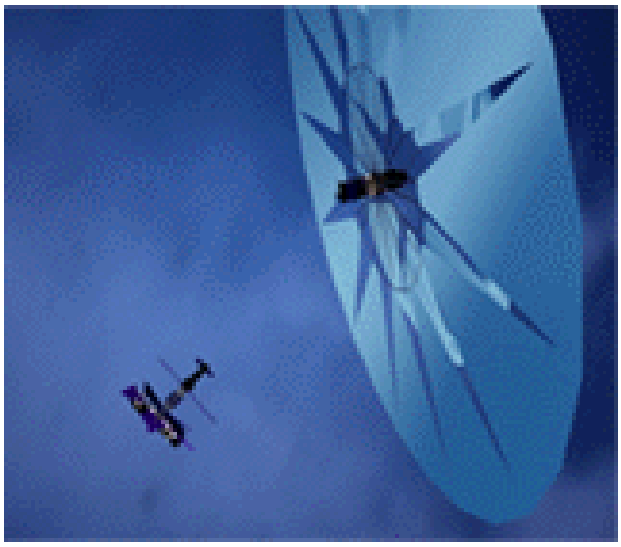

Figure 3. Artist Conception of the Znamya 3 near the Mir Space Station [12]

2.3 Traditional Reflector Technology

Historically there were several key technological developments that made large solar reflector experiments like the Znamya project feasible. A firm understanding of these technologies is required to leverage new technological advancements in design of a modern

solar reflector spacecraft. Mass constraints were handled through use of lightweight membrane mirrors and deployment structures, and low stress deployment techniques had to be created to accommodate the membrane structure.

There is little documentation available from Russian solar reflector programs; however, NASA has thoroughly documented the conceptual design process that took place between the 1970's and 1980's. NASA was particularly interested in applications related to solar farming though many other uses were also considered such as illumination of large urban areas, emergency operations, cattle farming, enhancing photosynthesis, and aiding in Space Shuttle on-orbit servicing missions [6] [9].The mission concept was to use the Space Shuttle to transport a spacecraft with a stowed solar reflector to 750-km altitude [6]. This phase required that the entire stowed reflector spacecraft fit within the cargo bay of the Space Shuttle along with a propulsion system required to boost the reflector spacecraft to an altitude between 1000-km and 5000-km. The spacecraft could then deploy its 1-km diameter solar reflector. At this altitude atmospheric drag effects have been reduced significantly, allowing for solar sailing to a final resident geostationary orbit in approximately 15.3 months [6] [9].

Creating large solar reflectors using a traditional monolithic glass mirror structure is not feasible due to size and mass constraints. Instead, new methods of mirror manufacturing had to be established. In order to meet these needs membrane mirrors were examined as a viable alternative. A Mylar or Kapton substrate is coated with a reflective material to create a mirror surface. There are many different coatings that could be used, three of the most reflective being sodium (Na), silver (Ag), and aluminum (Al) with approximate coefficients of reflectivity of 0.99, 0.98, and 0.92 respectively [6]. Though

sodium has the highest reflectivity it is extremely reactive within the atmosphere and would require coating on orbit. NASA recommended that sodium be used should on-orbit production facilities become a reality. Silver may not be ideal for the space environment as it oxidizes rapidly in the presence of atmosphere. This can be negated by use of a thin transparent covering, though most plastics suitable for this purpose are prone to radiation degradation, a factor that is doubled due to the reflected light having to pass through the layer twice. These plastics would also add weight to the spacecraft which would add to launch costs and make attitude control more difficult. This leaves aluminum as a prime candidate. Not only is the reflectivity greater than 90%, but it is also lightweight, physically robust in the atmospheric and space environments, a relatively inexpensive and commonly used coating, and has weak absorption bands in the infrared which could help in cooling the spacecraft.

In order to facilitate the stowed launch requirements, NASA proposed using a spacecraft body which handles the typical spacecraft bus functions, and the reflector payload would be stowed along the outside edge of the spacecraft. Upon deployment, the rim truss cannisters would deploy and a combination of stay tapes and edge tensioners would be used to gently guide the reflector into a flat shape, similar to the deployment process of a simple rain umbrella. The stowed and deployed designs are shown in Figure 4 and Figure 5 below.

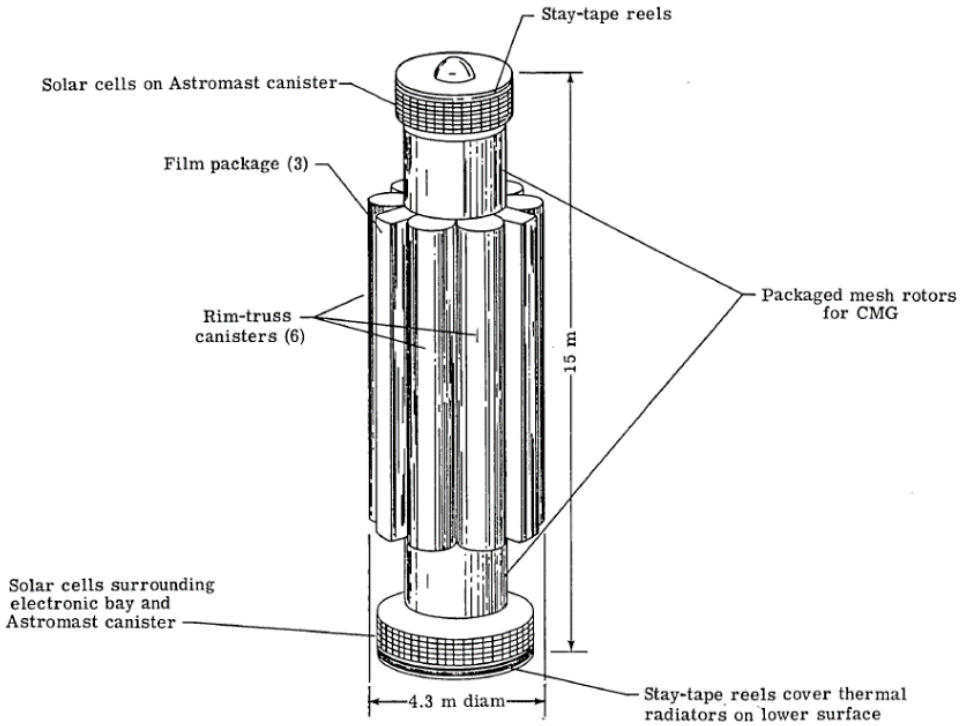

Figure 4. NASA Stowed Solar Reflector Design [6]

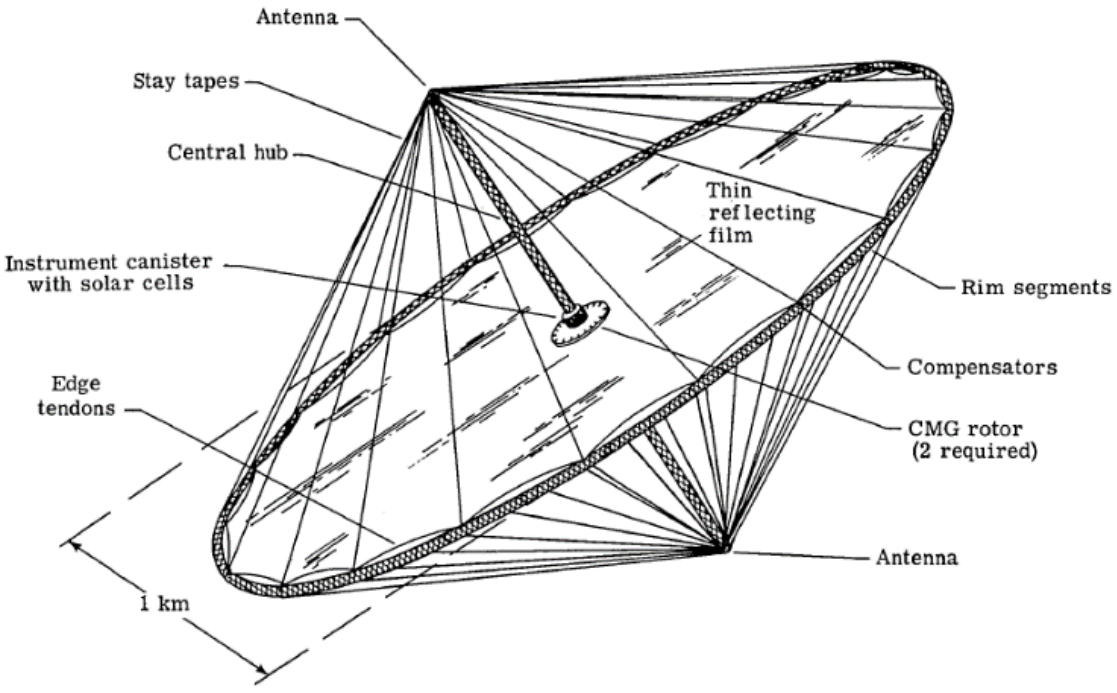

Figure 5. NASA Deployed Solar Reflector Design [6]

There are four primary loads derived from environmental and mission needs that a solar reflector spacecraft must be carefully engineered to handle: solar pressure, atmospheric drag, gravity gradient, and control or slewing loads. Exactly quantifying these effects is nearly impossible due to the variety of factors effecting the loads to include the spacecraft's orientation with respect to the Sun, location of the spacecraft in the ever-changing magnetic field of the Earth, and even the current state of the solar cycle. General estimates are known and given that these loads are generally small (nominally on the order of 10^{-3} Pa) designs with sufficient margin can be established. Figure 6 below summarizes these conditions for the NASA designed 1-km diameter solar reflector based on worst case estimates and with all pressures assumed to act normal to the membrane surface.

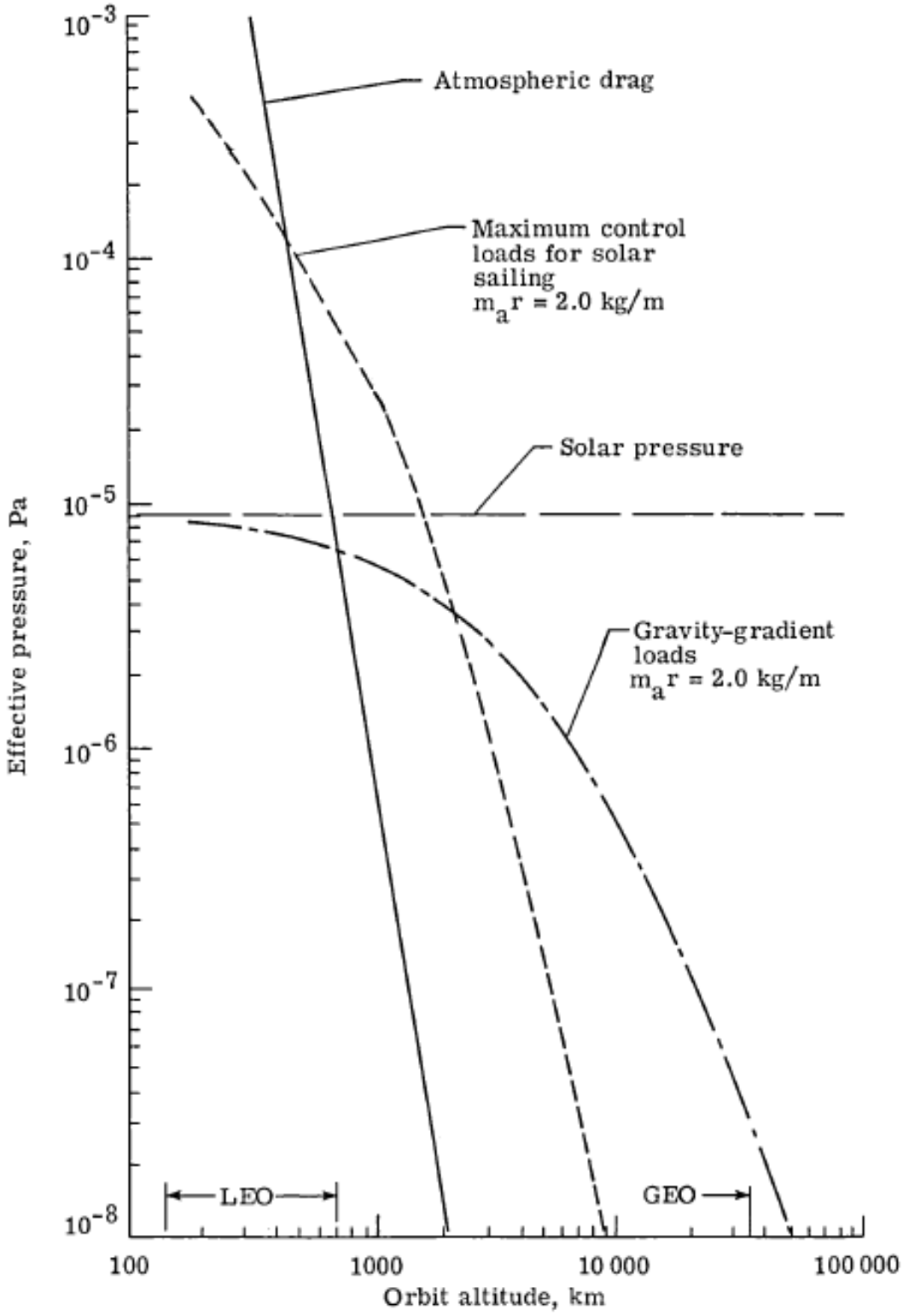

Figure 6. Maximum Loads on Reflector Membrane of 1-km Spacecraft [6]

The effect from solar radiation pressure is present at all altitudes after the solar reflector is deployed. This pressure is greatest when the mirror surface is perpendicular to the incoming rays. Atmospheric drag pressure is largest at the lowest orbital altitudes and the magnitude of this perturbation is largely influenced by solar weather phenomenon and the current solar cycle condition: when the solar cycle is at its maximum, the upper atmosphere becomes denser, thereby increasing the drag force experienced by a given spacecraft. The gravity gradient load is based on an estimate of the reflector density and is worst-case at the edge of the solar reflector. The NASA solar reflector assumes a distance to the edge of the reflector of 500-m and a density of 0.004-kg/m^2. This results in a gravity gradient pressure of mass per unit area of 2-kg/m as shown in the Figure 6. Gravity gradient loads are greater at lower orbital altitudes due to the larger orbital angular velocities. Control loads are largely dependent on the mission requirements. NASA calculated the control loads for the solar sailing mission segment and ground site tracking. Both these scenarios produced approximately equal loads as described by the figure. The maximum loads for control again occur at the reflector's edge, resulting in a worst-case mass per unit area of 2-kg/m. The highest solar sailing/tracking loads again occur at lower orbital altitudes due higher orbital angular velocities requiring faster rotation to track the Sun or a specified ground target. Ultimately, NASA concluded that the described solar reflector should be designed to handle inertial loads from a maximum angular acceleration of $2.75x10^{-3}$-mrad/sec^2, dominated by the solar sailing and gravity gradient load requirements.

2.4 Leverageable Technological Advancements

Since the late 1990's there have been several major technological breakthroughs that can make large membrane mirror structures more feasible for a variety of uses, with several of the primary advances related to aperture size, deployment, and system control. Much of this advancement has derived from the field of astronomy where large aperture optics are integral to high resolution imagery.

The James Webb Space Telescope (JWST) is a prime example of advanced deployable large aperture technology. The legacy Hubble Space Telescope features a single monolithic primary mirror with an aperture of 2.4-m and launched within the payload bay of the Space Shuttle [13]. By comparison, the JWST boasts a 6.5-m aperture [14]. In order to accommodate this aperture size in the fairing, the JWST is a segmented deployable telescope using 18 distinct hexagonal mirror reflectors in the primary collecting aperture [15]. These mirrors have six degree-of -freedom control, as well as a radius of curvature adjustment [16]. While the JWST is an incredible example of the modern abilities with deployable optics, the project has become notoriously overbudget and overschedule. NASA has also invested in lower cost/mass reflector options utilizing advances in membrane optics and control techniques. NASA's Innovative Advanced Concepts program funded research by Northwestern University and the University of Illinois for creation of a satellite using a deployable mirror using magnetic smart materials called APERTURE (A Precise Extremely large Reflective Telescope Using Re-configurable Elements) shown in Figure 7 [17].

In traditional membrane optics, the surface figure of the instrument is controlled using piezo-electric patches. These patches are transducers that respond to an electric

charge by generating a mechanical stress or vice-versa. Theses patches can be used as both as sensors and as actuators. While the ceramic elements of these parts tend to be brittle, by embedding them in a thin foil, roughly 100 to 500-μm thick, a transducer can be created that is quite ductile [18]. By embedding these transducers in the mirror substrate, on orbit corrections to mirror shape can be performed.

Recently, magnetic smart materials have been proposed as an alternative to piezo-electric patches in order to reduce the quantity of electrical hardware needed to actuate the mirror correcting device. The APERTURE concept uses an aperture design where the mirror substrate is coated with a magnetic smart material that retains its shape after an interaction with a magnetic field and the satellite bus has a magnetic write head that is attached to an arm. When surface figure corrections are required, this arm swings into position and the electromagnet applies a magnetic field using magnetostriction to bring the mirror into shape [19]. The magnetic smart material will then hold this correction.

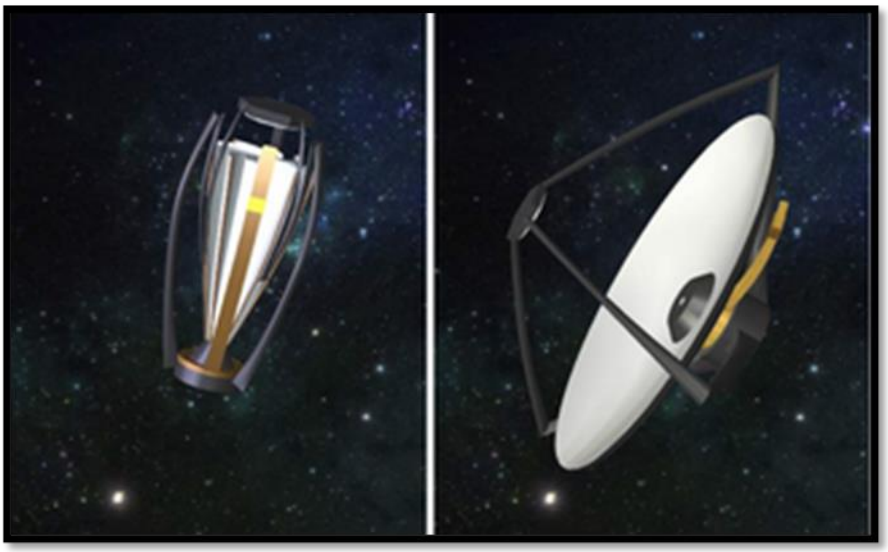

Figure 7. APERTURE Design Concept [17]

Piezo-electric patch technology has been shown to work for wavelengths greater than about one millimeter, though the surface error has not been able to be reduced past the $\lambda/20$ needed for ultra-violet and visible observation [20]; magnetic smart materials have the potential to meet this error however more testing must be done. For solar reflectors where surface figures are not needed to be as stringent both of these surface figure corrective methods show great promise.

2.5 Alternative Application to Initial Orbit Determination

There exist numerous uses of large solar reflector spacecraft constellations as discussed. A novel use that this research seeks to explore further is that of spacecraft orbit determination through the use of a reverse occultation problem. Utilizing illumination and eclipse timing techniques has been shown to be applicable to low Earth orbital regimes with errors typically on the order of several kilometers [21]. In place of observing solar or stellar eclipses, large solar reflectors or other space-based energy point sources can provide illumination that is projected upon the surface of the Earth. This illuminated region can then be observed for shadows passing though it and pose information can be gained from the resulting shadow geometries.

Should a reasonably large nadir pointing solar reflector be placed into orbit, it would act as a point light source. This would cause anything that passes through its cone of reflected light to cast a shadow onto the Earth with a negligible penumbra creating shadows with well-defined edges. This fact allows for a reverse occultation problem, using the project shadow on the surface of the planetary body for creation of an inertial position vector. An occultation occurs when an object passes in front of a light source, partially or

completely obscuring the light [22]. Historically, stellar occultations have been used to determine the shape parameters of objects as far as the Kuiper Belt [23].

In this reverse occultation problem, the shadow from a resident space object is projected onto a planetary surface and observed. A translational orbit model is derived using the inertial position and velocity vectors. Traditional optical or radar equipment can only provide angular or range data respectively. Performing orbit determination utilizing only these data sets yields inherent ambiguities [24]. One of the benefits of the proposed method is that all three components of the inertial position vector can be calculated deterministically, doing away with these ambiguities.

In recent years, short arc orbit determination methods have seen significant research in the realm of asteroid orbit determination as well as satellite optical tracking [25]. Contemporary research has shown that accurate orbit determination can be performed with dense observational data collected within a short interval (several hundred observations per satellite pass) [26]. High data density techniques are ideally suited to this IOD method. Using either modest frame rate cameras or luminosity sensors hundreds of observations can be gathered quickly. The development of this novel initial orbit determination method will be discussed at length in Chapter V.

2.6 Summary

This chapter served to review relevant scientific literature as it pertains to the use of solar reflectors and their applications. Significant research into solar reflector programs has been performed in the past; however, since the turn of the century, new research has remained largely dormant. Advances in astronomy tools and techniques have yielded new

technology that can be applied to solar reflector designs. These advancements have thoroughly matured the technology needed to create large, accurate solar reflectors that can collect and reflect light to desired locations. In the following chapters the application of this technology to augmenting natural on-orbit lighting conditions in addition to an alternate use as a means of orbit determination will be discussed.

III. Augmenting Lighting Conditions on Orbit Methodology

3.1 Introduction

Imaging and inspections missions have a long heritage in space programs. These missions often have to consider Sun vectors to accommodate imaging requirements. With too little illumination image exposure becomes impossible, while too much sunlight or target reflectivity can overexpose or blind imagers, and even the specific Sun vector angle must be considered as obtruding features on the target spacecraft can cast shadows over smaller surface features that are of interest. Subjecting proximity operations to natural lighting conditions places extensive restrictions on mission design and requirements.

Carrying onboard active illumination sources to augment the natural lighting conditions is costly in terms of size, weight, and especially power, if even feasible over the often-vast distances required. With the recent advancements made in membrane and adaptive optics, large solar reflectors are now a viable and realizable option. Though the use of solar reflectors for augmenting natural lighting for proximity operations is novel, it builds on decades of solar reflector research and experimentation. The goal of this study is to design and simulate a solar reflector constellation that will allow an inspector spacecraft to:

1. Image all six sides of a target for full inspection ability
2. Constrain the incident illumination to within +/- 45 degrees from the line normal to each side of the target spacecraft to limit shadow lengths
3. Perform this maneuver within one period of the target spacecraft (to conserve time)
4. Perform this maneuver under natural motion (as defined by the classic two body problem) to conserve fuel

We will begin by discussing the fundamental optics and design principles, followed the creation of the simulation, and the design of the proximity maneuver. In the following chapter results and implications of the testing will be summarized.

3.2 Fundamental Optics

In order to create and test the efficacy of mirror technology in a realistic scenario significant research was performed to accurately portray the mirror's optic properties. Equation 3.1 below shows the energy of the reflected light E_r, where η is the mirror coefficient of reflectivity, ψ is the mirror surface figure (or flatness) coefficient, I_0 is the radiation flux density, A_r is the mirror cross sectional area, and γ is the reflected radiation's angle of incidence.

$$E_{r1} = \eta\psi I_0 A_r \cos(\gamma) \tag{3.1}$$

For the purposes of this research, the mirrors will be assumed to be manufactured from an aluminum coating on a Kapton substrate. These mirrors were chosen due to their physical properties making them the ideal candidate for large space-based mirrors [6]. Being slightly conservative both a surface figure and reflectivity coefficients of 0.9 were used throughout the simulation process.

The radiative flux intensity is assumed to be 1358 W/m^2 to align with approximate solar intensity values in near-Earth orbits. For this paper however the units for radiative flux intensity will be given in lux, or lumen per square meter. This is due to the fact that the candela base unit id weighted to match a model of the human, which is convenient for the visible range of the electro-magnetic spectrum our analysis is concerned with. It also

allows for easy comparison of the on-orbit lighting conditions with that of daily life as shown in the table below. In this study it is assumed that 1358 W/m^2 = 136,700 lux.

Table 1. Lux values in common environments

Lux Value	Example
10,000–25,000	Earth based daylight condition not in direct Sun [27]
1000	Overcast day or nighttime sports stadium [6] [27]
300-400	Office lighting [28] [29]
100	Extremely overcast day [27]
3.4	Dark limit of civil twilight [30]
< 1	Full moon on a clear night [27]

It is also important to note that the Sun is not a true point light source and its light is not collimated. The half angle of solar divergence is approximately 0.00465 radians. While this is a small angle, over the array of separation distances encountered on-orbit significant loss in light intensity occurs due to the inverse square law. The illumination flux at a desired target for a single mirror with a non-collimated light source is given in the equation below, where d is the distance from the mirror to the target and α is the half angle of divergence of the light source:

$$I_{t1} = \frac{\eta\psi I_0 A_r \cos(\gamma)}{\pi(d \cdot \tan(\alpha))^2} \tag{3.2}$$

From this equation there are three main design variables through which to engineer a system: A_r, γ, and d. The illumination flux at the target can be increased by using a larger reflector, minimizing the angle of incidence, or minimizing the distance between the reflector and the target.

Using a larger mirror is an obvious solution, however spacecraft are often limited in SWaP constraints. These constraints are minimized through the use of membrane mirrors

as have been described. This allows for larger mirrors than traditional monolithic structures. A more difficult design issue is that of minimizing the cosine loss term.

As the angle of incidence nears 90-degrees, the cosine loss term dominates the equations and reduces the reflected energy to a near zero value. In order to combat this, a bifocal dual mirror design is proposed. Using two mirrors, the angle of incidence at each mirror can be reduced, thereby combating the large cosine loss at higher angles of incidence. In order to find the optimal angle for each reflector, a turning angle, δ, is defined as a constant angle equal to the total angular change in direction of the illumination from its original path. This results in the following definition for the bifocal dual mirror system, where $0 < \delta < \pi$.

$$\delta = 2(\gamma_1 + \gamma_2) \tag{3.3}$$

The cosine efficiency term we are seeking to maximize is written as:

$$f(\gamma_1) = \cos(\gamma_1) \cdot \cos(\gamma_2) \tag{3.4}$$

Where θ_2 is constrained as the turning angle is a constant in accordance with the following equation.

$$\gamma_2 = \frac{\delta}{2} - \gamma_1 \tag{3.5}$$

The first derivative of the cosine efficiency function is then taken, set to zero, and solved to find the critical points of the function as shown below.

$$f'(\gamma_1) = -sin(\gamma_1) \cdot cos(\gamma_2) + cos(\gamma_1) \cdot sin(\gamma_2) \tag{3.6}$$

$$f'(\gamma_1) = 0 \tag{3.7}$$

$$sin(\gamma_1) \cdot cos(\gamma_2) = cos(\gamma_1) \cdot sin(\gamma_2) \tag{3.8}$$

$$tan(\gamma_1) = tan(\gamma_2) \tag{3.9}$$

$$\gamma_1 = \gamma_2 \tag{3.10}$$

In order to ensure this critical point is a maximum the second derivative and evaluated at the critical point as shown below.

$$f''(\gamma_1) = -2 \cdot cos(\gamma_1) \cdot cos(\gamma_2) - 2 \cdot sin(\gamma_1) \cdot sin(\gamma_2) \tag{3.11}$$

The value of this function will always be negative over the range of γ, namely [0, π/2]. By the second derivative test we have proved that this efficiency function is maximized at the critical point where the angles of incidence are equal.

This optimization process results in Equation 3.12, noting that both mirrors are identical in their physical properties and the angle of incidence is equal.

$$E_{r2} = \eta^2 \psi^2 I_0 A_r \cos^2(\gamma) \tag{3.12}$$

The dual mirror system also allows for a possibility of collimating this light. Each of the dual mirrors could be slightly spherical in shape or a lens could be placed between the two larger solar reflectors to accomplish this task. This collimation eliminates the inverse square loss term seen in Equation 3.12, resulting in the equation below.

$$I_{t2} = \eta^2 \psi^2 I_0 \cos^2(\gamma) \tag{3.13}$$

This allows for a constant luminosity regardless of range from the target, since this luminosity is contained entirely within the collecting area (cross sectional area multiplied by the cosine loss). At farther distances the dual mirror system will prove a better illumination source than the single mirror.

Unfortunately, the realizability of this collimating mirror system is significantly questionable at best. Lenses are not a good option as they are large, have high mass, have difficulty surviving the launch environment, and must be manufactured to a high degree of

accuracy. Spherical mirrors are not much of an improvement either. In order to collimate the light, the Sun should be placed at the mirrors focus. For spherical mirrors, the radius of curvature is equal to twice the focal length. This results in a mirror with a radius of curvature of approximately 2-au. This geometry is summarized in Figure 8 below.

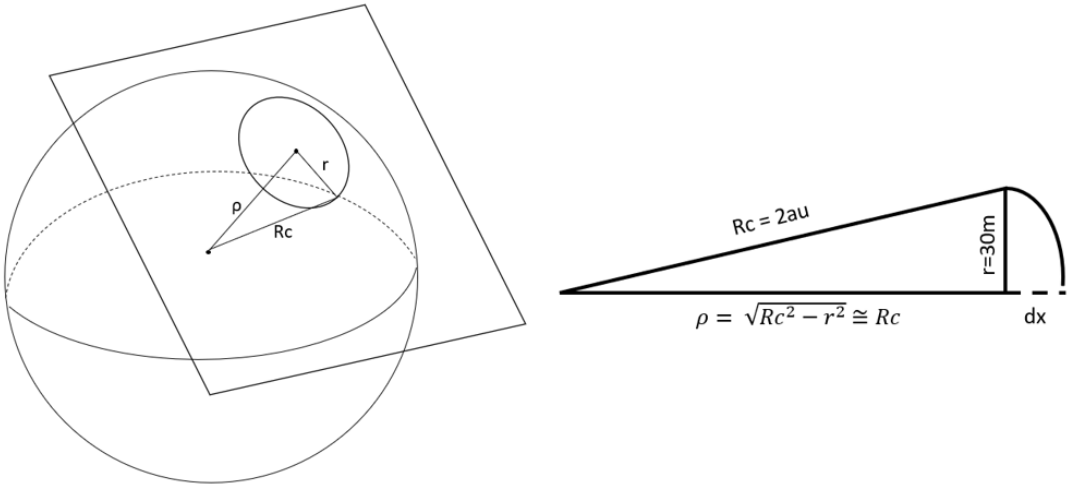

Figure 8. Radius of Curvature Geometry

Even for a 30-m radius mirror the deflection, given as dx in Figure 8, is incalculably small. A mirror with a radius of 10-km would have a maximum deflection of only 183-μm. Attempting to control a membrane mirror to this degree of accuracy is prohibitively difficult.

Using a dual mirror system is not always advantageous anyway. At higher angles of incidence, the cosine loss is minimal, and a single mirror performs better since the surface and reflectivity losses are only encountered once. Performing numerical analysis on the mirrors described in the preceding sections, it becomes advantageous to use a dual mirror system when reflecting light over 90-degrees from its original path. The figure

below shows a plot of the performance of the single vs dual mirror system over a range of turning angles.

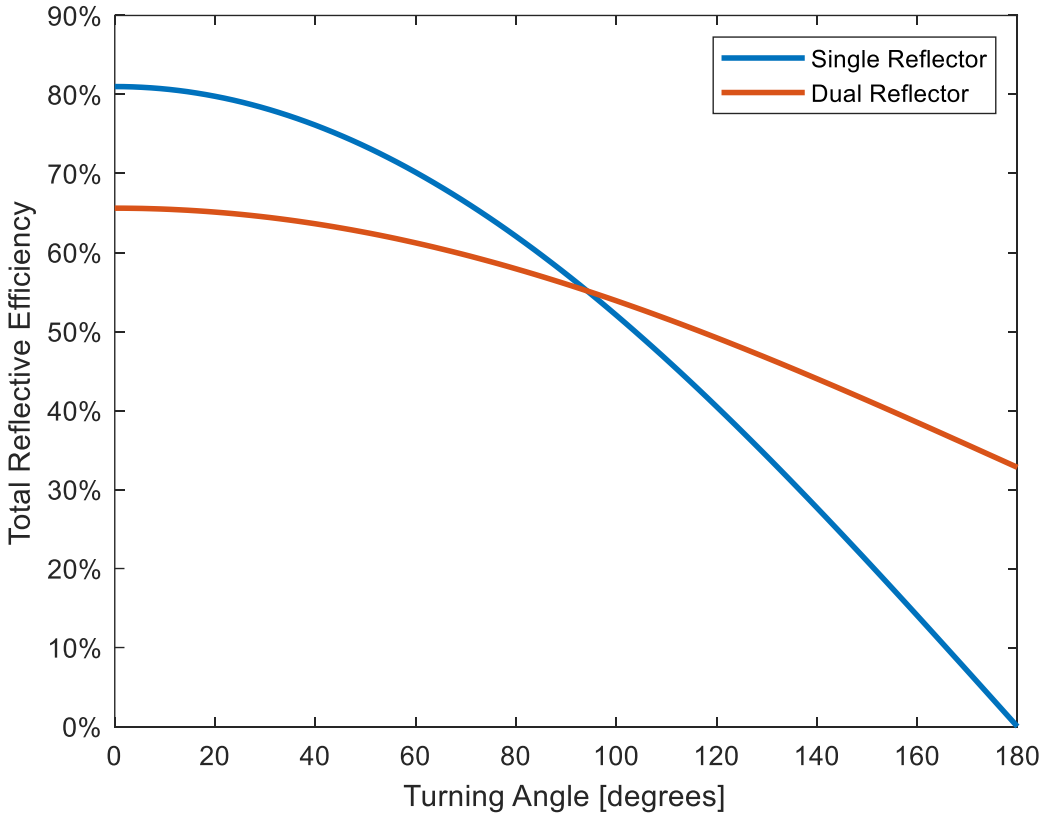

Figure 9. Single vs Dual Mirror System Performance

The distance between the reflector and the target is the third design variable, and perhaps the most mission dependent. Should light not be collimated, the distance variable is extremely important. Proximity operations using CubeSats have already demonstrated the ability to come within 22-m of a target spacecraft [31].

An understanding of the basic optics principles and design variables set forth in this section facilitated the creation of a complex simulation in MATLAB to evaluate the

performance of these mirrors and their efficacy in augmenting lighting conditions during proximity operations.

3.3 Simulation Process

The simulation was modeled in three ways:

1. With two solar reflectors placed 180-degrees apart in a circular Sun-synchronous orbit at an altitude of 1000-km that have the ability to collimate sunlight
2. With two solar reflectors placed 180-degrees apart in a circular Sun-synchronous orbit at an altitude of 1000-km without collimating ability
3. Without these two Sun-synchronous spacecraft

The dedicated solar reflector spacecraft are large solar reflectors based on the Znamya reflectors of the 1990s, utilizing a dual mirror system with a radius of 30-m in order to avoid exceptionally high cosine loses near 90-degree angle of incidence. The Sun-Synchronous orbit allows these spacecraft to avoid eclipse, meaning that they can reflect light constantly, particularly to the eclipsed regions of the target's resident orbit. It was found that these large solar reflectors do not add substantial capability to the system. Particularly for the more realistic non-collimating reflector, any additional illumination it provided was well under 0.5-lux, a negligible addition. The results from these trials are shown in Appendix A and Appendix B, and will be discussed briefly in Chapter 4.4. Due to this analysis the remainder of this document will focus on single plane mirror reflector attached to the inspector spacecraft. This is configuration is illustrated in the figure below, showing the relative motion of the inspector spacecraft about the target spacecraft in the

target's LVLH reference frame, with the natural sunlight represented as a solid yellow arrow and the reflected light with a dashed yellow arrow.

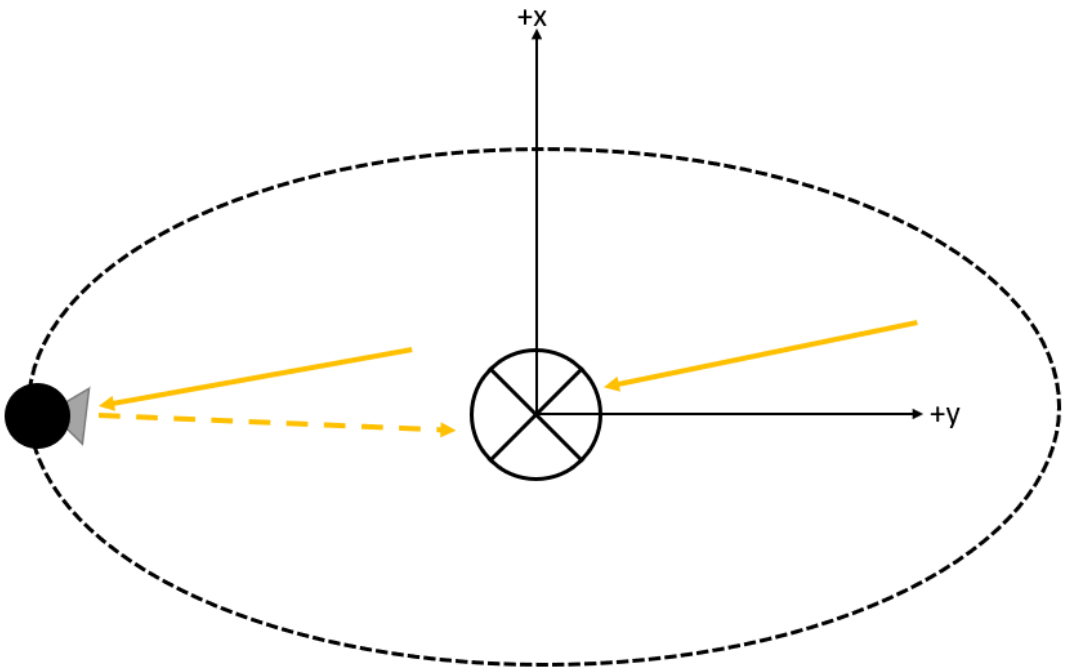

Figure 10: Inspector Trajectory and Reflector Configuration

The simulation created contains a target and inspector spacecraft. The target spacecraft is modeled as a sphere with radius of 1-m. It is assumed to be a nadir pointing spacecraft, such as an Earth imager. The goal of this project is to determine proximity operation methods that take advantage of the augmented lighting conditions provided by solar reflectors. As such, it is important to know which side of the target is being illuminated. For the purposes of this paper, we will define a side to be based off of the target satellites LVLH reference frame. Side one is defined as the 45-degree spherical pyramid whose spherical base is in the Earth pointing (-x) direction in the LVLH frame. Side two is then defined as the side in the y direction in the LVLH frame. Side three and

four are then counted in consecutive order. Side five is defined as the face in the positive angular momentum direction (z) and six is in the negative angular momentum direction (-z). This geometry is summarized in Figure 11. The code used to perform this logic is included as Appendix C.

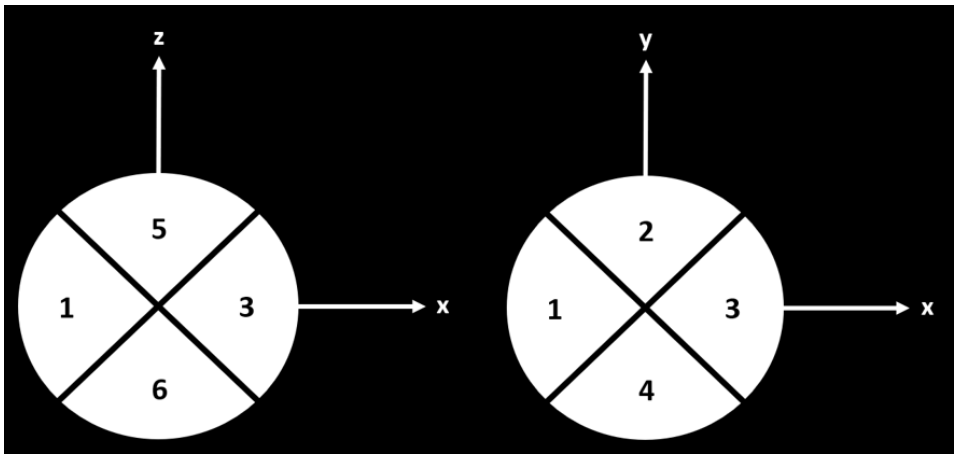

Figure 11. Definition of Target Sides in Target LVLH Frame

The second type of spacecraft is an inspector spacecraft that will be performing the proximity operations. Modeled as a sphere with a radius of 1-m, this spacecraft is equipped with a 1-m radius single plane mirror with physical properties as described by the previous section.

The spacecraft orbits are propagated using the classic two body equations of motion. After propagating the spacecraft's orbit, a series of logic statements are then used to determine the illumination conditions. Within this scenario there are three possible illumination conditions that must be considered as detailed in Table 2.

Table 2. Summary of Illumination Conditions

Illumination Path	Value [lux]	Name
Direct Sunlight on Target	136,700	Sunlight
Sunlight-Inspector-Target	Dependent	Inspector
No illumination	0	None

In order for a side of the target to be in direct sunlight, it must not be in the shadow caused by the Earth or any of the other spacecraft in the scenario. Though occlusions from the shadow of other spacecraft is a rare occurrence, it was included in the simulation to account for the close proximity operations being conducted. Within the simulation a spherical Earth is assumed, and all shadows are modeled to include both umbral and penumbra regions in order to display a worst-case scenario. The code used to perform this logic is included as Appendix D.

In order for the sunlight to be reflected from the inspector satellite to the target, the target must have line of sight with the target and must not be eclipsed. Upon analysis of the available illumination paths, the simulation then calculates the energy available through the inspector's reflector if available using Equation 3.2.

It is important to note that though multiple sources may be able to provide illumination of the target, only those illuminating the side the inspector is facing are pertinent to this scenario. Therefore, the simulation outputs a file that displays which side the inspector satellite is viewing, whether it is illuminated, the source providing maximum illumination, and the magnitude of said illumination. These outputs can then be analyzed in a variety of different scenarios to determine the best techniques and procedures to maximize the illumination of resident space objects during proximity operations. This process is summarized in the following figure:

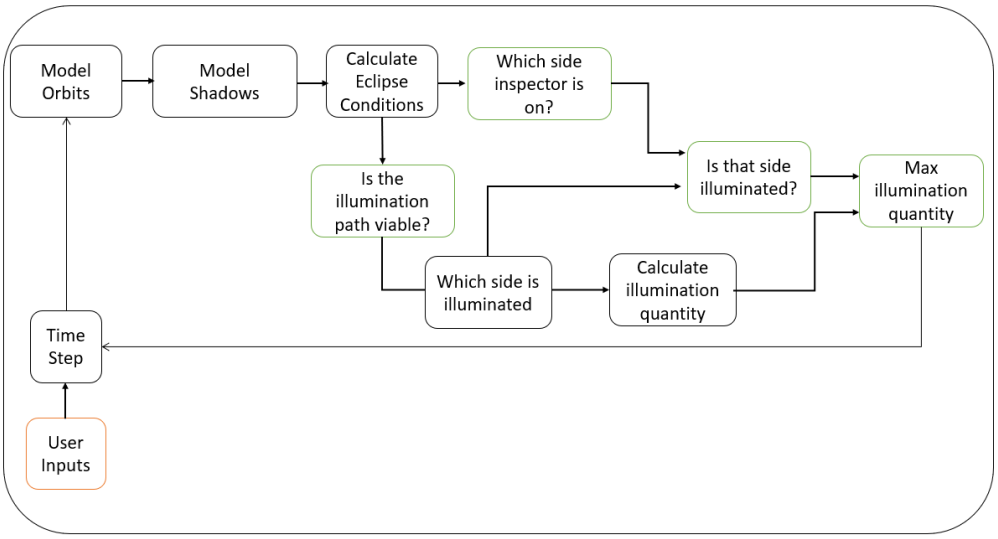

Figure 12. Simulation Process

3.4 Formation Design

The overarching goal is to inspect all six sides of the target with the source of illumination being within +/- 45 degrees from the line normal to each side of the target spacecraft. The reflector formation aiding in this accomplishment has been overviewed in the previous section.

In order to see all six sides of the target, specific proximity operations techniques must be introduced. The solutions of the Hill Clohessey Wiltshire (HCW) equations, shown in Equation 3.14 through 3.19 below, were used to derive these procedures due to their easily visualized nature.

$$x(t) = \left(-3x_0 - \frac{2}{n}\dot{y}_0\right)\cos(nt) + \frac{1}{n}\dot{x}_0 \sin(nt) + 4x_0 + \frac{2}{n}\dot{y}_0 \tag{3.14}$$

$$y(t) = \left(6x_0 + \frac{4}{n}\dot{y}_0\right)\sin(nt) + \frac{2}{n}\dot{x}_0 \cos(nt) + y_0 - \frac{2}{n}\dot{x}_0 - (6nx_0 + 3\dot{y}_0)t \tag{3.15}$$

$$z(t) = \frac{\dot{z}_0}{n}\sin(nt) + z_0\cos(nt) \tag{3.16}$$

$$\dot{x}(t) = \dot{x}_0\cos(nt) + (3nx_0 + 2\dot{y}_0)\sin(nt) \tag{3.17}$$

$$\dot{y}(t) = (6nx_0 + 4\dot{y}_0)\cos(nt) - 2\dot{x}_0\sin(nt) - 6n\,x_0 - 3\dot{y}_0 \tag{3.18}$$

$$\dot{z}(t) = \dot{z}_0\cos(nt) - z_0 n\sin(nt) \tag{3.19}$$

The derivation of the HCW equations of motion from the classic two body problem has been detailed extensively in other works [32]. The use of the HCW equations implies several key assumptions, namely that the two-body orbit model and associated assumption apply, that the inspector remains close to the target, and that the target is in a circular orbit. These assumptions can cause unacceptable error in some applications; however, we limit the scope of this project to orbits where these assumptions do not introduce significant error. In these orbits the perturbation forces, errors in modeling, and inaccurate measurements can be overcome with minimal control effort.

We develop our technique through the use of a key feature in the HCW equations. If the drift term is set to zero as shown in the equations below, then it can be noted that the x(t) and y(t) solutions allow for a 2x1 ellipse in the x-y orbital plane.

$$\dot{y}_0 = -2nx_0 \tag{3.20}$$

$$\therefore y(t) = \left(6x_0 + \frac{4}{n}\dot{y}_0\right)\sin(nt) + \frac{2}{n}\dot{x}_0\cos(nt) + y_0 - \frac{2}{n}\dot{x}_0 \tag{3.21}$$

It can also be seen that the z(t) solution yields a simple harmonic oscillator and is entirely decoupled from the x(t) and y(t) solutions. These observations allow for a trajectory referred to as a natural motion circumnavigation (NMC).

In order to center the NMC ellipse about the origin point (e.g., the center of the chief spacecraft) both x(t) and y(t) ellipse centers must be set to zero

.
$$4x_0 + \frac{2}{n}\dot{y}_0 = 4x_0 + \frac{2}{n}(-2nx_0) = 0 \tag{3.22}$$

$$y_0 - \frac{2}{n}\dot{x}_0 = 0 \tag{3.23}$$

Since Equation 3.22 is met simply by using the no-drift condition found in Equation 3.20 we only must comply with Equation 3.23 to center the ellipse. In order to simplify this task, we will assume that we are entering the NMC at $y_0 = 0$ and therefore need no $\dot{x}_0$, or in other words are at the maximum x distance.

Should we enter an NMC honoring these conditions with zero z position or velocity we would enter an NMC solely in the x-y plane. The cross-section of the plane of this ellipse with the target spacecraft would only intersect with sides 1, 2, 3, and 4. The geometric application of seeing all six sides is similar to forming a hexagon from a plane intersection a cube. In order to accomplish this task, the plane must be inclined and rotated with respect to the cube as shown in Figure 13 below.

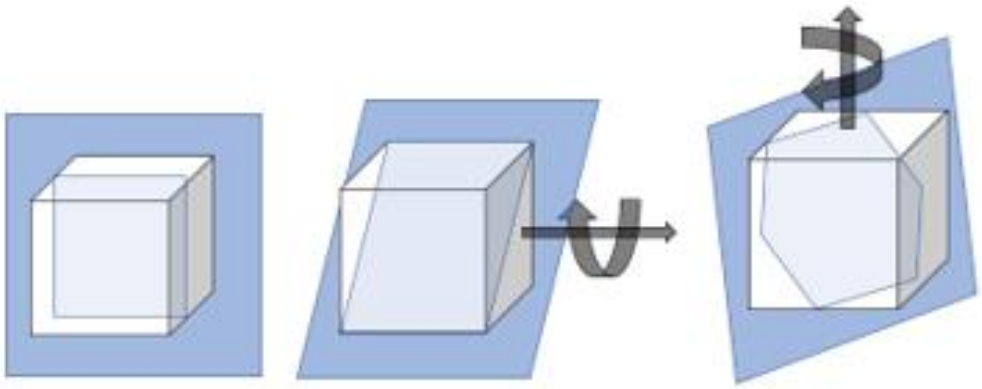

Figure 13. Hexagon Formed from Planar Cross Section of a 3D Cube

This inclination is akin to creating a hexagonal cross-section through the cube, ensuring that all sides are seen by the inspector. This inclination is performed by adding in a z-

component to the initial position and velocity. The z-component in the initial position inclines the NMC in the x-z plane. This is essentially a rotation of the 2x1 ellipse in the x-y plane about the chief's y LVLH axis. The velocity component ensures that we are not at the maximum z-position which inclines the NMC in the y-z plane. Therefore, the maximum x, y, and z components all occur at distinct points in the ellipse trajectory. This is essentially a rotation of the 2x1 ellipse about the Chief's z-axis. These rotations, by addition of z initial position followed by z initial velocity, are shown in the STK simulation below.

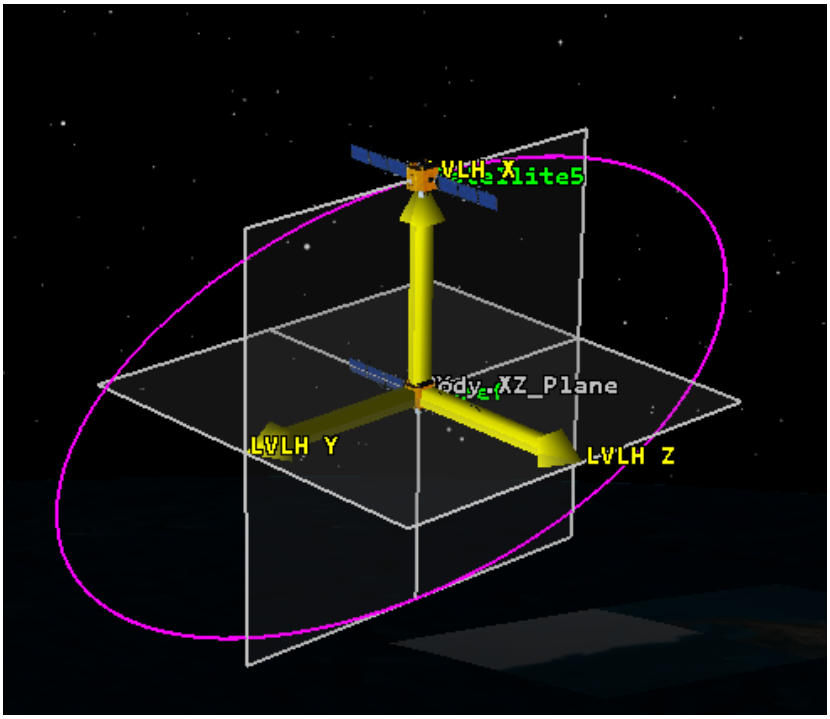

Figure 14. XY Planar NMC

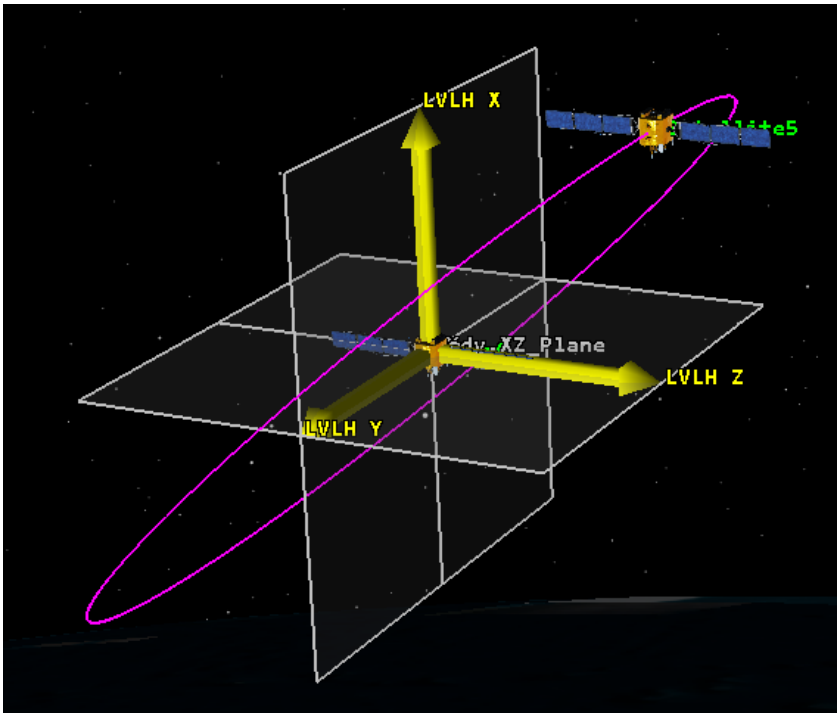

Figure 15. NMC Rotated about Y Axis

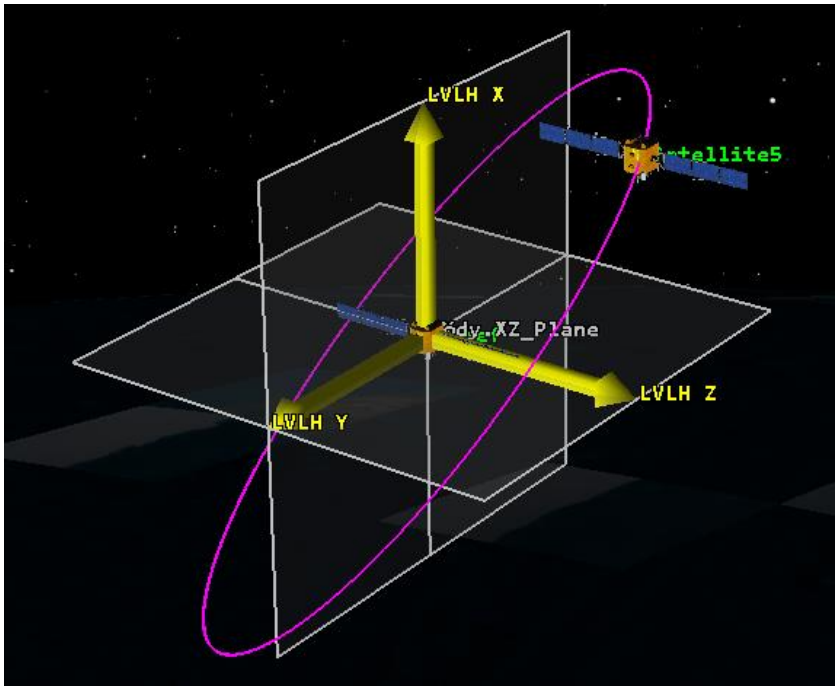

Figure 16. NMC Rotated about Y Axis followed by Z Axis

To test these results the following parameters were utilized as inputs to the model.

$$\bar{\rho} = [x_0 \quad 0 \quad x_0]^T \tag{3.24}$$

$$\dot{\bar{\rho}} = [0 \quad -2nx_0 \quad -nx_0]^T \tag{3.25}$$

where ρ and $\dot{\rho}$ correspond to the position and velocity of the inspector with respect to the target in the target's LVLH frame respectively. This results in an NMC with the shape shown in Figure 17, where the red x denotes the spacecraft's position at epoch.

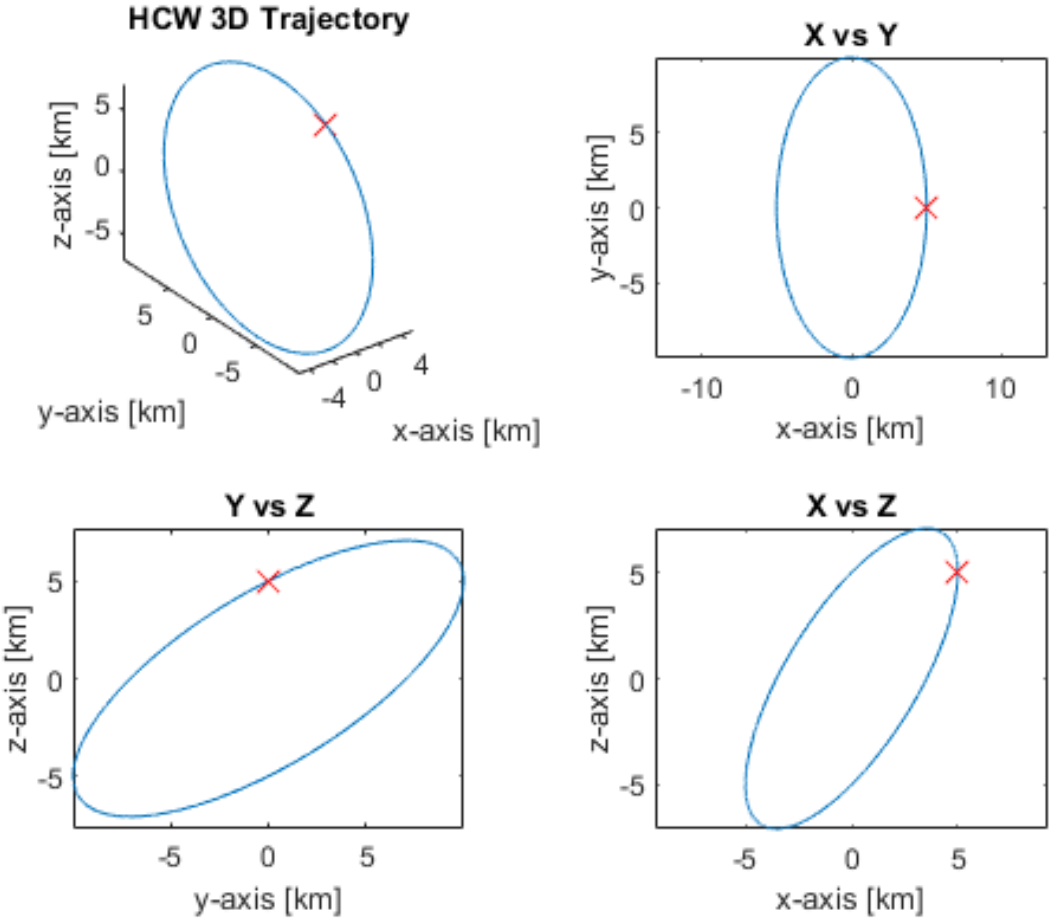

Figure 17. General NMC Trajectory

This is a significant result as it means that an inspector spacecraft can fly in a formation about a target seeing all six sides while utilizing extremely little fuel to maintain that formation in perpetuity. This method can now be tested against several different orbital regimes and values of x_0 in order to verify the predicted result as well as examine the added luminosity from the addition of the mirror constellation as opposed to only utilizing the Sun.

IV. Augmenting Lighting Conditions on Orbit Analysis and Results

4.1 Introduction

Due to the myriad of variables influencing this problem, creating an all-inclusive set of testing scenarios is impossible. Instead, the research is focused in two key areas. First, utilizing the NMC described previously to analyze the additional illumination provided by the reflector aboard the inspector satellite, as well as the required slew rates and angular accelerations, at various target orbits. Second, the size of the NMC is altered to show the quantity of illumination at various NMC sizes.

4.2 Results Altering Target Orbit

In order to meet this first objective, low Earth orbits and geosynchronous orbits are tested. In the LEO regime, two main orbits are modeled. A circular approximation of the ISS is used as a nominal orbit test case and a Sun-synchronous orbit is used as a best-case example. In the GEO regime, the case of the target satellite being in eclipse is used as a worst-case scenario and an entirely Sun lit condition is used as a best-case scenario.

For consistency the inspector will be in a NMC with initial position of $\rho = [5 \quad 0 \quad 5]^T$ -km with the initial velocity as defined previously, however the second test case will differ to show alternative benefits that will be discussed. It should be noted that the epoch for each scenario is 29 July 2021, other than the eclipsed geosynchronous test which is simulated on the equinox of 20 March 2021 to ensure the eclipse condition. These test cases are summarized in Table 3 below, with italic emphasis added for specialty cases.

Table 3. Varying Orbit Test Cases

Trial #	Orbit	Significance	Target	Inspector
1	LEO (July 29 2021)	ISS Type	$R = [6{,}798.137 \quad 0 \quad 0]^T$ $V = [0 \quad 4.7519 \quad 6.0045]^T$	$\rho = [5 \quad 0 \quad 5]^T$ $\dot{\rho} = [0 \quad -2nx_0 \quad -nx_0]^T$
2	LEO (July 29 2021)	ISS Type	$R = [6{,}798.137 \quad 0 \quad 0]^T$ $V = [0 \quad 4.7519 \quad 6.0045]^T$	$\rho = [5 \quad 0 \quad 5]^T$ $\dot{\rho} = [0 \quad -2nx_0 \quad -2nx_0]^T$
3	LEO (July 29 2021)	Sun Synch.	$R = [6{,}044 \quad 4{,}232 \quad 0]^T$ $V = [0.69 \quad -0.99 \quad 7.25]^T$	$\rho = [5 \quad 0 \quad 5]^T$ $\dot{\rho} = [0 \quad -2nx_0 \quad -nx_0]^T$
4	GEO (July 29 2021)	GEO - No Eclipse	$R = [42{,}166.2370 \quad 0 \quad 0]^T$ $V = [0 \quad 3.0746 \quad 0]^T$	$\rho = [5 \quad 0 \quad 5]^T$ $\dot{\rho} = [0 \quad -2nx_0 \quad -nx_0]^T$
5	GEO (*March 20 2021*)	GEO - Eclipse	$R = [42{,}166.2370 \quad 0 \quad 0]^T$ $V = [0 \quad 3.0746 \quad 0]^T$	$\rho = [5 \quad 0 \quad 5]^T$ $\dot{\rho} = [0 \quad -2nx_0 \quad -nx_0]^T$

For the first LEO test case, the target satellite was given an initial inertial position and velocity components as shown below.

$$\begin{aligned} \overline{R} &= [6{,}798.137 \quad 0 \quad 0]^T \\ \overline{V} &= [0 \quad 4.7519 \quad 6.0045]^T \end{aligned} \tag{4.1}$$

The plots of the NMC entered by the inspector satellite are shown in Figure 18 and Figure 19, with the red x denoting the starting position. Note that the NMC used throughout the following scenarios will appear identical in the chief's reference frame and therefore will not be plotted.

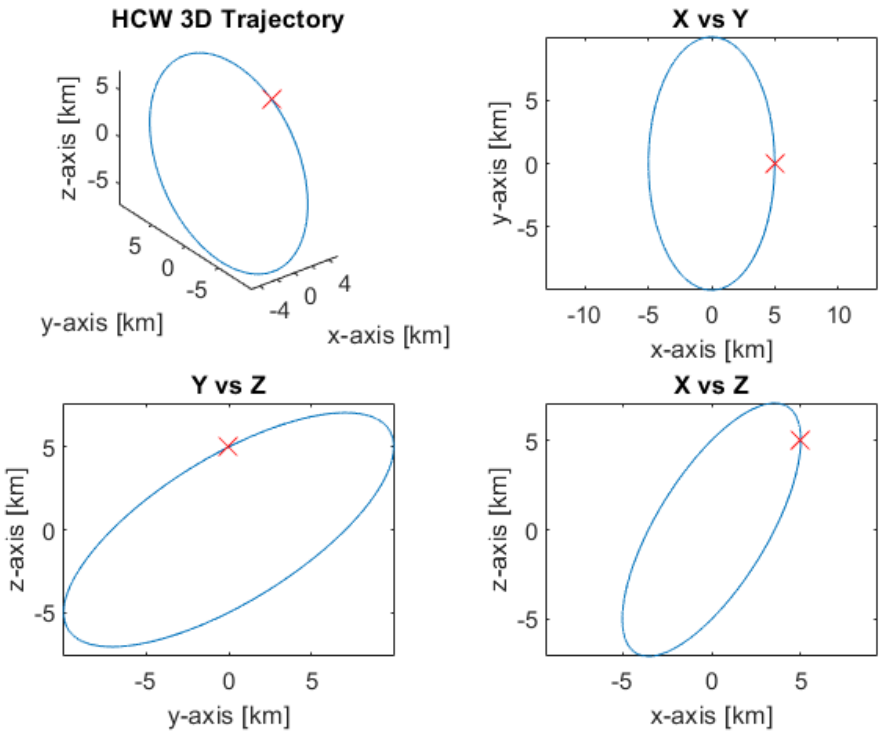

Figure 18. Trajectory Planes via HCW

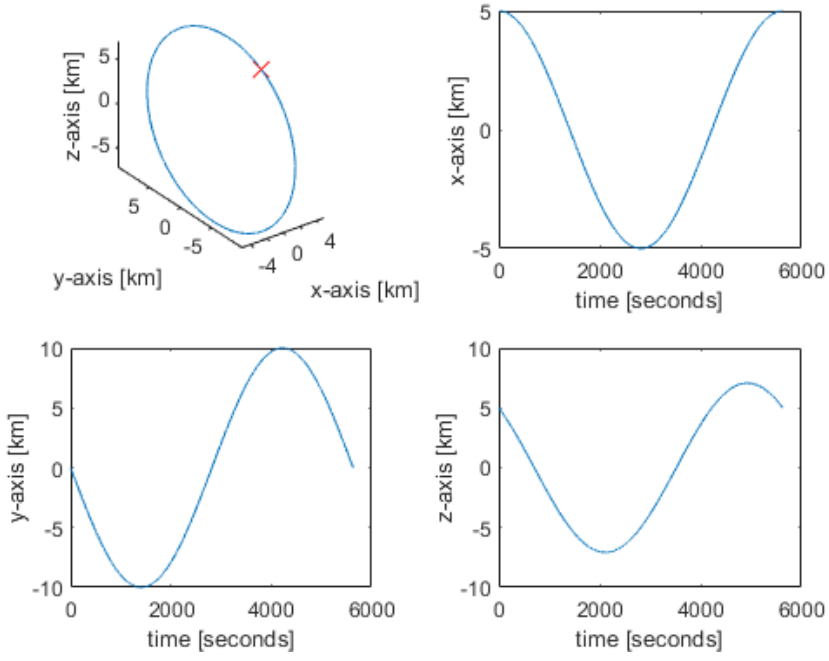

Figure 19. Trajectory vs Time via HCW

The inspector was able to illuminate and inspect five of six sides of the target even though it was not illuminated throughout the entire orbital period as shown in Figure 20 below.

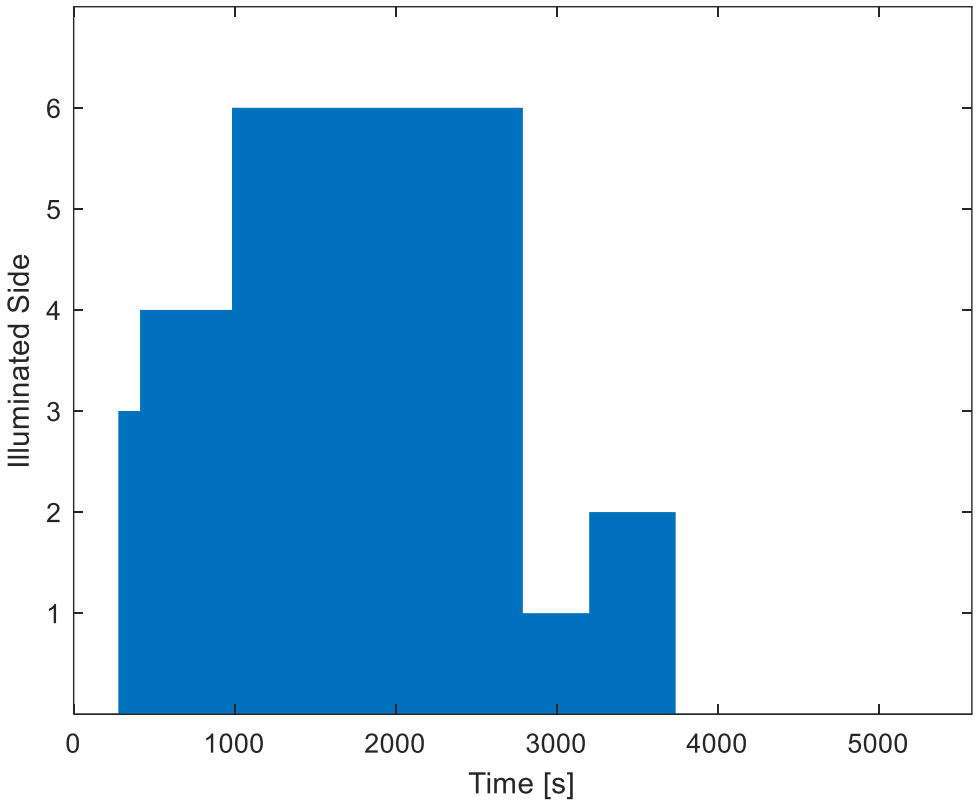

Figure 20. Trial 1 Illuminated Side over Time

The illumination quantity oscillated between approximately 50 lux at the minimum to approximately 120 lux at maximum as shown in the Figure 21 below, these results are promising as this is similar to the illumination experienced on an overcast day or at sunset on Earth.

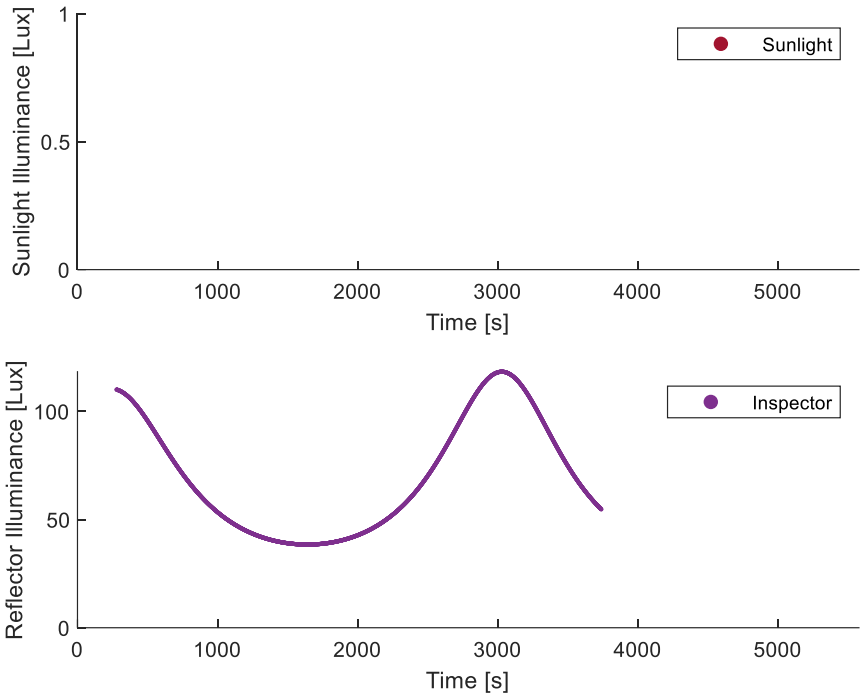

Figure 21. Trial 1 Illumination over Time

Reflecting sunlight from the Inspector's mirror directly onto the target occurred throughout over 60% of the orbit as displayed in Figure 22 below. It is interesting to note that sunlight did not illuminate the side of the target the inspector was on at any point in the orbit.

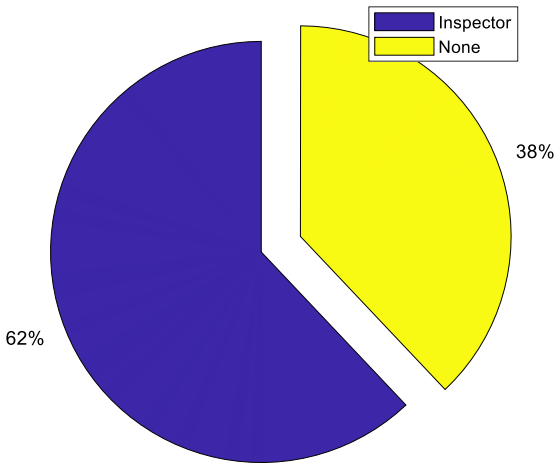

Figure 22. Trial 1 Illumination Source over Time

The slew rates and angular acceleration encountered in this maneuver are quite mild as shown in Figure 23 below, with a maximum slew rate of 5.51×10^{-2}-degree/second and a maximum angular acceleration of 2.50×10^{-4}-degree/second^2.

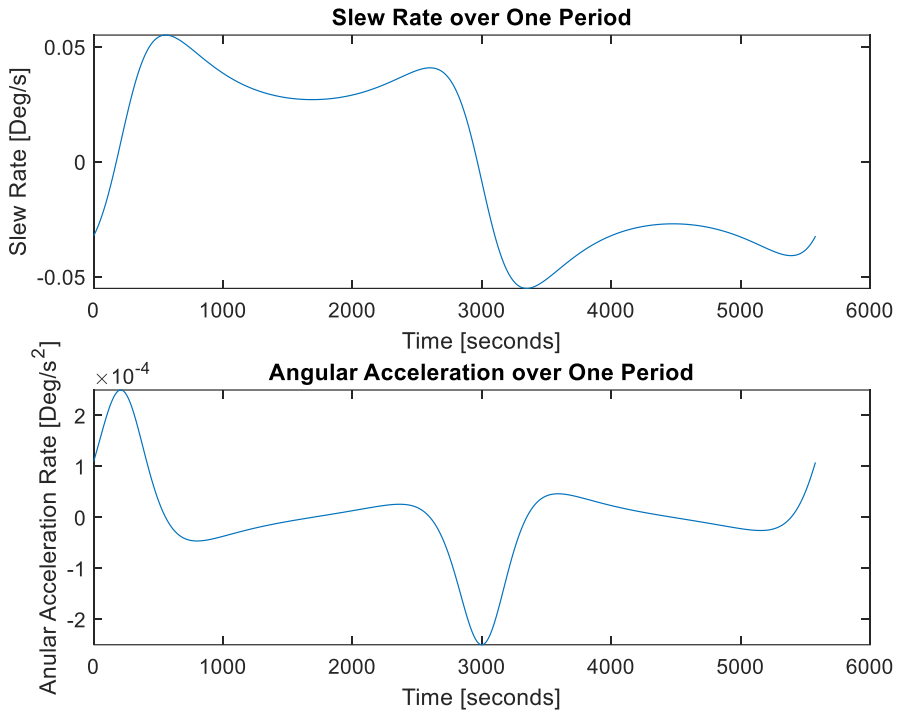

Figure 23. Trial 1 Slew Rate and Angular Acceleration

It should be noted that this NMC is not necessarily optimal but can provide the baseline for defining an optimal NMC based on more narrowly defined mission requirements such as equal dwell time per side, equal illumination per side, or many other such situations. For example, should the initial velocity be adjusted such that $\dot{\bar{\rho}} = [0 \quad -2nx_0 \quad -2nx_0]^T$ -km/s the results change significantly. Though the sides seen per time are quite similar as shown in Figure 24, there is the addition of sunlight such that all six sides can now be seen. At approximately 3,400 seconds where trial one lost illumination this NMC allows for side five to be seen. This sunlight can also clearly be seen in Figure 25 below.

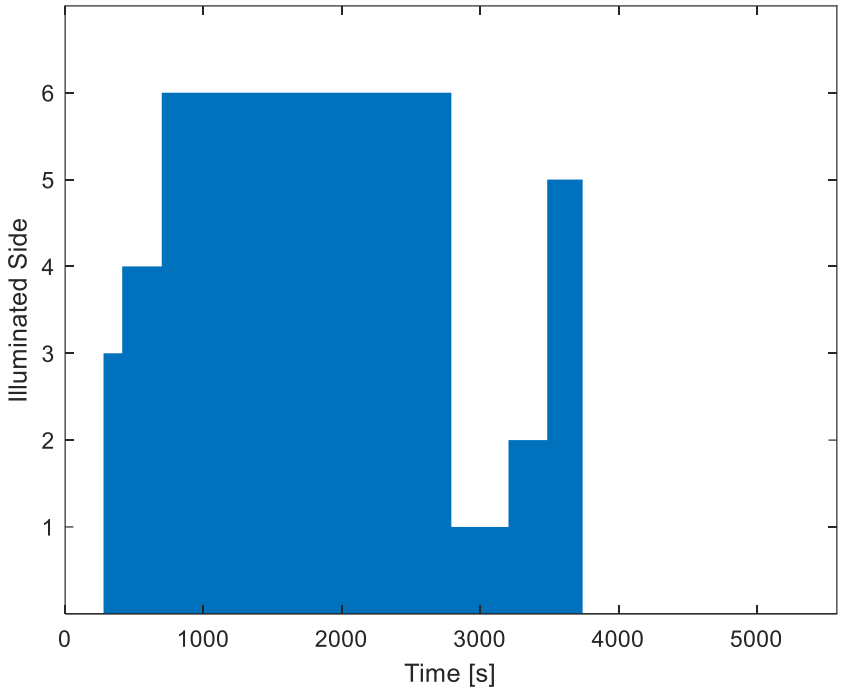

Figure 24. Trial 2 Illuminated Side over Time

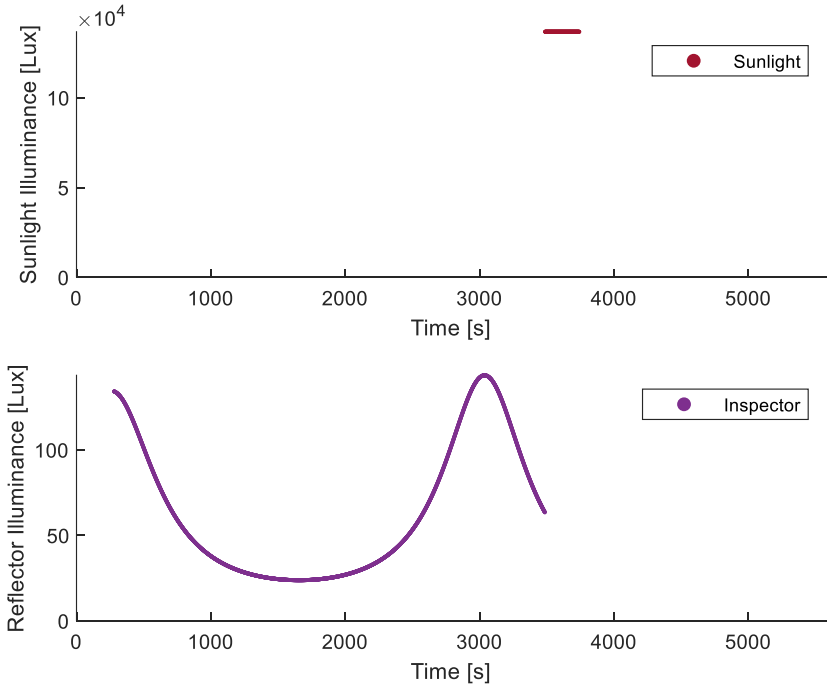

Figure 25. Trial 2 Illumination over Time

In total, direct illumination from the Sun is only present throughout 5% of the period, but this small amount enables imaging of all six sides of the target spacecraft.

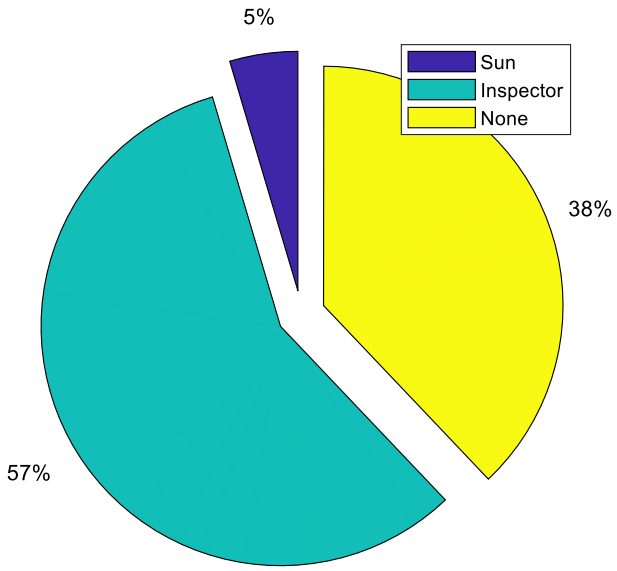

Figure 26. Trial 2 Illumination Source over Time

Trial 2 does have a slightly higher slew rate and angular acceleration than Trial 1, with a maximum slew rate of 8.23×10^{-2}-degree/second and a maximum angular acceleration of 6.27×10^{-4}-degree/second^2 as shown in Figure 27.

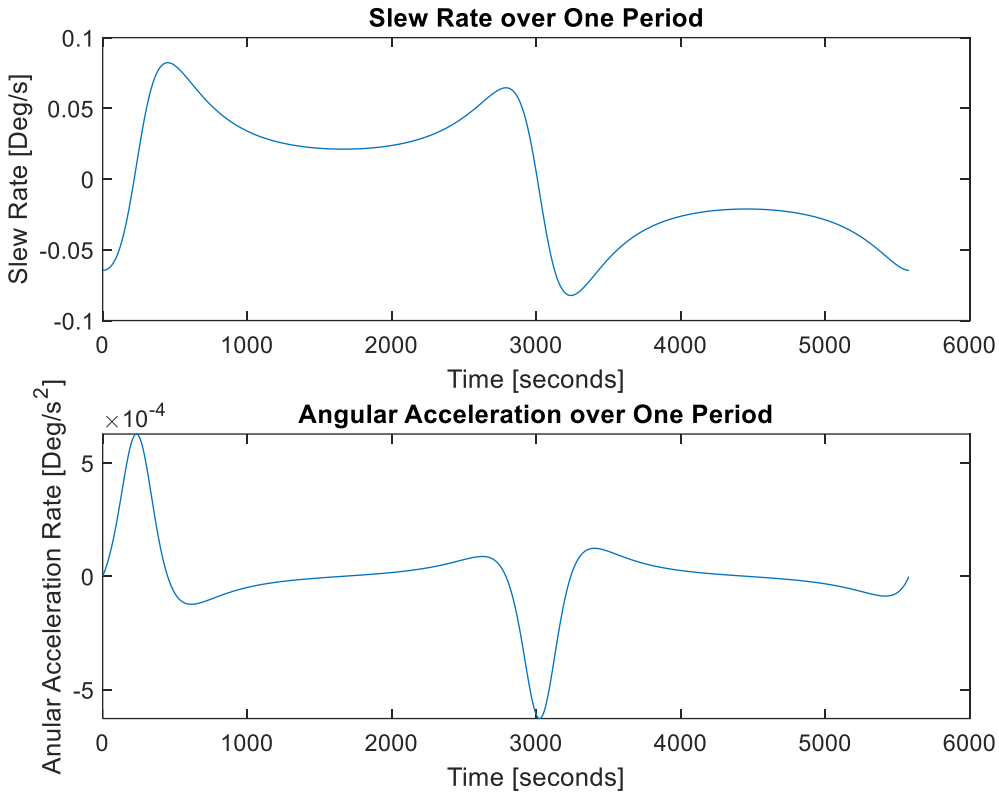

Figure 27. Trial 2 Slew Rate and Angular Acceleration

Trial 2 demonstrates that though a reflector is an enabling technology for inspection missions, ultimately nothing can replace mission planning. With only a slight change in the NMC the inspector was successfully able to image all six sides of the target with favorable conditions. These trials also demonstrate that an NMC as described previously utilizing a reflector attached to an inspector can see all six sides of a target spacecraft in an orbit similar to the ISS while constrained to the +/-45-degree illumination condition.

Trial 3 consists of testing an example of a best-case orbit, a Sun-synchronous orbit with an altitude of 1000-km such that the chief spacecraft never enters eclipse. The Chief's initial states are given below.

$$\bar{R} = [6{,}044 \quad 4{,}232 \quad 0]^T$$
$$\bar{V} = [0.69 \quad -0.99 \quad 7.25]^T \tag{4.2}$$

As expected, all six sides of the spacecraft are easily seen as in Figure 28 below.

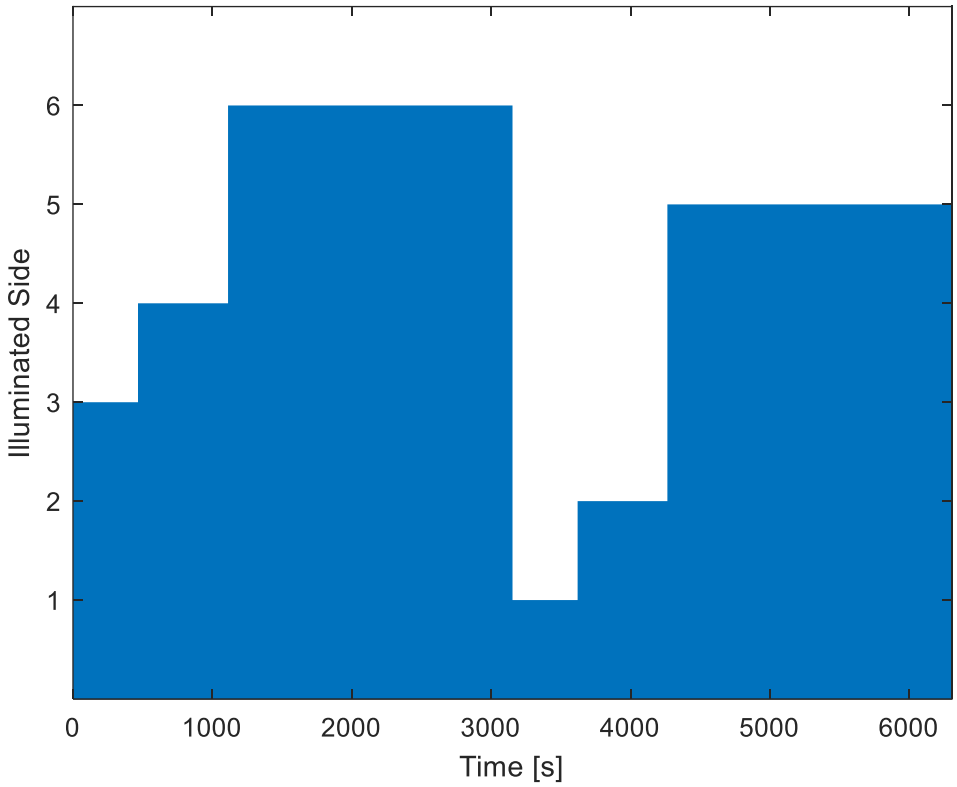

Figure 28. Trial 3 Illuminated Side over Time

The illumination quantity shown in Figure 29 also shows that the natural sunlight can augment the inspector's reflector throughout one of the lower illumination troughs. In total, the sunlight accounts for approximately 16% of the illumination throughout the orbit as shown in Figure 30.

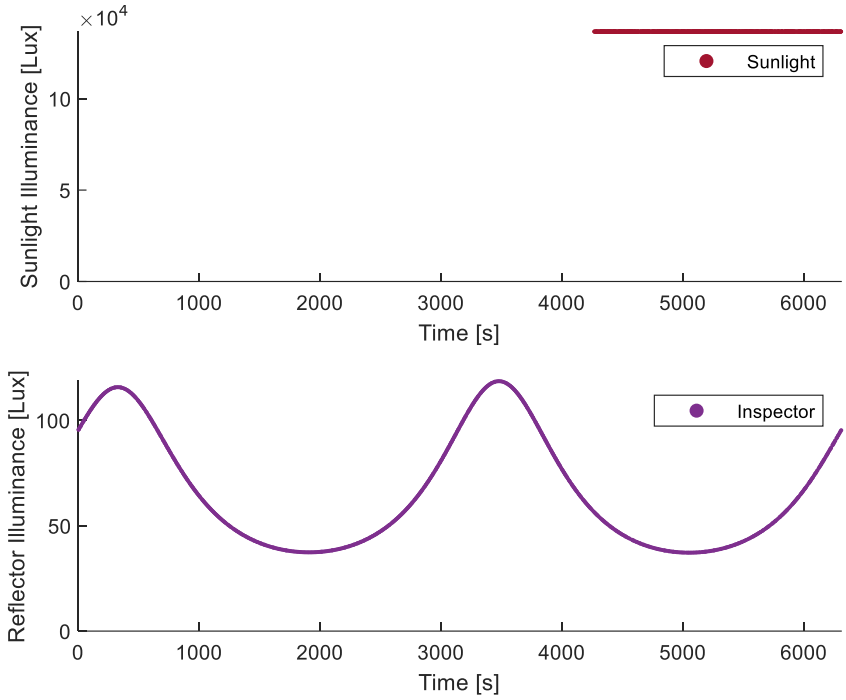

Figure 29. Trial 3 Illumination over Time

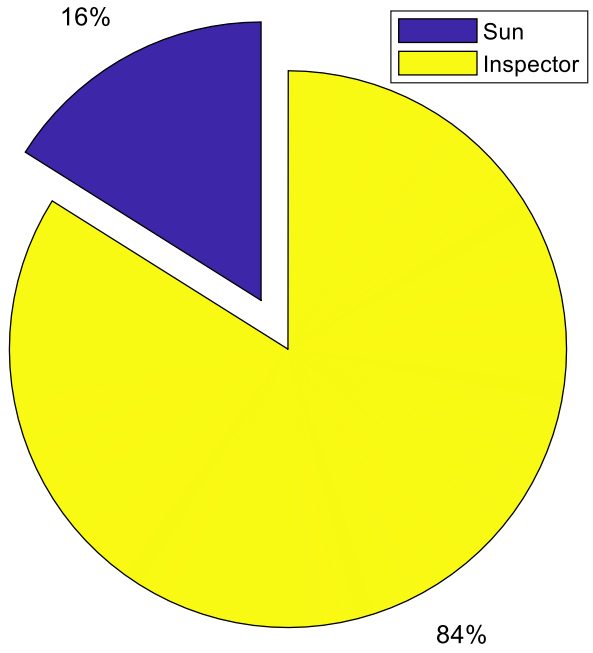

Figure 30. Trial 3 Illumination Source over Time

This orbit also experiences lower slew rates and angular acceleration due to having a longer period than the lower altitude orbits from trials 1 and 2, with a maximum slew rate of $4.87\text{x}10^{-2}$-degree/second and a maximum angular acceleration of $1.96\text{x}10^{-4}$-degree/second^2 as shown in Figure 31.

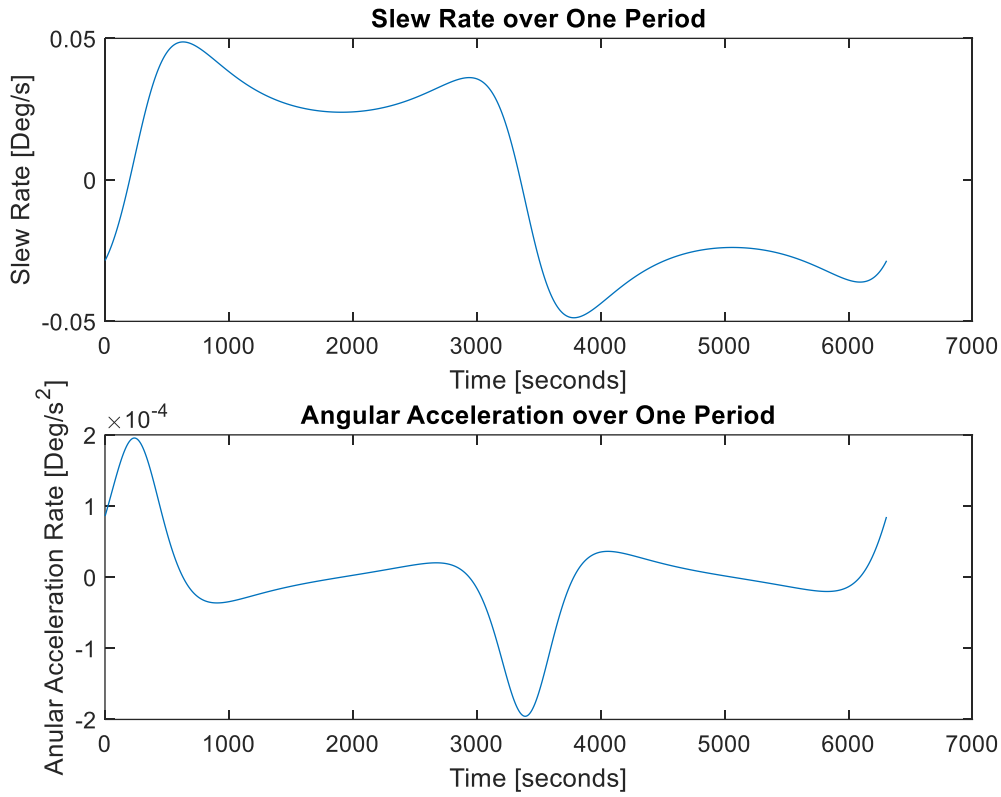

Figure 31. Trial 3 Slew Rate and Angular Acceleration

The next target orbit considered is a geostationary satellite in a daylit condition throughout the entirety of its orbit. The initial states for the target spacecraft are given below.

$$\begin{aligned} \overline{\mathrm{R}} &= [42{,}166.2370 \quad 0 \quad 0]^{\mathrm{T}} \\ \overline{\mathrm{V}} &= [0 \quad 3.0746 \quad 0]^{\mathrm{T}} \end{aligned} \tag{4.3}$$

in this scenario, the target spacecraft is illuminated for the entire duration of the pass as shown in the Figure 32 below.

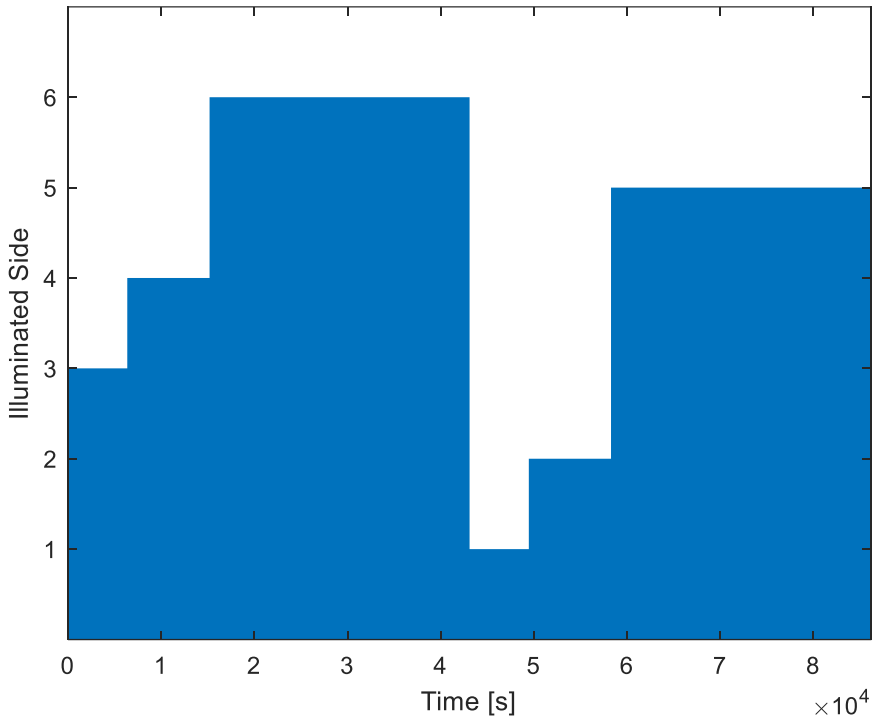

Figure 32. Trial 4 Illuminated Side over Time

The quantity of illumination is similar to trial 3, with natural sunlight augmenting approximately 3% of the NMC period at various intervals as shown in Figure 33 and Figure 34.

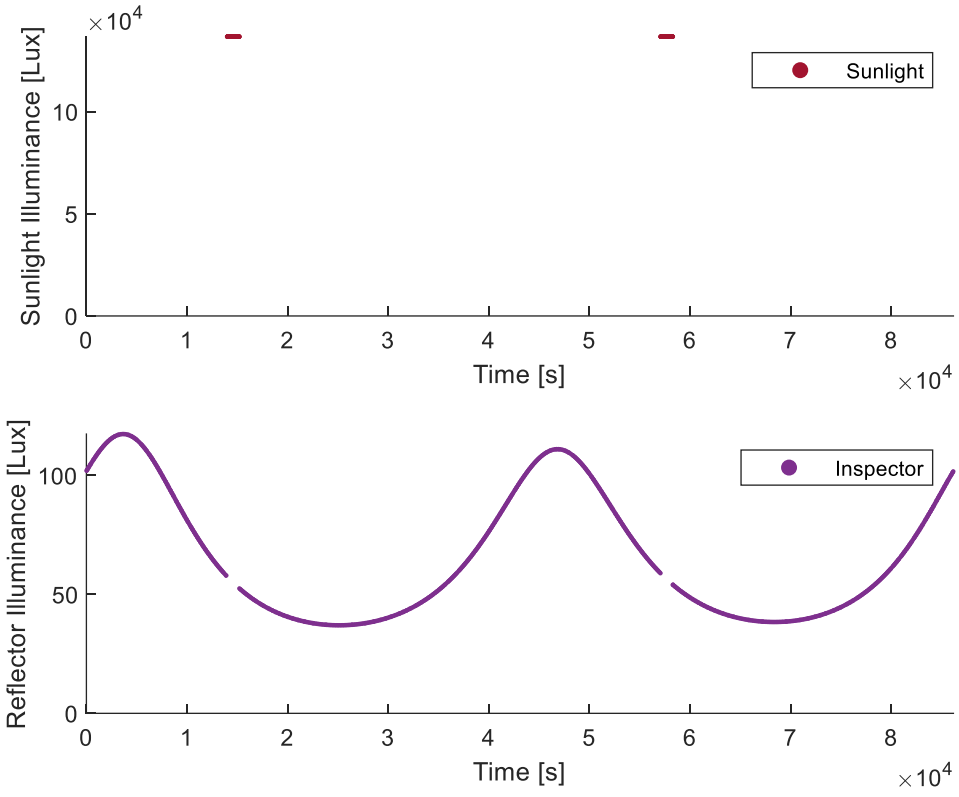

Figure 33. Trial 4 Illumination over Time

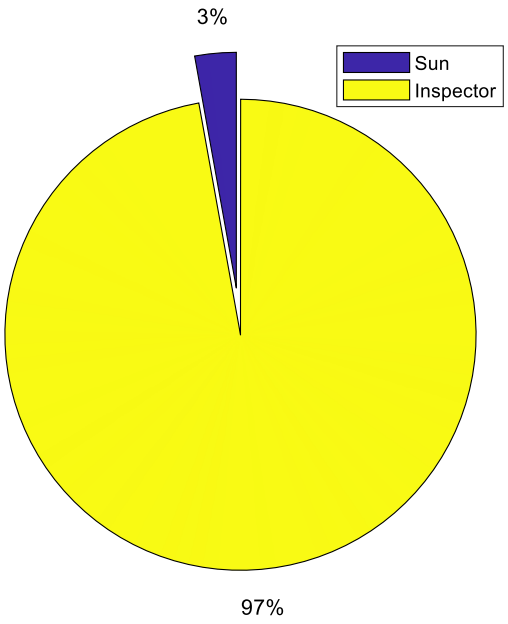

Figure 34. Trial 4 Illumination Source over Time

The slew rates and angular acceleration are the lowest yet, due to having an entire day to complete the path around the NMC. This yields a maximum slew rate of $3.6x10^{-3}$-degree/second and a maximum angular acceleration of $1.05x10^{-6}$-degree/second^2 as shown in Figure 35. It should be noted that trial 4 and 5 are in the same orbit, therefore the slew rates and angular acceleration will be the same and will not be displayed again for sake of brevity.

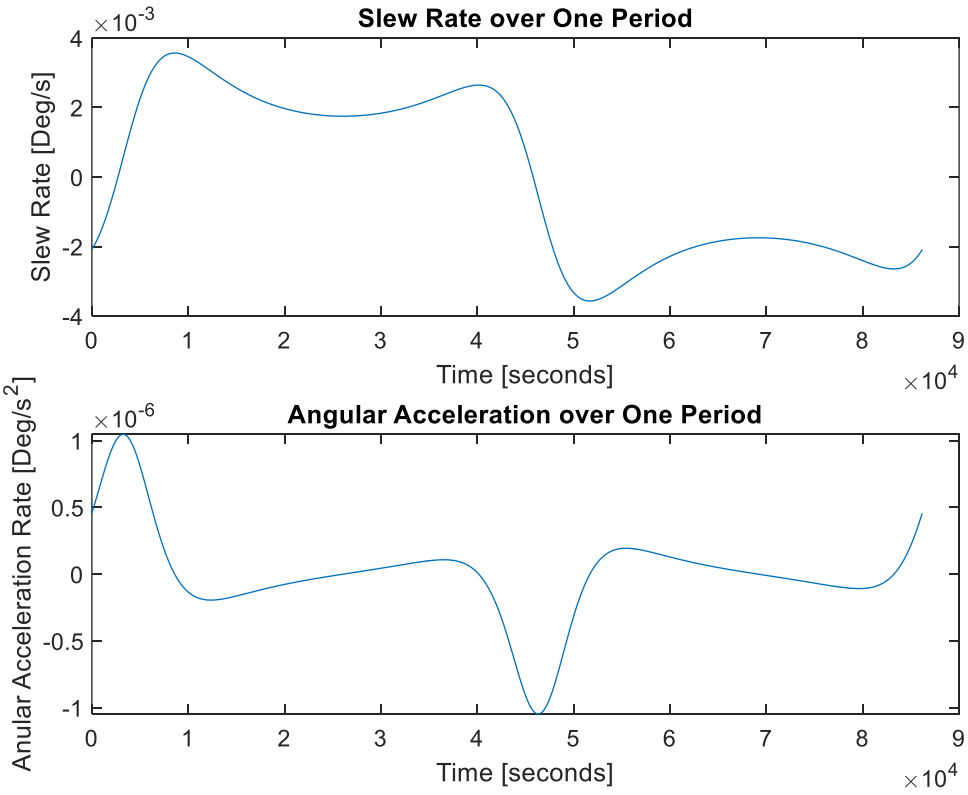

Figure 35. Trial 4 and 5 Slew Rate and Angular Acceleration

Also of note is that this slew rate is an order of magnitude lower, and the angular acceleration is two orders of magnitude lower, than the previous LEO trials.

The final target orbit considered is a geostationary satellite during the spring equinox, such that it experiences an eclipse of approximately 67 minutes. The initial states for this orbit are the same as trial 4, however the epoch time has changed to March 20th 2021. Ultimately, the inspector was still able to see all six sides of the target spacecraft and met the illumination conditions throughout approximately 96% of the target period. These results are shown in Figure 36, Figure 37, and Figure 38.

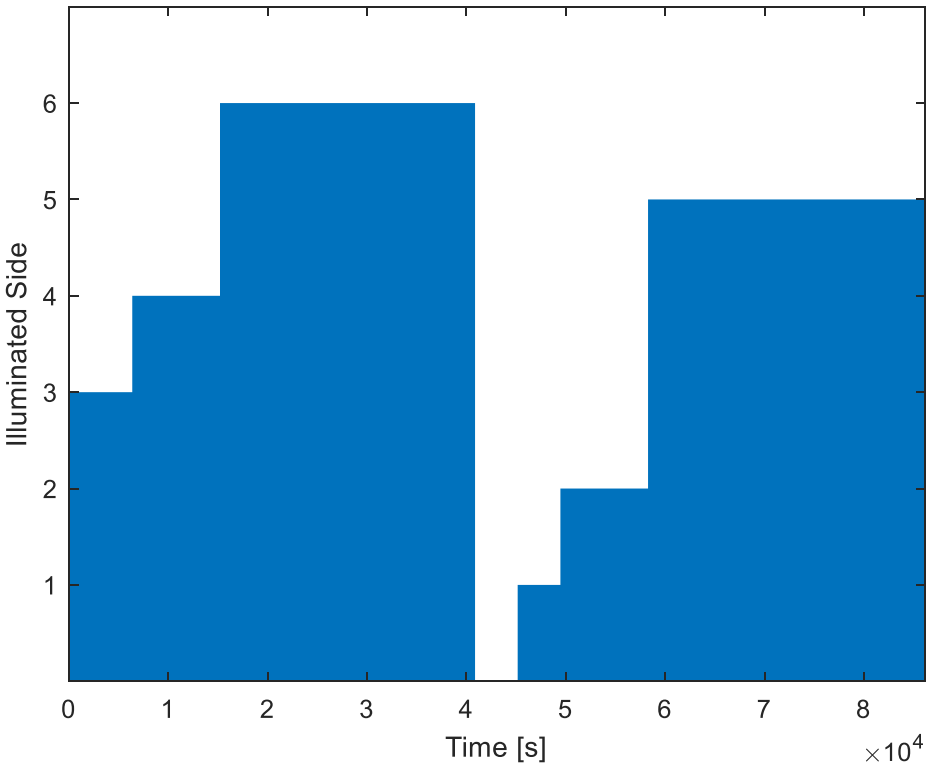

Figure 36. Trial 5 Illuminated Side over Time

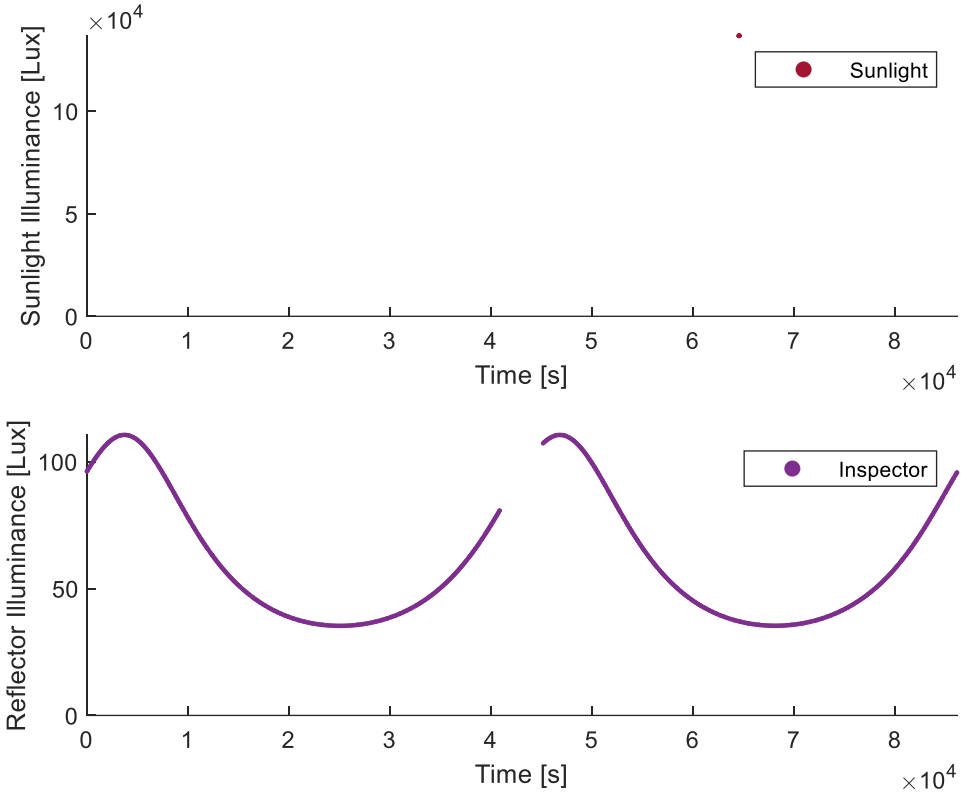

Figure 37. Trial 5 Illumination over Time

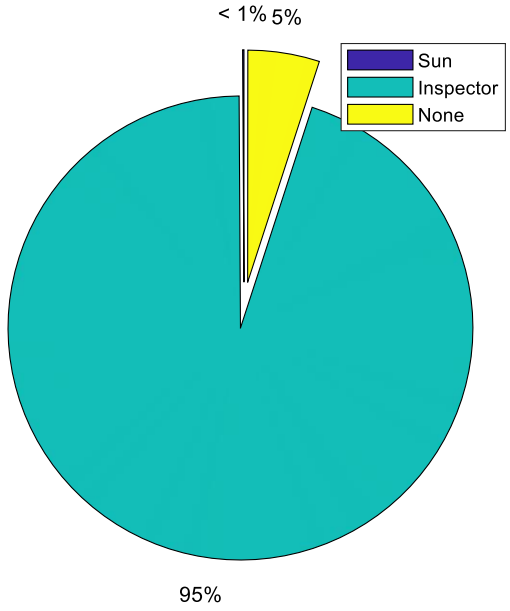

Figure 38. Trial 5 Illumination Source over Time

In all but trial 1 the inspector was successfully able to image each of the six sides of the target spacecraft with the source of illumination being within +/- 45-degrees from the line normal to each side of the target spacecraft. In trial 1, only five sides were successfully imaged, however with a minor alteration of the NMC as shown in trial two the revised NMC was able to successfully meet the imaging requirements for all sides. The greatest illumination for most of these orbits was direct sunlight and the lowest was equivalent to a sunset experienced on Earth. This is a significant result as it implies that using the reflector described, the opportunities for ideal lighting conditions for proximity operations can be expanded immensely. More analysis on these results will be provided in section 4.4. The following section will examine the effect of varying the NMC size on the illumination given a 1-m radius reflector attached to the inspector.

4.3 Results Altering NMC Size

In order to meet the second objective, the NMC size is altered using the x_0 initial condition and the change in illumination quantity is recorded. The orbit used in trial 4 was chosen for this round of testing since the target is constantly in a sunlit condition. The NMC x_0 initial condition is tested at 0.1, 0.5, 1, 5, 10, 50, and 100-km, and the maximum and minimum illumination conditions are recorded. It should be noted that the slew rate and angular acceleration are invariant to the NMC size. The inspector must travel 360-degrees about the target within one period, therefore the period of the target spacecraft is the only factor that effects the slew rates and associated angular velocities. The results of this testing are summarized in Table 4.

Table 4. Maximum and Minimum Illumination Value

x_0 [km]	NMC Seminor Axis [km]	NMC Semimajor Axis [km]	NMC Average Distance [km]	Min Illumination [lux]	Max Illumination [lux]
0.1	0.1303	0.2303	0.1838	92,526	136,770
0.5	0.6514	1.1514	0.9188	3,702	136,770
1	1.3028	2.3028	1.8376	925	136,770
5	6.5139	11.5139	9.1880	37	136,770
10	13.0278	23.0278	18.3760	9	136,770
50	65.1388	115.1388	91.8802	0.37	136,770
100	130.2776	230.2775	183.7603	0.09	136,770

The illumination quantity decreases exponentially as the NMC size is increased. While required illumination quantity is mission dependent, a few key observations can be made. In the case of $x_0 = 0.1$ -km the illumination is approximately equivalent to full daylight under a clear sky on Earth. As the range is increased to $x_0 = 10$ -km the illumination has dropped to approximately a sunset condition on Earth. Anything between 0.5-1-lux is relatively minimal illumination and is similar to the light on Earth under a full Moon on a clear night. The implications of these values will be summarized in section 4.4.

4.4 Discussion

In the previous sections it was demonstrated that an inspector spacecraft with a 1-m radius reflector can successfully accomplish the four goals described previously:

1. Image all six sides of a target
2. Constrain the incident illumination to within +/- 45-degrees from the line normal to each side of the target spacecraft
3. Perform this maneuver within one period of the target spacecraft

4. Perform this maneuver with minimal fuel (i.e., under natural motion as defined by the classic Two Body Problem)

This would not be the case if only natural sunlight was available. Meeting these conditions from sunlight alone is rare, as shown in Table 5.

Table 5. Percent of Period Sunlight and Inspector Mirror Meet Goals

Trial #	Sunlight	Inspector Mirror	Sunlight plus Inspector Mirror
1	0	62%	62%
2	5%	57%	62%
3	16%	84%	100%
4	3%	97%	100%
5	1%	95%	96%

While it is noted that the scenario is not optimized for natural illumination inspections, one of the goals of this research is to minimize the requirements levied on inspection missions.

As mentioned previously, the use of large reflector spacecraft in Sun-synchronous orbits, both with and without collimating ability, to use along with the inspector with a flat-plane mirror were also examined. Interestingly, the testing results also show that the majority of the utility of this constellation is gained from simply equipping the inspector with its own reflector and reflecting the sunlight directly onto the target. This result is even more pronounced in the GEO regime. As summarized in Table 5, using only the natural sunlight and the inspector's mirror the inspection goals are met over 96% of the period.

This result is significant as it vastly simplifies the infrastructure needed to perform the inspection. Though large reflectors are feasible with modern technology, the resources required to bring them to fruition is formidable. Instead, a smaller lightweight reflector can be attached to the inspector spacecraft. Using the areal density determined by NASA, the 1-m reflector used in the simulation would weigh under 45 grams [6]. Even small CubeSat

programs can host a mirror of this mass. The slew rates are also very manageable. As a pragmatism *The Space Mission Engineering: The New SMAD*, qualifies slew rates between 0.05-0.5-degrees/second as minimal and capable of being performed with reaction wheels [33]. Even the highest slew rate encountered in testing (0.0823-degrees/second) is well under this upper limit. Reaction wheels are also extremely precise, with typical accuracies ranging from +/-0.0001 to 1-degree and have typical torque abilities from 0.01 to 1-Nm [33].

Using the lower limit of this torque ability and the maximum angular acceleration experienced from trial 2, this allows for a moment of inertia about the axis of rotation for the reflector system of 913.8-kg-m^2. This reflector would not need to rotate about the mirror's axis of symmetry, but rather about the two axes perpendicular to the axis of symmetry. It should be noted that depending on image orientation requirements, it may also be possible to only use one degree of freedom rotation for the reflector and allow the spacecraft bus to control the second required rotational degree of freedom. The moment of inertia equation for circular flat reflector is similar to that of a thin disk as given in Equation 4.4 below, where M is the total mass of the disk and r is the radius of the disk.

$$\mathrm{I_x} = \mathrm{I_y} = \frac{1}{4}\mathrm{Mr} \tag{4.4}$$

Substituting the areal density, χ, of the reflector multiplied by the reflector area for the total mass results in Equation 4.5.

$$\mathrm{I_x} = \frac{1}{4}(\chi \cdot \pi * r^2)\mathrm{r} = \frac{\chi \cdot \pi}{4} r^3 \tag{4.5}$$

NASA estimates the areal density of an aluminum-Kapton reflector to be 14-g/m^2. Solving this equation to find the maximum reflector radius, results in a reflector radius of 4.36-m.

It should be noted that even this large mirror is based on very conservative estimates of reaction wheel abilities.

Making the mirror larger is one of two methods of increasing the illumination on target as described in Table 4. The second option is simply to fly in closer proximity to the target. Even the smallest NMC tested ($x_0 = 0.1$ -km) only flies within 130-m of the target spacecraft. With modern technology, even CubeSats have demonstrated the ability to fly with 20-m of their target [31]. Creating the appropriate lighting conditions for a specific mission can be accomplished by tuning the two design variables of reflector size and NMC size.

4.5 Summary

In this chapter, the simulation developed in Chapter III was utilized to test the inspection of targets in a variety of orbital regimes. The reflector constellation was shown to be able to meet all the four of the mission goals. The results of this research show that the concept of large reflectors in Sun-synchronous orbit may be abandoned without detrimental effects. This vastly simplifies the infrastructure and mission design requirements. Large, low mass solar reflectors have been shown to increase satisfactory imaging conditions by approximately 60% in LEO and 95% in GEO. These mirrors are easily realizable with modern technology. The flexibility and low mass of these mirrors shows specific promise for CubeSat inspection programs.

In conclusion, for inspection missions with strict lighting conditions it is recommended that the inspector spacecraft be equipped with a lightweight flat plane membrane mirror. The reflector should be designed for two degree of freedom rotation in

order to track between the Sun vector and the target spacecraft. A reflector of this description would be extremely lightweight and easily controlled. Though further work will certainly be required to mature this technology, it has potential to drastically increase on-orbit illumination and transform current rendezvous and proximity operation techniques.

V. Novel Orbit Determination Methodology

5.1 Introduction

A novel method of preliminary satellite orbit determination is presented utilizing a union of the techniques used in astronomical occultation analysis, short arc orbit determination techniques integral to asteroid orbit determination, and satellite optical tracking. Departing from the convention of employing ground- and/or space-based radar to obtain angle and position data for near-Earth orbit determination, such information is instead obtained by using a combination of ground or space-based visual light sensor and a space-based mirror. In this new method, the space-based mirror reflects light towards the Earth and the resultant illumination disk is observed for the transit of satellites or other resident space objects. The sensor observes the passing shadow of the satellite or RSO and directly computes the relative position of the object casting the shadow to the space-based mirror.

Traditionally, the problem of orbit determination based on azimuth and elevation data has been handled using classical angles-only orbit determination techniques, such as Laplace's or Gauss's Method. The proposed system creates a novel orbit determination technique using the known geometry of the space-based reflector, illumination disk optical data, and a linearized orbit model. The accuracy of this novel method will be compared with traditional orbit determination techniques for accuracy and to determine applicability for different orbital regimes. This method would meld the advances made in the astronomy field with that of near-Earth orbit determination and could provide particular benefit to spacecraft lost after initial orbit insertion.

This method functions on a satellite or RSO that passes through the illumination cone provided by the reflected light from the space-based mirror. The resultant shadow is then observed. Using basic trigonometry, a relative position vector from the space-based mirror to the transiting object is then created utilizing the position of the centroid of the observed shadow and trigonometric data. This relative position vector in the space-based mirror's body reference frame is then converted to the Earth-centered inertial frame. The relative position vector is then added to the position vector of the space-based mirror to result in the position vector of the RSO. Using a linearized model and a high frequency optical sensor the velocity vector of the spacecraft or RSO can then be derived. Having computed an Earth-centered inertial position and velocity vector, the RSO's classic two body orbit is then fully determined and can be propagated both forward and backward in time.

An astrodynamicaly accurate software simulation has been developed to create a video upon which to test this technique. This program takes inputs of the space-based mirror's and RSO's classical orbital elements (COEs) and optical sensor parameters and outputs a video simulation and the propagated position data of the space-based mirror. These outputs are then fed into a second software program to analyze the video using the novel orbit determination technique developed herein and outputs the COEs of the RSO. The results from this software will then be compared to show the efficacy of this novel orbit determination technique. Circumstances under which this novel method may prove particularly advantageous will be discussed. The method proposed is deterministic in nature. In order to increase the efficacy of this model, the research in occultation solutions and short arc orbit determination must be melded.

5.2 Initial Orbit Determination Algorithm

The first step in this novel IOD method is to observe the shadow cast by a RSO travelling through the illumination cone provided by the space-based illumination source. The illumination cone will be assumed to be pointing nadir for the purposes of this chapter. This cone will have an opening angle equal to the solar angular diameter at Earth hereon referred to as α, which is approximately constant throughout Earth's orbit with a value of 0.0093 radians [5]. This illumination cone will intersect with the surface of the Earth, assumed to be flat over the length of the resultant illuminated circle on the Earth. Any object traveling through the illumination disk will then cast a shadow onto the Earth. The projection of this shadow on the Earth will be an ellipse throughout the transit, or circular should the RSO pass directly underneath the reflector. Figure 39 provides a two-dimensional representation of the transit.

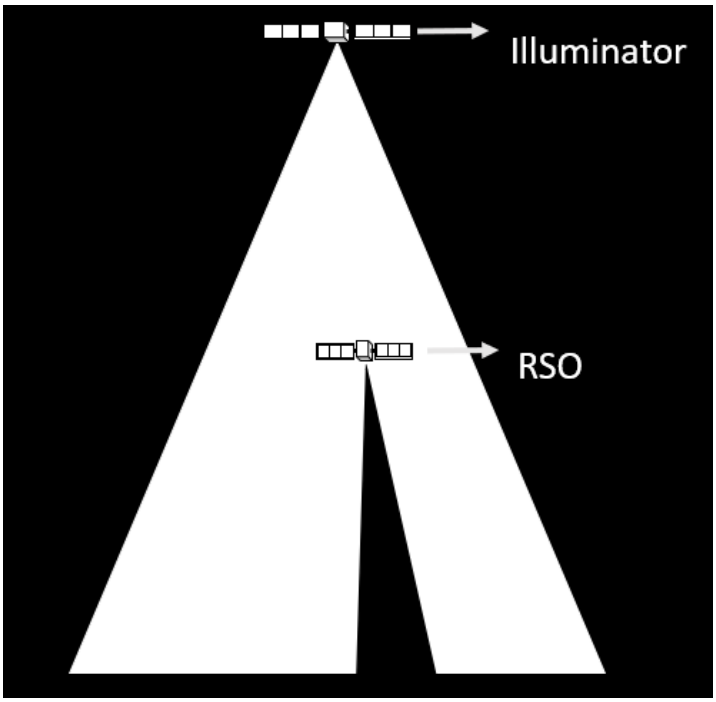

Figure 39. Two-Dimensional Transit Geometry

In the following analysis two orbital frames of reference will be utilized. The first is the Earth-centered inertial (ECI) frame defined as $\hat{e_1}$ pointing towards the vernal equinox, $\hat{e_2}$ pointing perpendicularly eastward, and $\hat{e_3}$ completing the right-handed coordinate frame. The second is a reflector satellite fixed local-vertical-local-horizontal (LVLH) frame defined as $\hat{e_1}$ pointing in the negative radial direction, $\hat{e_3}$ in the negative orbit normal direction, and $\hat{e_2}$ completes the right-handed coordinate frame. The shadow ellipse cast onto the Earth must be measured to determine the semiminor and semimajor axes of the ellipse (b and a, respectively), the position of the centroid in the second and third dimension of the LVLH frame (the first dimension, essentially depth, is unknown at this point). These quantities can be determined by use of a space-based sensor or ground based luminosity detector system.

In order to find the relative position of the RSO with respect to the illuminator, the altitude of the RSO above the Earth is first calculated using the geometry of the shadow ellipse. When the transit geometry is observed perpendicular to the shadow ellipse minor axis in two dimensions the shadow appears to form an isosceles triangle as shown in Figure 40.

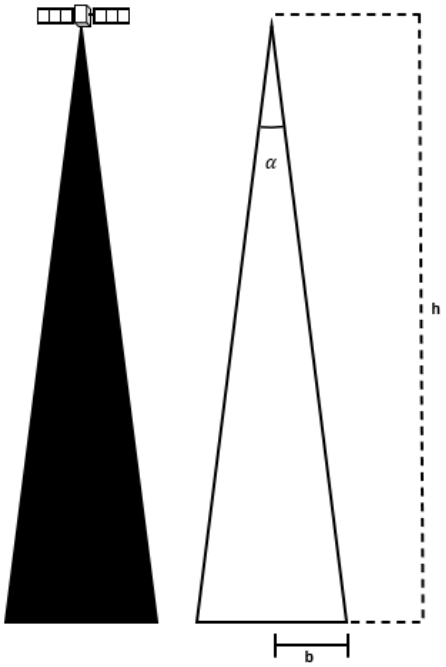

Figure 40. Two-Dimensional Minor Axis View of Shadow Geometry

Using this view, the altitude of the RSO (*h*) can clearly be determined from the trigonometric relationship shown in Equation 5.1.

$$\mathrm{h} = \frac{\mathrm{b}}{\tan(\alpha)} \tag{5.1}$$

The RSO's altitude can then be used in order to calculate the position of the RSO with respect to the shadow ellipse's centroid (at the intersection of sides ρ and a in Figure 41).

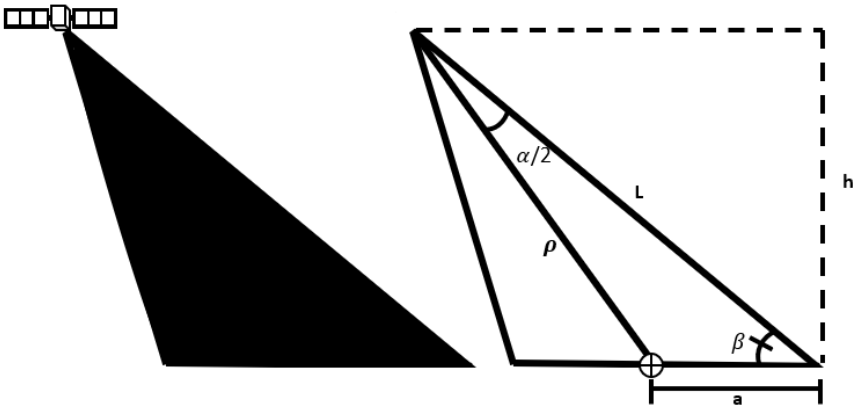

Figure 41. Two-Dimensional Major Axis View of Shadow Geometry

If the position of the centroid of the shadow is known, then the distance from the RSO to the shadow centroid ρ must be calculated in order to fully define the three-dimensional position of the RSO. The values of L and β determined through knowledge of h found from Equation 5.1, the constant α, and the semimajor axis length. This geometry problem then reduces through defining two equations and two unknowns which can then be solved simultaneously as shown in Equations 5.2 and 5.3 below. Equation 5.2 is a simple trigonometric identity for the right triangle with h as a side and L as the hypotenuse and Equation 5.3 is an application of the Law of Sines on the triangle ρ-a-L.

$$\cos(\beta - 90^0) = \frac{\mathrm{h}}{\mathrm{L}} \tag{5.2}$$

$$\frac{\mathrm{a}}{\sin(\alpha)} = \frac{\mathrm{L}}{\sin(180^0 - \alpha - \beta)} \tag{5.3}$$

With quantities L and β known, τ can be calculated through the use of the Law of Cosines as shown in Equation 5.4.

$$\tau = \sqrt{\mathrm{a}^2 + \mathrm{L}^2 - 2\mathrm{aL}\cos(\beta)} \tag{5.4}$$

The relative position of the RSO with respect to the illuminator is then shown in Equation 5.5, with $C_{\odot}(2)$, $C_{\odot}(3)$ being the shadow center position in the LVLH frame $\hat{e_2}$ and $\hat{e_3}$ directions, respectively.

$$[\overline{R}_{rel}]^{LVLH} = \begin{bmatrix} [R_{illuminator} - (R_{\oplus} + h) \\ C_{\odot}(2) - \tau * \hat{R}_{C_{\odot}}(2) \\ C_{\odot}(3) - \tau * \hat{R}_{C_{\odot}}(3) \end{bmatrix} \tag{5.5}$$

A series of rotations can then be used to convert this vector from the LVLH frame into the ECI frame. With this relative position vector in the ECI frame, simple vector addition can be used to ultimately calculate the position of the RSO in inertial space as shown in Figure 42 and Equation 5.6. This technique can be used to calculate the inertial position vector of the RSO at each data point.

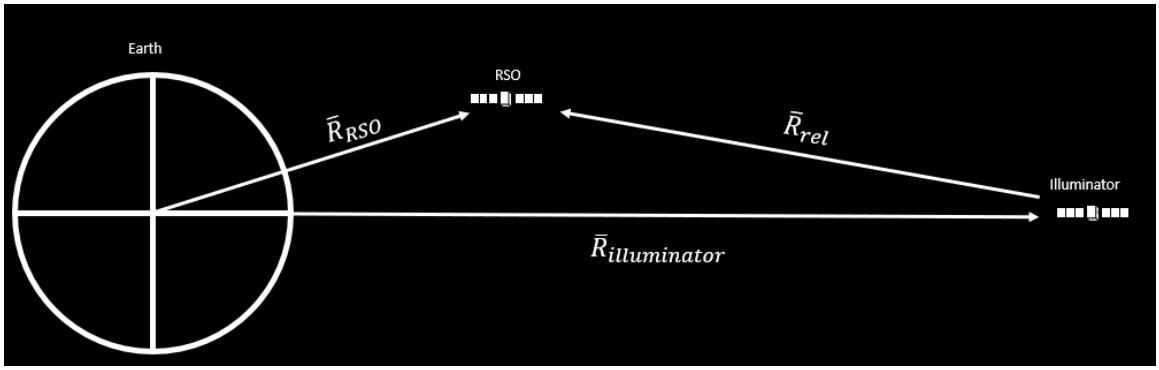

Figure 42. Vector Geometry Representation

$$\overline{R}_{RSO} = \overline{R}_{illuminator} + \overline{R}_{rel} \tag{5.6}$$

Three methods of velocity calculation are used in conjunction with this technique to test for efficacy within the low Earth orbit (LEO) regime: namely linearization, circularization, and the Herrick-Gibbs method. Knowing both a current and a past inertial

position vector for the RSO and assuming a sufficiently short time step, the linear velocity vector can be approximated as shown in Equation 5.7.

$$\bar{V}_{RSO}(k) = \frac{\bar{R}_{RSO}(k) - \bar{R}_{RSO}(k-1)}{\Delta t} \tag{5.7}$$

Most objects in LEO have very low eccentricities due to their proximity to Earth, as a high eccentricity at this point would force the RSO into atmospheric reentry. This provides a second method, similar to linearization, but instead assuming circular travel within the time step. A change in the inertial position vector ($\widehat{\Delta R}$) is calculated as shown in Equation 5.8. The average position vector is then used to calculate a scalar circular velocity which is then projected onto the change in $\widehat{\Delta R}$ as given by Equation 5.9.

$$\widehat{\Delta R} = \frac{\bar{R}_{RSO}(k) - \bar{R}_{RSO}(k-1)}{\|\bar{R}_{RSO}(k) - \bar{R}_{RSO}(k-1)\|} \tag{5.8}$$

$$\bar{V}_{RSO}(k) = \sqrt{\frac{\mu}{\frac{\bar{R}_{RSO}(k) - \bar{R}_{RSO}(k-1)}{2}}} \cdot \widehat{\Delta R} \tag{5.9}$$

The final method is the Herrick-Gibbs method. For sake of brevity, a thorough discussion of this well-known technique will be left to other authors [24]. Implementation of this technique will be performed through use of Vallado's Herrick-Gibbs algorithm which supplemented his text *Fundamentals of Astrodynamics and Applications* [34]. Comparisons between the three methods will be analyzed to determine how a rough approximation (derivative and circular techniques) compares to Herrick-Gibbs more mathematically rigorous technique.

5.3 Software Implementation of IOD Technique

MATLAB (version 2020b) was used to realize an initial program based off the IOD algorithm that receives a video file and position data for the reflector and generates COEs for the RSO to be tested for accuracy. In order to simplify the program, it is assumed that the reflector and RSO follow two body motion, the reflector and the observational instrument are co-located in a geostationary orbit, and the size of the RSO is negligible compared to the shadow size. First, the program uses the input COEs of the reflector satellite and RSO and a fourth order Runge-Kutta integrator to numerically propagate both orbits for the duration of time specified within the input. The relative position of the position of the RSO with respect to the reflector is then calculated in a similar fashion as discussed before, shown in Equation 5.10.

$$\overline{\mathrm{R}}_{\mathrm{rel}} = \overline{\mathrm{R}}_{\mathrm{RSO}} - \overline{\mathrm{R}}_{\mathrm{illuminator}} \tag{5.10}$$

Next, a binary image of the illumination disk is created to represent an optical instrument aboard the reflector satellite and aligned with the $\hat{e_2}$ and $\hat{e_3}$ axis of the LVLH reference frame. The image is square with 400-km ground distance per side and each pixel represents 100 m. A base image is used to create an illuminated circle, as expressed by Equation 5.11 using a flat-Earth approximation over the picture size.

$$\mathrm{r} = \mathrm{alt}_{\mathrm{geo}} * \tan\left(\frac{\alpha}{2}\right) = 35788.1\mathrm{km} * \tan(.00465) = 166.4\mathrm{km} \tag{5.11}$$

In order to animate the RSO's shadow, the relative position vector is rotated into the LVLH frame via Equation 5.12, where l is the reflector satellites true longitude.

$$[\overline{\mathrm{R}}_{\mathrm{rel}}]^{\mathrm{LVLH}} = \begin{bmatrix} \cos(\pi) & 0 & \sin(\pi) \\ 0 & 1 & 0 \\ -\sin(\pi) & 0 & \cos(\pi) \end{bmatrix} \begin{bmatrix} \cos(\mathrm{l}) & -\sin(\mathrm{l}) & 0 \\ \sin(\mathrm{l}) & \cos(\mathrm{l}) & 0 \\ 0 & 0 & 1 \end{bmatrix} [\overline{\mathrm{R}}_{\mathrm{rel}}]^{\mathrm{IJK}} \tag{5.12}$$

The equation of a three-dimensional half cone centered at the RSO and whose central axis is aligned with the relative position unit vector is then set equal to the plane of the Earth directly under the reflector. The intersection of the three-dimensional plane and cone yields an ellipse along the plane. This plane runs perpendicular to the $\hat{e_1}$ LVLH axis such that when this ellipse is filled in, it represents the objects shadow. This binary image is finally converted into an eight-bit integer value to be saved as a standard .avi video frame; the results of which are shown in below in Figure 43.

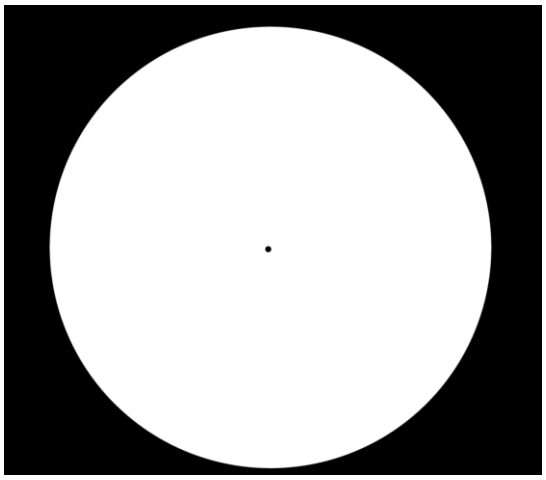

Figure 43. Example Binary Video Frame

For the next frame, a new relative position vector is calculated and the process of re-animating the RSO's shadow is repeated once per frame for the requested duration of the video and upon completion of this loop the video file is saved as well as the position data from the reflector satellite for use in the orbit determination program. For the purposes of initial testing, a frame rate of 30 frames per second was used.

Having read in the video file, the orbit determination program must gather geometric information from the image. For this task, the video frame is sent to a computer

vision subprogram. The image is first converted into a greyscale image. Next, Otsu's thresholding algorithm is then applied to determine a threshold value which is used to convert the greyscale image into binary [35]. This binary image is then flipped, such that any shadows pixels in the image are converted to a one value for detection. All one-valued shapes in the image are then examined for their size parameters. Any shapes that do not fit expected size parameters, in the case of our situation the size of a LEO RSO's shadow, will be filled in. This leaves an image with only the desired shadows present, and this image and the number of objects detected therein are then sent back to the main IOD program. With the video creation software creating a binary image, the computer vision subprogram was tested against a true color image taken by the NASA's Cassini spacecraft. The image (courtesy of NASA's Jet Propulsion Laboratory) shows Io and its shadow overlaid on Jupiter's surface [36]. Figure 44 below provides a visual depiction of the computer vision process on this image.

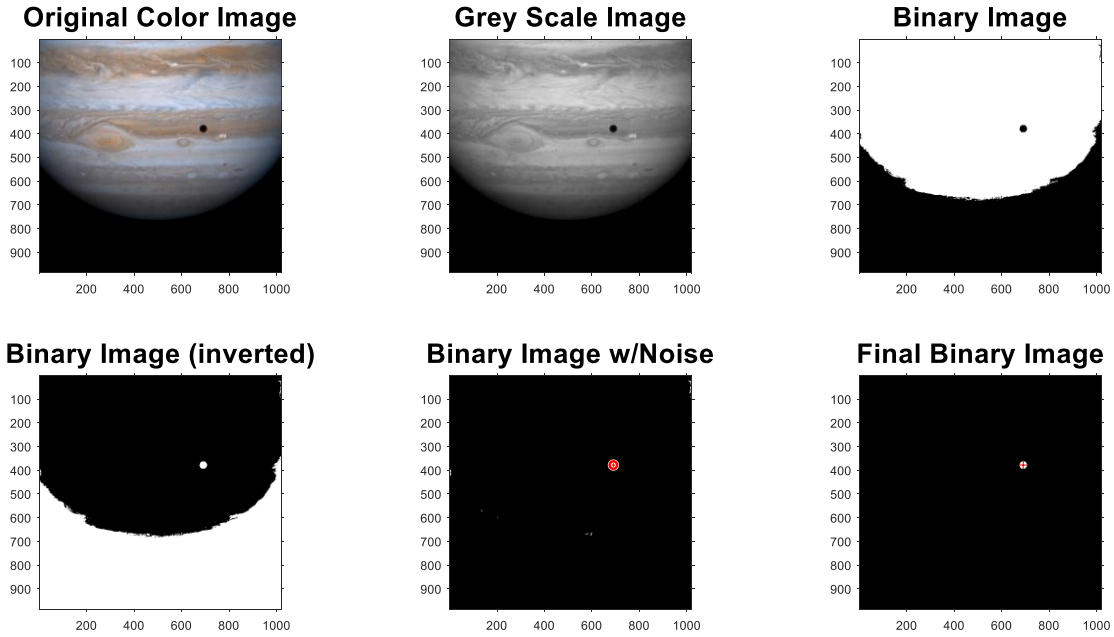

Figure 44. Computer Vision in Action

If the computer vision subprogram does not detect any shadows, then the program continues directly to the next frame. If shadows are detected, then the program measures the shadow's semiminor and semiminor axis lengths, and centroid locations. Using this information, it develops a relative position vector in the LVLH frame as described by Equations 5.1-5.5 previously.

In preliminary testing, significant noise was found in the $\hat{e_1}$ component of the relative position vector in the LVLH frame as shown in Figure 45. This was due to errors in determining the semimajor and semiminor axis lengths. The $\hat{e_2}$ and $\hat{e_3}$ components experienced no such noise, since their values are dominated by the shadow centroid position terms, $C_{\odot}(2)$ and $C_{\odot}(3)$ respectively. In order to negate the effect of the noise on the $\hat{e_1}$ component, a moving mean filter is implemented with a sliding window length equal to the framerate. A moving mean filter averages the input values (*x*) within a finite window (*N*) as shown in Equation 5.13 [37] [38].

$$\mathrm{x(k)} = \frac{\mathrm{x(k)} + \mathrm{x(k-1)} \ldots + \mathrm{x(k-\frac{N}{2})} + \mathrm{x(k+1)} \ldots + \mathrm{x(k+\frac{N}{2})}}{\mathrm{N}} \quad (5.13)$$

As illustrated by Figure 45, the blue line indicating the filtered $\hat{e_1}$ component of the relative position vector in the LVLH frame has far smaller amplitude oscillations than the unfiltered data in red.

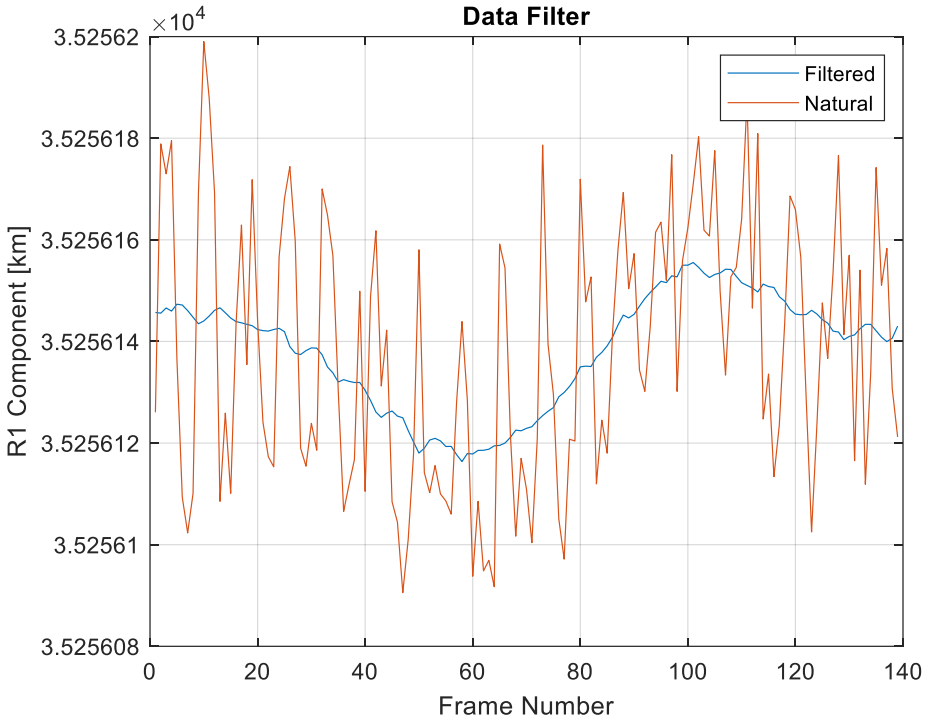

Figure 45. Filtering of $\widehat{e_1}$ Relative Position Vector in the LVLH Frame

Rotations about the second and third axes are then used to convert the relative position vector from the LVLH frame into the IJK frame as shown in Equation 5.14

$$[\bar{R}_{rel}]^{IJK} = \begin{bmatrix} \cos(-l) & -\sin(-l) & 0 \\ \sin(-l) & \cos(-l) & 0 \\ 0 & 0 & 1 \end{bmatrix} \begin{bmatrix} \cos(-\pi) & 0 & \sin(-\pi) \\ 0 & 1 & 0 \\ -\sin(-\pi) & 0 & \cos(-\pi) \end{bmatrix} [\bar{R}_{rel}]^{LVLH} \quad (5.14)$$

This vector is then added to the inertial position vector of the reflector satellite to determine the inertial position vector of the RSO as described by Equation 5.6 previously.

After calculating the inertial position vector as detailed above, inertial velocities can be calculated as described by Equations 5.7 – 5.9 previously. It is of note that the linearized and circularized methods will only yield $n - 1$ full state vectors and the Herrick-

Gibbs method will only yield $n-2$ full state vectors since the methods require initial knowledge of two or three observations respectively.

These inertial position and velocity vectors are then converted into COEs using well known conversion equations [24] [34]. While the position and velocity vectors do provide a fully defined orbit, COEs are chosen as the final output due to five of the six of these elements being constant, namely semimajor axis, eccentricity, inclination, right ascension of the ascending node, and argument of perigee. Using this fact, these five COEs can be averaged throughout the entire simulation duration. The sixth COE, true anomaly will be average through one second or equivalently 30 data points. While not a precision technique, as an example the average true anomaly change of a LEO orbit with an altitude of 50- km over one second is only 0.0634-degrees.

$$\Delta\nu = \frac{360^0}{\mathrm{P}} * 1\,\mathrm{sec} = 0.0634^0 \tag{5.15}$$

These final six COEs are then saved as the output of the IOD program and can then be compared to the inputs to the video creation program for analysis.

VI. Novel Orbit Determination Analysis and Results

6.1 Results

As previously mentioned, testing of this technique assumes the reflector/observer are modeled in a geostationary orbit and in a position coincident with the Vernal Equinox at the epoch time. In order to examine how changing one of the RSO's orbit shape parameters effects the COEs three main trials of 25 tests each were performed, varying the semimajor axis, eccentricity, and inclination. It is important once again to note that this method is deterministic and is being applied to a digital program over a significant course of time and will lend heuristic results. In order for this method to be truly accurate, a more complicated statistical method must be devised.

The semimajor axis was varied from 6878.137-km to 18878.137-km in a circular orbit inclined at 45-degrees. The argument of latitude of the RSO was given as 359.8-degrees and the relative motion simulation was propagated for ten seconds. The results provided are given in terms of the predicted RSO's orbital shape parameters (semimajor axis, eccentricity, and inclination) and the angular position is given in argument of latitude since most of the orbits being tested are circular or near circular and this simplifies the angular position data greatly for initial assessments. The results of these 25 trails are outlined in Figure 46.

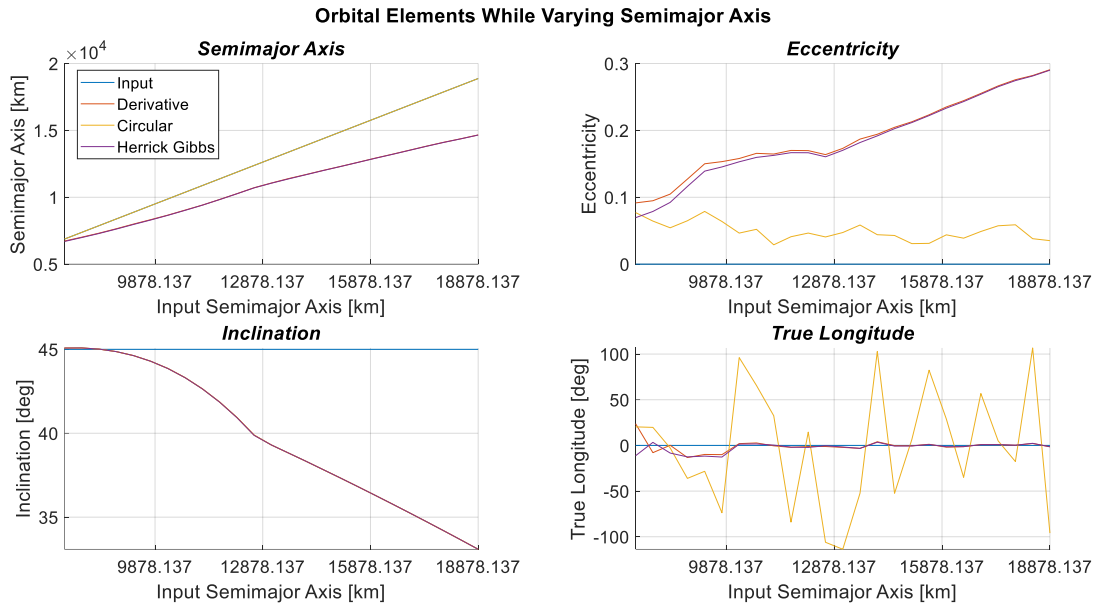

Figure 46. Orbital Elements while Varying Semimajor Axis

Upon visual inspection, it can be seen that as semimajor axis is increased, the circular method closely tracks this increase while the linear and Herrick-Gibbs method diverge from the input. Eccentricity shows a steady divergence for the linear and Herrick-Gibbs method while the circular method holds approximately constant above the zero valued input. All of the inclination values diverge as the semimajor axis is increased. The derivative and Herrick-Gibbs methods are quite accurate for the initial true longitude value, while the circular approximation had much larger oscillations about the true input value. The input orbit is circular, so it should come as no surprise that the circular assumption most closely tracks the increasing semimajor axis. The increasing errors in eccentricity for the linear and Herrick-Gibbs methods, as well as inclination for all methods may be attributable to the different rates of relative motion. Lower orbits will cover more relative distance than higher ones within the same 10 second pass, resulting in a greater spread in

data points. This variance seems to be necessary to accurately determine the orbital elements. In order to gain a visual sense of these orbits, the input of run number 15 (in blue, altitude of 7,500-km), and the linear (yellow), circular (green), and Herrick-Gibbs (red) approximations are shown in Systems Tool Kit (STK) in Figure 47.

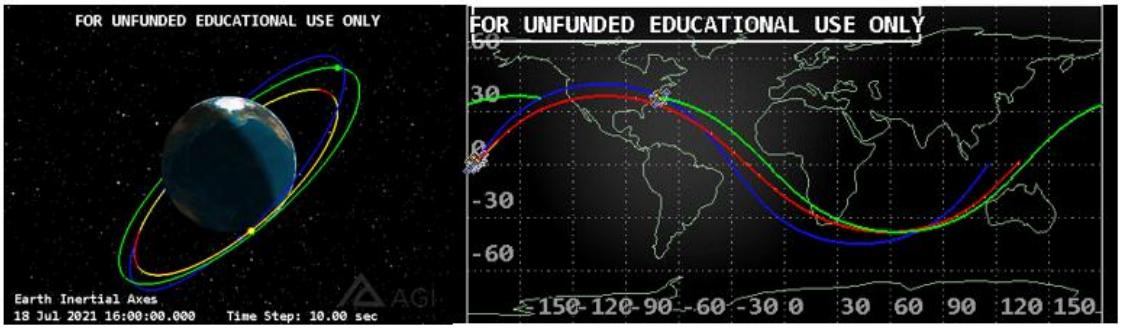

Figure 47. Trial One Example Three- and Two-Dimensional of Output

The eccentricity was varied from 0.0000001 to 0.1 in an orbit with a semimajor axis of 11378.137-km, an inclination of 45-degrees, right ascension of 0, argument of perigee of 0, and a true anomaly of 359.8-degrees. The results of these 25 trails are given in Figure 48.

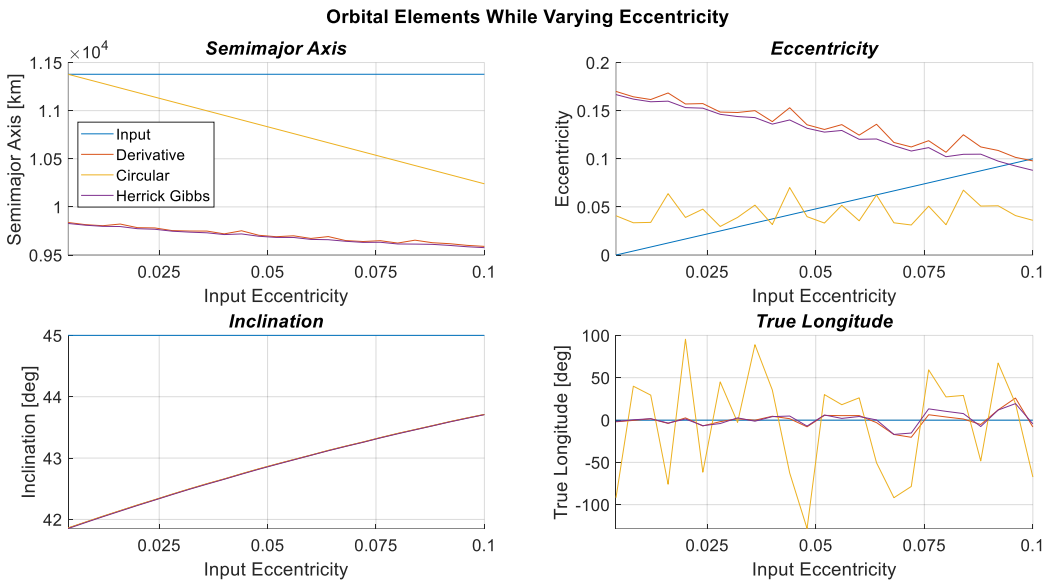

Figure 48. Orbital Elements while Varying Eccentricity

As expected, Figure 48 shows that as the eccentricity increases, the circular assumption diverges quickly from the input semimajor axis while the linear and Herrick-Gibbs methods both maintain an underestimate value. It is also expected that the circular assumption maintains an approximately constant value for eccentricity as is observed. The linear and Herrick-Gibbs methods both provide an overestimate of eccentricity but do converge to the input value at higher values of eccentricity. For near circular orbits ($e < 0.1$) however it seems that the circular approximation provides a good baseline. The error of the inclination value decreases as the eccentricity is increased. Once again, the linear and Herrick-Gibbs approximations tend to have a significantly smaller error in true longitude than the circular approximation.

The underestimation in the RSO's semimajor axis is likely due to the spacecraft's short arc being observed at perigee, and that if it were instead observed at apogee, it would show

an overestimate value. This is the main difficulty of developing short arc techniques; it is difficult to make predictions about where the RSO will be half a period later based on a short pass. This could also explain the inclination error decreasing as the eccentricity is increased. At apogee, the RSO will be moving faster providing creating a greater spread in data points for analyzes as discussed previously. Short arc stochastic methods could prove integral to the further development of this technique to resolve this issue.

In order to gain a visual sense of these orbits, the input of run number 15 (in blue, eccentricity of 0.0583), and the linear (yellow), circular (green), and Herrick-Gibbs (red) approximations are depicted in Figure 49.

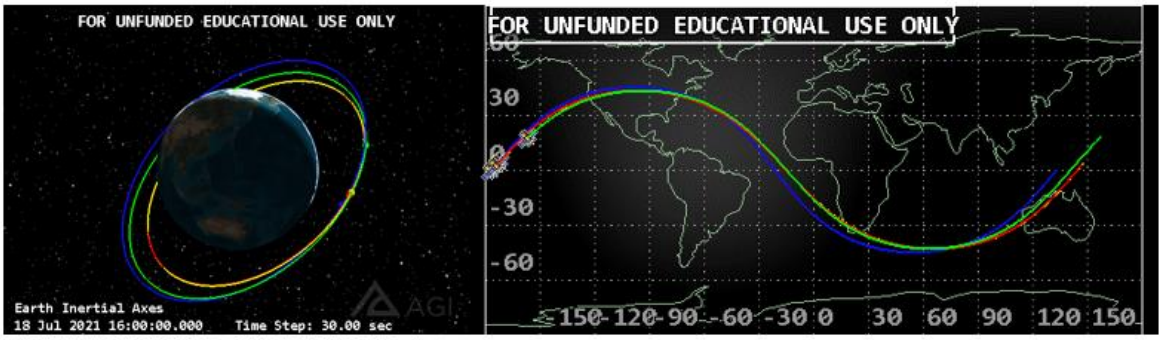

Figure 49. Trial Two Example Three- and Two-Dimensional Output

Lastly, the inclination was varied from 0 to 180-degrees in a circular orbit with a semimajor axis of 11,378.137-km and a true longitude of 359.8-degrees. The results of these 25 trails are given in Figure 50.

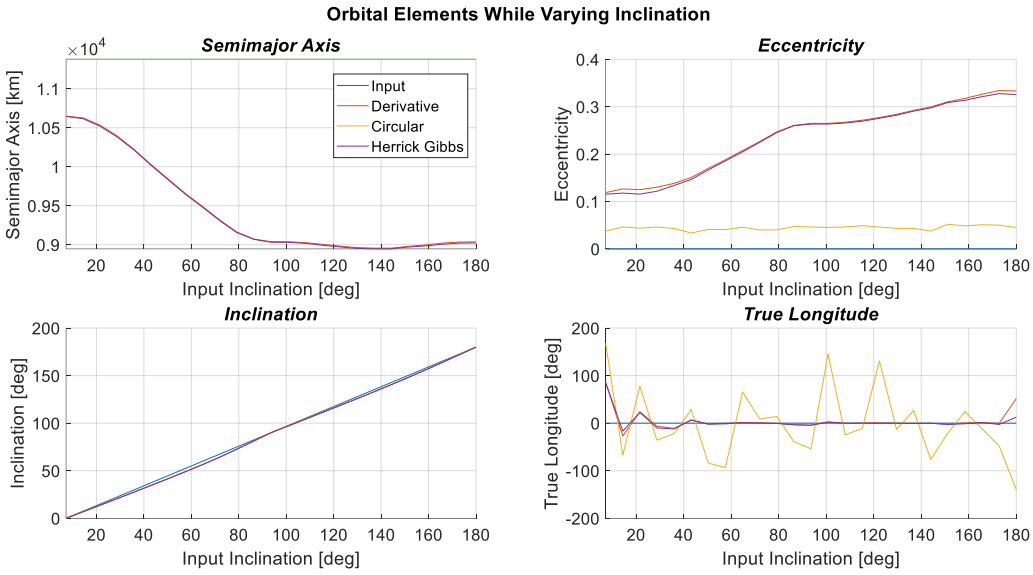

Figure 50. Orbital Elements while Varying Inclination

Due to the orbit being circular, we once again find that the circular approximation closely matches the semimajor axis, while the linear and Herrick-Gibbs methods provide a diverging underestimate. Similarly, we find a nearly identical plot of the eccentricity as when varying the semimajor axis, with the circular approximation providing a near constant value and the linear and Herrick-Gibbs methods diverging. The inclination plot shows constant accurate tracking. The true longitude again shows the linear and Herrick-Gibbs methods providing a far closer approximation in the majority of cases. In order to gain a visual sense of these orbits, the input of run number 15 (in blue, inclination of 105-degrees), and the linear (yellow), circular (green), and Herrick-Gibbs (red) approximations are shown below in Figure 51.

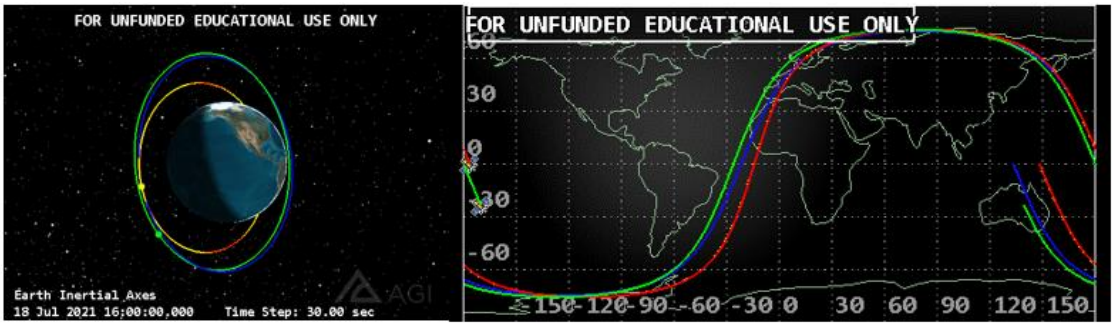

Figure 51. Trial Three Example Three- and Two-Dimensional Output

6.2 Discussion

This testing has shown some important heuristic results. It is clear from Figs. 10, 12, and 14 that the most difficult shape parameters to be calculated are the semimajor axis and eccentricity. In testing, eccentricity has proven to be the most difficult to model for low Earth orbits where low values for eccentricity are common. The circular approximation repeatedly provides the most accurate overall orbit shape, however the linear and Herrick-Gibbs methods tend to provide significantly better initial position estimates. These preliminary data points yield confidence that a short arc statistical method can be created that provides results with significantly higher accuracy.

One of the benefits of this method is a large search area to locate an uncooperative RSO. Assuming a geostationary reflector, the radius of the search area for an RSO at 500-km in LEO would be nearly 330-km in diameter. For an uncooperative or tumbling RSO, it can be very difficult to effectively locate it due to changing or masked radar cross sections. Optical observations also require a significant amount of environmental cooperation. There are many ways in which a radar or optical observations can be

disrupted, however it is far more difficult for a shadow to be masked. With the growing number of RSOs these benefits avail further development of this method.

In order to increase the efficacy of this IOD technique several further developments are being pursued. First and foremost, a statistical technique must be implemented to utilize the full range of information provided from the dense observation data collected from a pass. Once accomplished, the testing code should be altered to consider various spacecraft cross sectional areas as well as a non-co-located observer and reflector. Upon completion of these updates, the orbits discussed above should be tested. Assuming acceptable results, the technique could then be tested against one of the many LEO catalogs to determine accuracy over a wider range of real-world orbital parameters.

6.3 Summary

This chapter has described the initial progress towards the development of a novel IOD technique based on the transit of a RSO in front of an artificial point light source. This deterministic method melds advances made in the field of astronomy, such as short arc orbit determination and occlusion analysis, with LEO space situational awareness methods. This deterministic method should provide inertial position data accurately to within the precision of available optical instruments. This inertial position data can then be used to create a velocity vector to fully define the translational system.

There are many methods of calculating a velocity vector from the inertial position vector. Three techniques were tested, a linear approximation, a circular approximation, and the Herrick-Gibbs method. In further development of a statistical model, the circular approximation may prove useful for near-circular orbits, while the Herrick-Gibbs

technique could yield a better initial estimate over a wider range of orbital eccentricities. Ultimately, this method could prove beneficial in the updating the catalogs containing the ever-increasing number of RSOs in the LEO domain. Should development of space-based solar reflectors continue, this novel method could prove useful in preliminary orbit determination for both cooperative and uncooperative RSOs.

VII. Conclusions and Recommendations

7.1 Conclusions of Research

This research has shed a modern light on the uses of space-based solar reflectors. This avant-garde approach has yielded several significant results. A reflector system has been designed that can drastically increase available illumination on orbit. A proximity operations maneuver was developed that allows for an inspection of all sides of a target with direct illumination in under one period using no fuel (other than required to combat perturbing effects). Proximity operations could benefit substantially by equipping the inspector with a simple flat-plane membrane mirror. Reflectors such as these increase the quantity of inspection time under ideal illumination conditions by approximately 95% in GEO and 60% in LEO. This technique could provide a simple, a low mass, and low-cost method of augmenting on-orbit lighting conditions. This research could lower the complexity of rendezvous and proximity operation mission concepts and could be of particular benefit in uncooperative spacecraft inspection and servicing. This technique could facilitate CubeSats in completing rendezvous and proximity that have historically been performed by larger spacecraft.

A new method of orbit determination has also been detailed. Though the technique still requires extensive development, it shows promise for future improvement. Advancements in short arc high data density techniques as are used in asteroid orbit determination can be leveraged to further refine this technique. Experiments such as the Air Force Research Laboratory's Space Solar Power Incremental and Demonstrations Research (SSPIDR) program could provide the space-based illumination source required

for this technique [39]. While this research was certainly specialized, it provided an opportunity to get hands on experience with the optics, physics, and programing skills that the primary research objectives required.

7.2 Significance of Research

This research has been a unique application of old ideas to create novel solutions to contemporary problems. The interdisciplinary nature of this body of work has garnered considerable attention from the greater aerospace and academic community.

- Research Funding: The Edison Grant generously awarded $20,000 in funding to explore this research.
    - Edison Grant: "Investigation of Mirror Satellite Concept to Provide Augmented Lighting for Dim Space-Based Objects," 2021, $20,000.
- Patents: The novel IOD method was awarded a provisional patent.
    - Dombrowski, D. M., Bettinger, R. A., "Spacecraft Orbit Determination System," AFD-2224, U.S. Provisional Patent No. 17/467,548, September 2021.
- Conference Paper Accepted on Basis of Full Paper Review: A conference paper pertaining to the development of reflector constellations and proximity maneuvers has been accepted for review and presentation at the 2022 IEEE Aerospace Conference.
    - Dombrowski, D. M., Bettinger, R. A., "Investigation of Mirror Satellite Concept to Provide Augmented Lighting for Dim Space-Based Objects," 2022 IEEE Aerospace Conference, Big Sky, MT, March 2022.

- Conference Paper Accepted on Basis of Abstract Review: A conference paper pertaining to the development of the IOD technique was written for the 2021 Advanced Maui Optical and Space Surveillance Technologies Conference (AMOS).
    - Dombrowski, D. M., Bettinger R. A., "Preliminary Orbit Determination Using the Transit of Satellites in Front of Space-Based Illumination Sources," 2021 Advanced Maui Optical and Space Surveillance Technologies Conference (AMOS), Maui, HI, September 2021.
- Scholarly Presentations: The IOD method was presented at AMOS, the 46th AIAA Dayton-Cincinnati Aerospace Sciences Symposium (DCASS), and the 14th AAS Wernher von Braun Memorial Symposium, Huntsville.
    - Dombrowski, D. M., Bettinger, R. A., "Preliminary Orbit Determination Using the Transit of Satellites in Front of Space-Based Illumination Sources," 46th AIAA Dayton-Cincinnati Aerospace Sciences Symposium (DCASS), Dayton, OH, March 2021.
    - Dombrowski, D. M., Bettinger, R. A., "Preliminary Orbit Determination Using the Transit of Satellites in Front of Space-Based Illumination Sources," 14th AAS Wernher von Braun Memorial Symposium, Huntsville, AL, October 2021.

7.3 Recommendations for Future Research

The following section provides avenues for further development in both the primary and secondary research topics, ranging from short term to long term developments:

Short-Term Recommendations

Primary Research

- Physical Property Verification: Aluminum, silver, and gold Kapton mirrors have been purchased to verify the commercial sector's ability to provide the reflectivity and surface figure estimates provided by NASA.
- MOI Estimation: Create MOI estimates for large reflectors that include required apparatus to maintain surface figure.

Secondary Research

- Statistical Filtering: Develop short-arc high data density statistical filtering technique to account for noise in shadow parameter measurements.

Long Term Recommendations

Primary Research

- Reflector Stowage and Deployment: Develop an optimized folding pattern and accompanying deployment technique for large membrane mirrors.
- Hardware in the Loop Testing: Simulate physical NMC results by testing augmented lighting proximity operations scenario with AFIT's CASpR testbed.
- Cislunar Applications: The Cislunar regime poses specific challenges to the SDA mission. Reflector aided proximity operations should be evaluated for applicability within this regime.
- Environmental Testing: Membrane mirrors should be tested to determine robustness to the space environment. Of particular interest is an examination of the effects of micrometeoroid impacts on mirror reflectivity parameters.

Secondary Research

- Solar Eclipse Testing: Gather images and accurate ephemeris from NASA's Hubble and Cassini missions in order to apply and test the IOD algorithm to Jupiter's Galilean moons.
- High Fidelity Earth Simulation: Create an improved video model of the Earth to include albedo, Rayleigh scattering, and other distortive effects over a wide wavelength spectrum.

Appendix A: Results with Collimating Sun Synchronous Mirrors

Run #	Orbit	Significance	Chief	Deputy
1	LEO (July 29 2021)	ISS type	$R = [6{,}798.137 \quad 0 \quad 0]^T$ $V = [0 \quad 4.7519 \quad 6.0045]^T$	$\rho = [5 \quad 0 \quad 5]^T$ $\dot{\rho} = [0 \quad -2nx_0 \quad -nx_0]^T$
2	LEO (July 29 2021)	ISS type	$R = [6{,}798.137 \quad 0 \quad 0]^T$ $V = [0 \quad 4.7519 \quad 6.0045]^T$	$\rho = [5 \quad 0 \quad 5]^T$ $\dot{\rho} = [0 \quad -2nx_0 \quad -2nx_0]^T$
3	LEO (July 29 2021)	Exclusion zone	$R = [6{,}841.637 \quad 0 \quad 0]^T$ $V = [0 \quad 7.6329 \quad 0]^T$	$\rho = [5 \quad 0 \quad 5]^T$ $\dot{\rho} = [0 \quad -2nx_0 \quad -nx_0]^T$
4	GEO (July 29 2021)	No Eclipse	$R = [42{,}166.2370 \quad 0 \quad 0]^T$ $V = [0 \quad 3.0746 \quad 0]^T$	$\rho = [5 \quad 0 \quad 5]^T$ $\dot{\rho} = [0 \quad -2nx_0 \quad -nx_0]^T$
5	GEO (March 20 2021)	Eclipse	$R = [42{,}166.2370 \quad 0 \quad 0]^T$ $V = [0 \quad 3.0746 \quad 0]^T$	$\rho = [5 \quad 0 \quad 5]^T$ $\dot{\rho} = [0 \quad -2nx_0 \quad -nx_0]^T$

Illumination Paths	Collimated	Name
Direct Sunlight on Target	No	Sunlight
Sunlight-Inspector-Target	No	Inspector
Sunlight-Solar-Reflector-Target	Yes	Reflector1 (or 2)
Sunlight- Solar Reflector-Inspector-Target	Yes	Bounce1 (or 2)

Run 1:

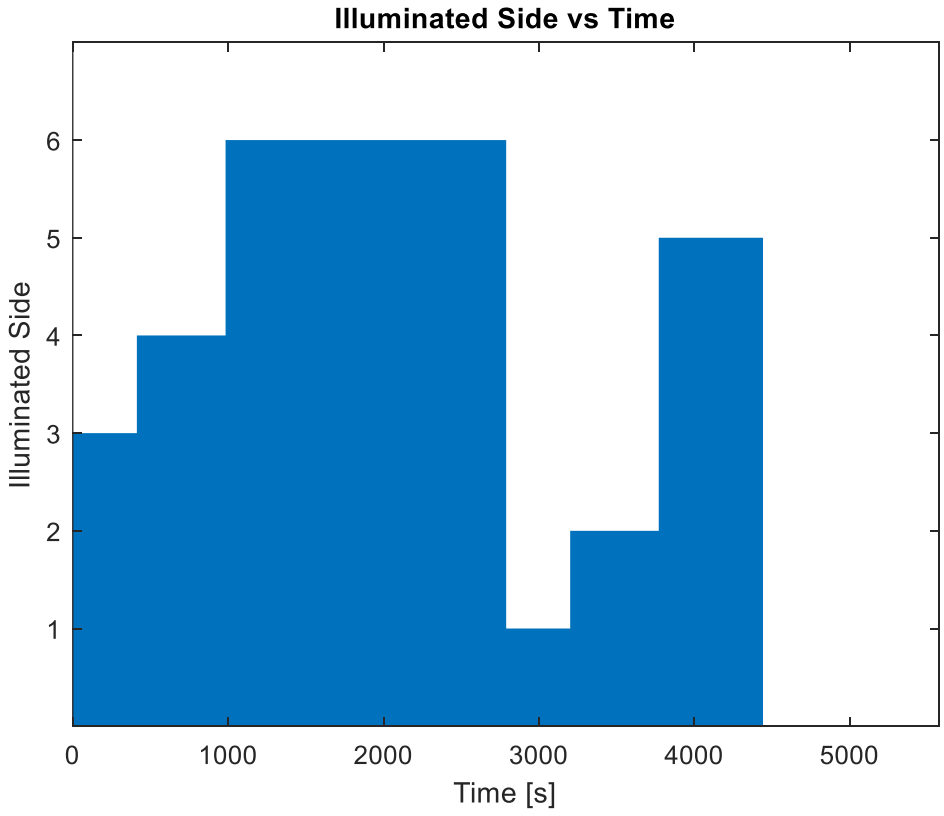

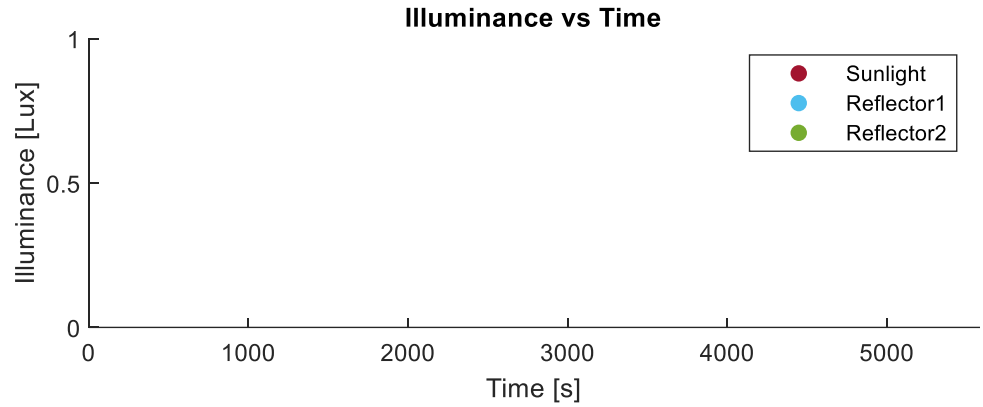
Illuminance vs Time
Illuminance [Lux]
Time [s]
Sunlight
Reflector1
Reflector2
0
0.5
1
0
1000
2000
3000
4000
5000

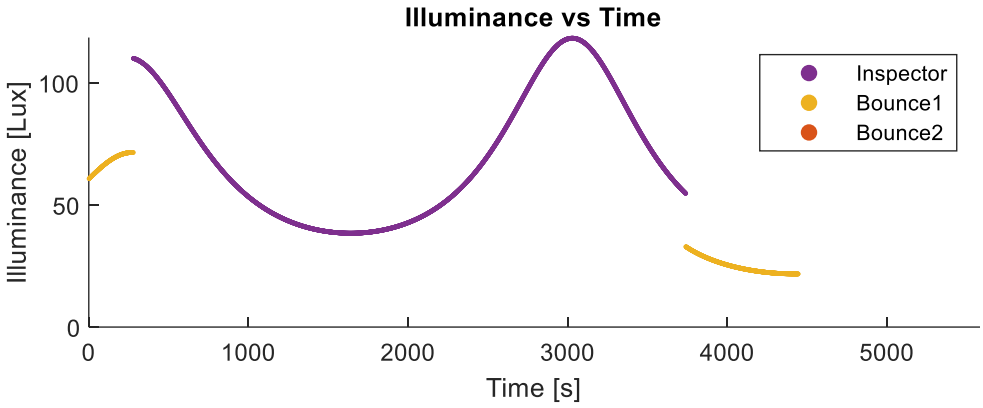
Illuminance vs Time
Illuminance [Lux]
Time [s]
Inspector
Bounce1
Bounce2
0
50
100
0
1000
2000
3000
4000
5000

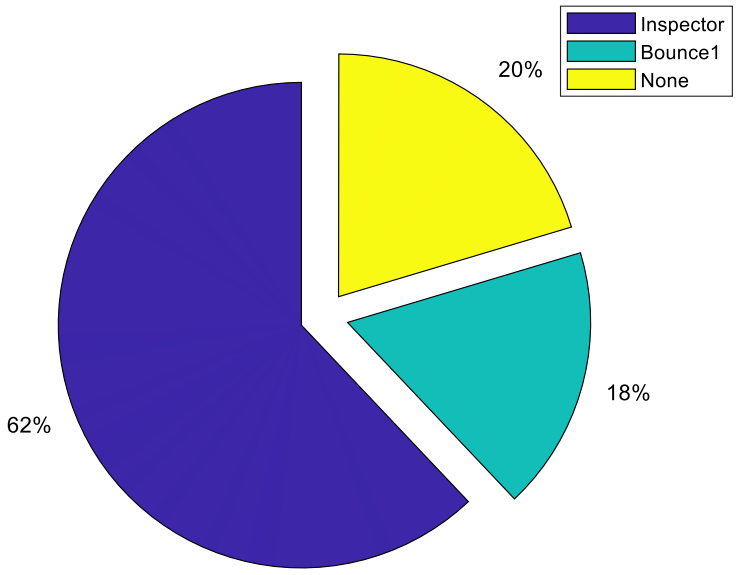
Inspector
Bounce1
None
20%
18%
62%

Run 2:

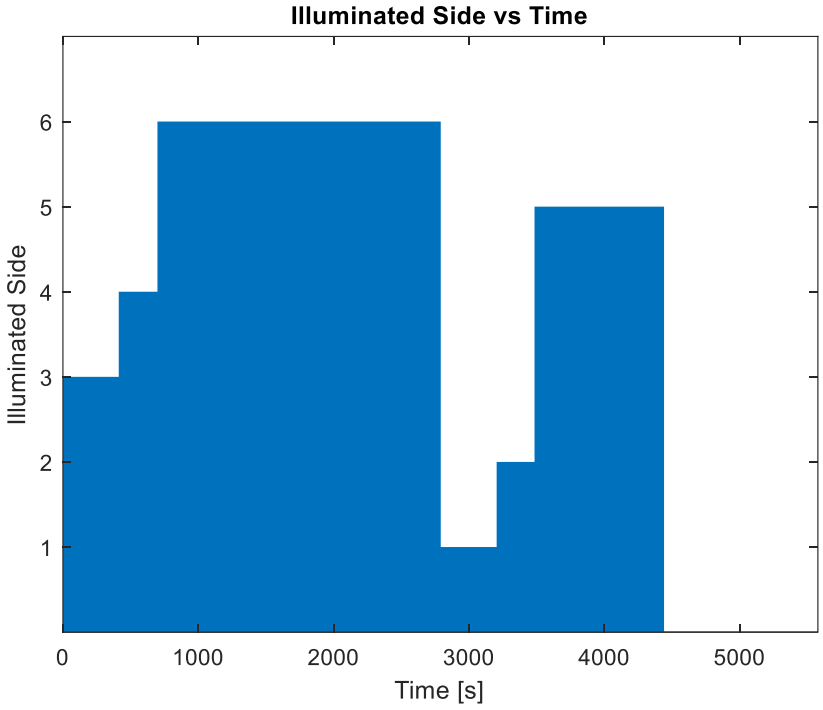
Illuminated Side vs Time
Illuminated Side
Time [s]
0
1000
2000
3000
4000
5000
1
2
3
4
5
6

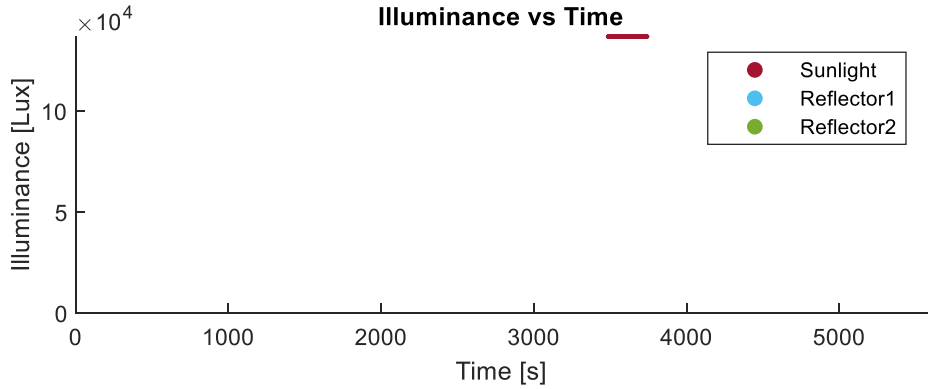
Illuminance vs Time
×10^4
Illuminance [Lux]
Time [s]
Sunlight
Reflector1
Reflector2
0
5
10
0
1000
2000
3000
4000
5000

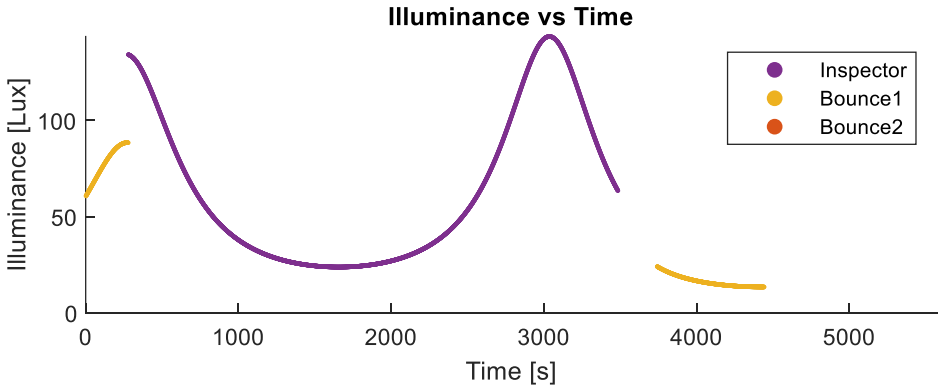
Illuminance vs Time
Illuminance [Lux]
Time [s]
Inspector
Bounce1
Bounce2
0
50
100
0
1000
2000
3000
4000
5000

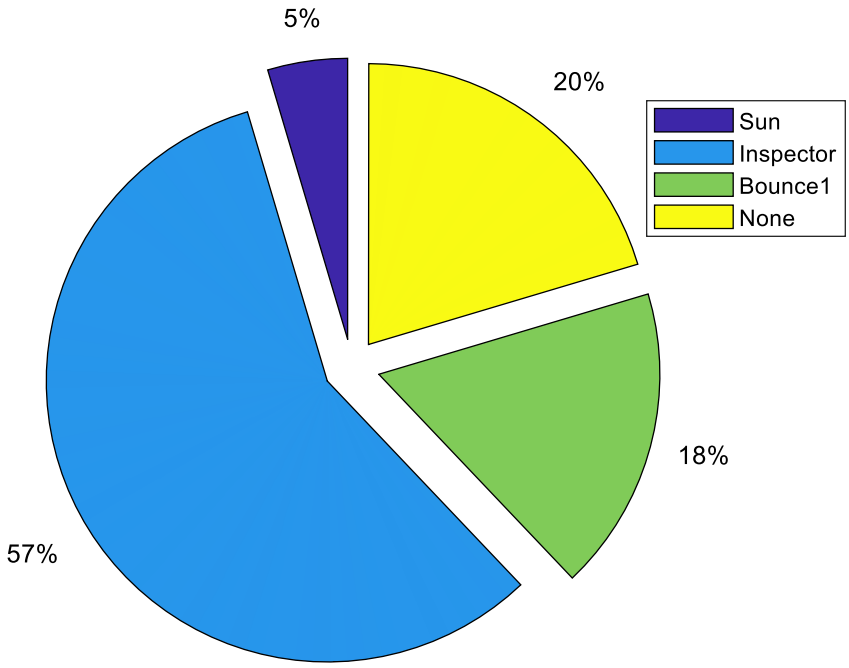
5%
20%
18%
57%
Sun
Inspector
Bounce1
None

Run 3:

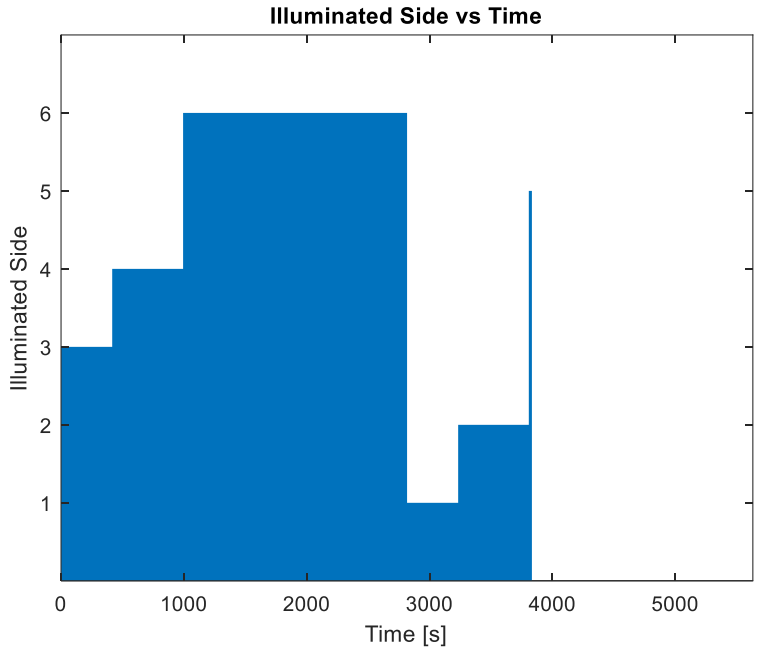
Illuminated Side vs Time
Illuminated Side
Time [s]
0
1000
2000
3000
4000
5000
1
2
3
4
5
6

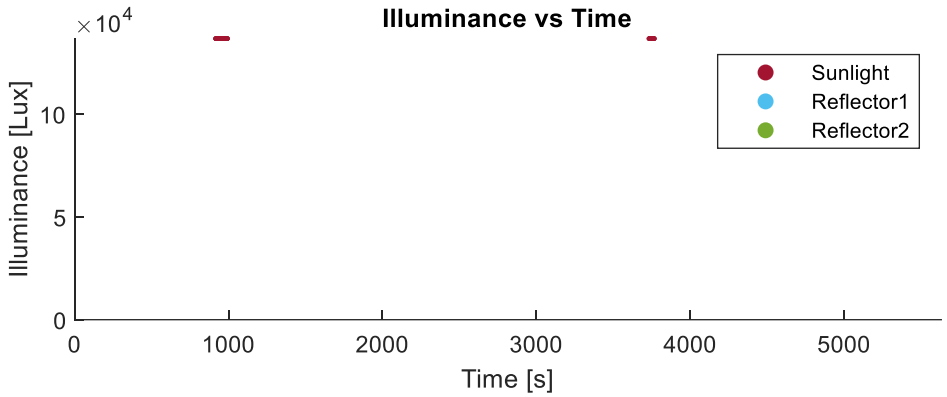
Illuminance vs Time
×10^4
Illuminance [Lux]
Time [s]
Sunlight
Reflector1
Reflector2
0
5
10
0
1000
2000
3000
4000
5000

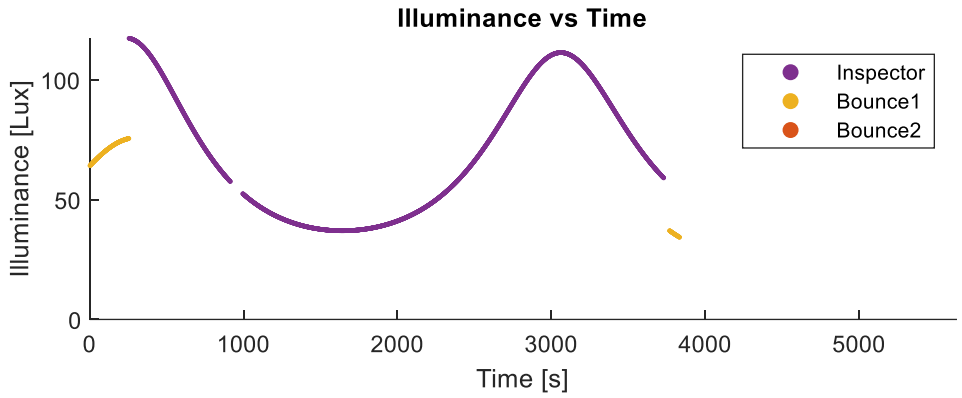
Illuminance vs Time
Illuminance [Lux]
Time [s]
Inspector
Bounce1
Bounce2
0
50
100
0
1000
2000
3000
4000
5000

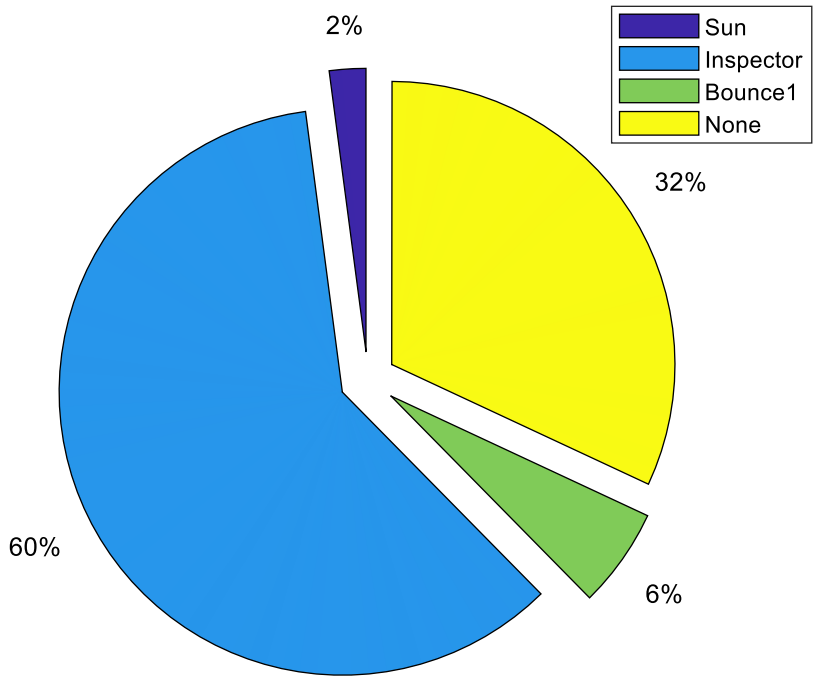
2%
32%
60%
6%
Sun
Inspector
Bounce1
None

Run 4:

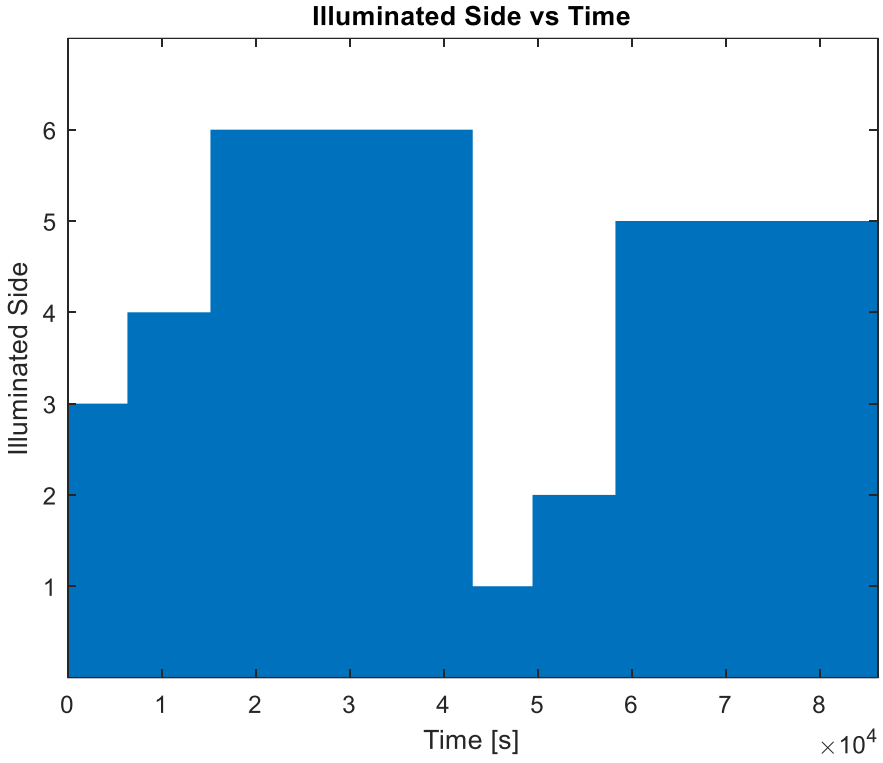
Illuminated Side vs Time
Illuminated Side
Time [s]
×10^4

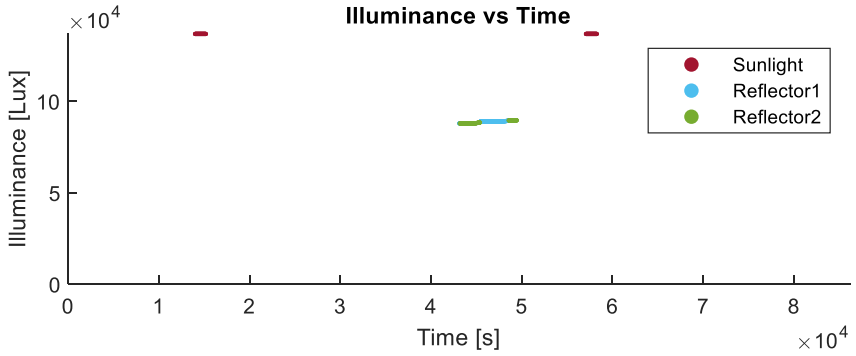
Illuminance vs Time
Illuminance [Lux]
Time [s]
×10^4
Sunlight
Reflector1
Reflector2

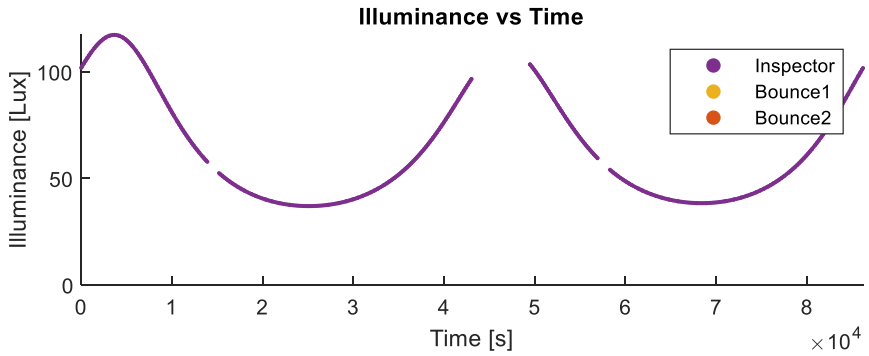
Illuminance vs Time
Illuminance [Lux]
Time [s]
×10^4
Inspector
Bounce1
Bounce2

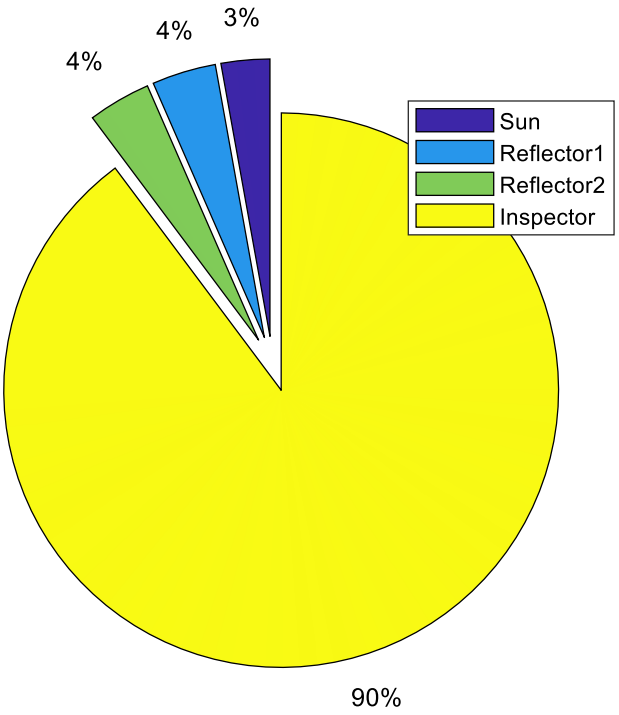
3%
4%
4%
90%
Sun
Reflector1
Reflector2
Inspector

Run 5:

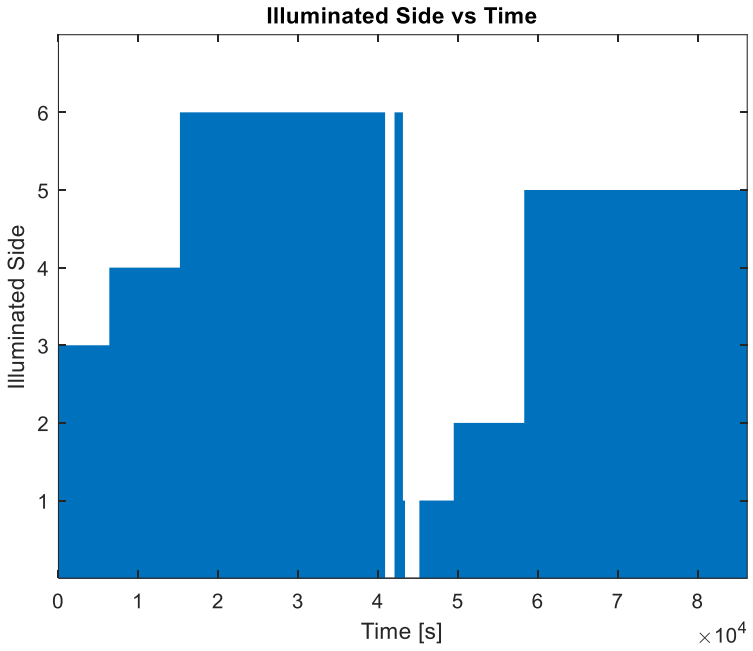
Illuminated Side vs Time
Illuminated Side
Time [s]
×10^4

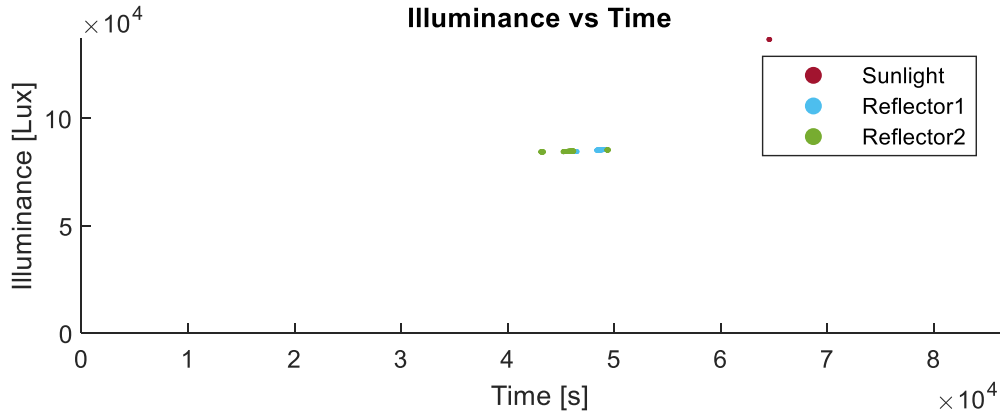
Illuminance vs Time
Illuminance [Lux]
Time [s]
×10^4
Sunlight
Reflector1
Reflector2

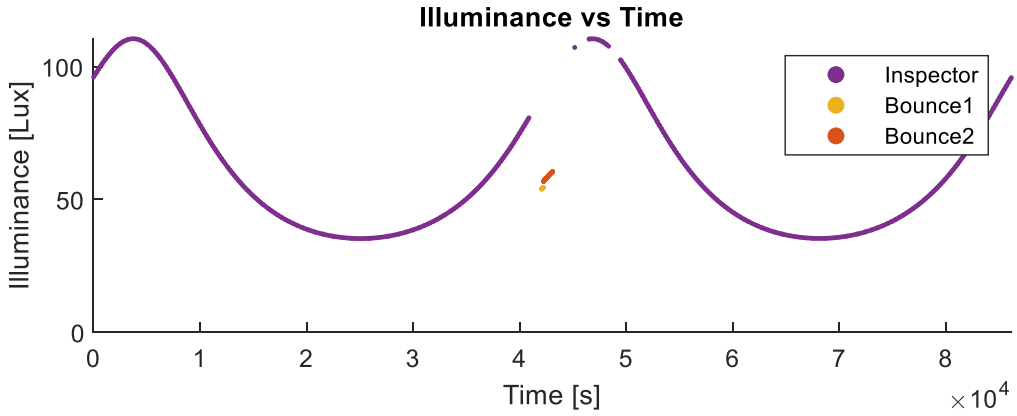
Illuminance vs Time
Illuminance [Lux]
Time [s]
×10^4
Inspector
Bounce1
Bounce2

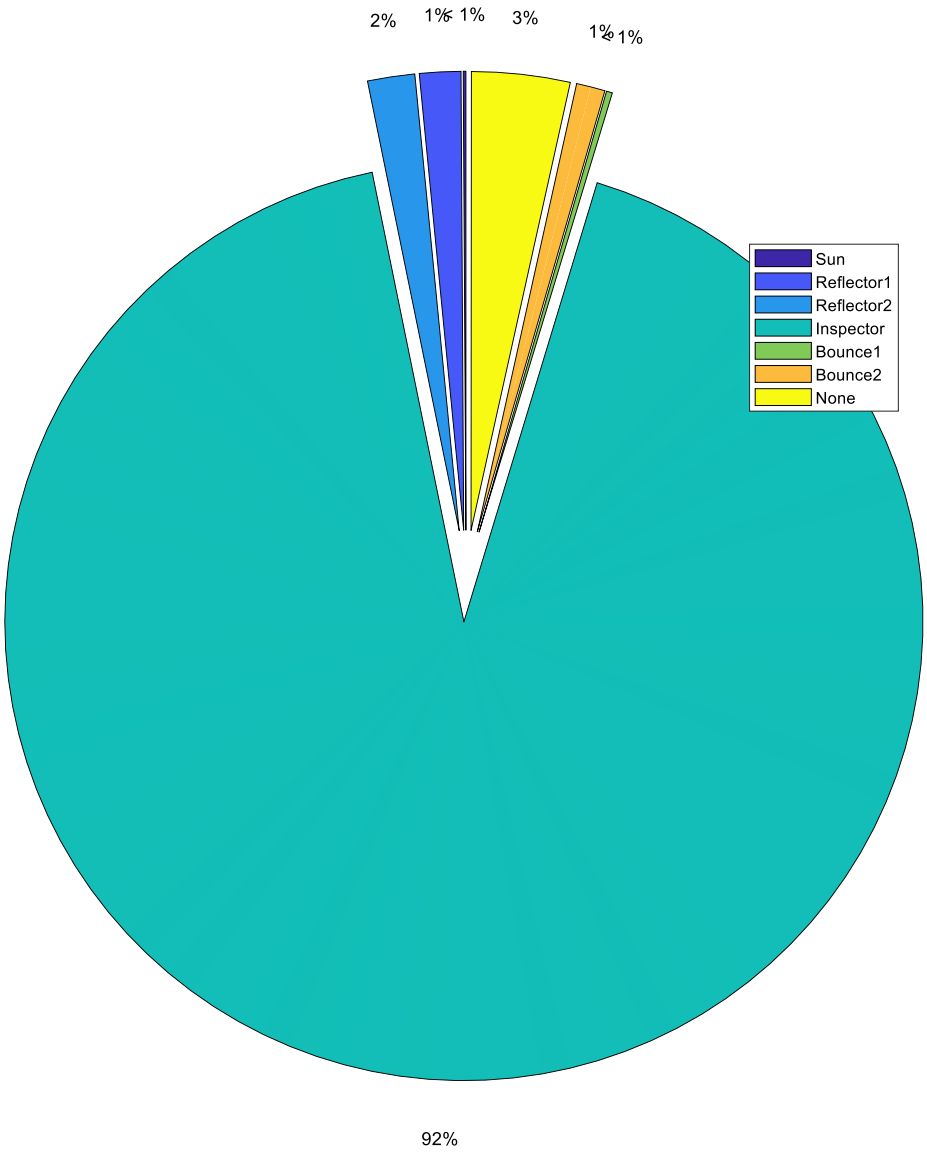
2%
1%
1%
3%
1%
1%
Sun
Reflector1
Reflector2
Inspector
Bounce1
Bounce2
None
92%

Appendix B: Results with Non-Collimating Sun Synchronous Mirrors

Run #	Orbit	Significance	Chief	Deputy
1	LEO (July 29 2021)	ISS type	$R = [6{,}798.137 \quad 0 \quad 0]^T$ $V = [0 \quad 4.7519 \quad 6.0045]^T$	$\rho = [5 \quad 0 \quad 5]^T$ $\dot{\rho} = [0 \quad -2nx_0 \quad -nx_0]^T$
2	LEO (July 29 2021)	ISS type	$R = [6{,}798.137 \quad 0 \quad 0]^T$ $V = [0 \quad 4.7519 \quad 6.0045]^T$	$\rho = [5 \quad 0 \quad 5]^T$ $\dot{\rho} = [0 \quad -2nx_0 \quad -2nx_0]^T$
3	LEO (July 29 2021)	Exclusion zone	$R = [6{,}841.637 \quad 0 \quad 0]^T$ $V = [0 \quad 7.6329 \quad 0]^T$	$\rho = [5 \quad 0 \quad 5]^T$ $\dot{\rho} = [0 \quad -2nx_0 \quad -nx_0]^T$
4	GEO (July 29 2021)	No Eclipse	$R = [42{,}166.2370 \quad 0 \quad 0]^T$ $V = [0 \quad 3.0746 \quad 0]^T$	$\rho = [5 \quad 0 \quad 5]^T$ $\dot{\rho} = [0 \quad -2nx_0 \quad -nx_0]^T$
5	GEO (March 20 2021)	Eclipse	$R = [42{,}166.2370 \quad 0 \quad 0]^T$ $V = [0 \quad 3.0746 \quad 0]^T$	$\rho = [5 \quad 0 \quad 5]^T$ $\dot{\rho} = [0 \quad -2nx_0 \quad -nx_0]^T$

Illumination Paths	Collimated	Name
Direct Sunlight on Target	No	Sunlight
Sunlight-Inspector-Target	No	Inspector
Sunlight-Solar-Reflector-Target	No	Reflector1 (or 2)
Sunlight- Solar Reflector-Inspector-Target	No	Bounce1 (or 2)

Trial 1:

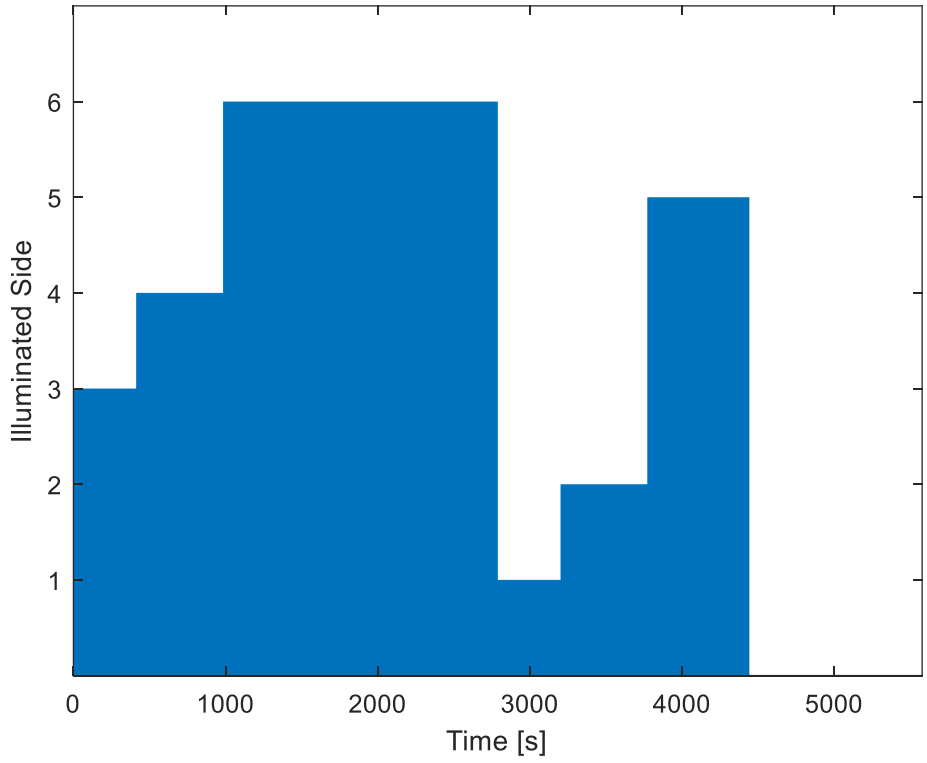

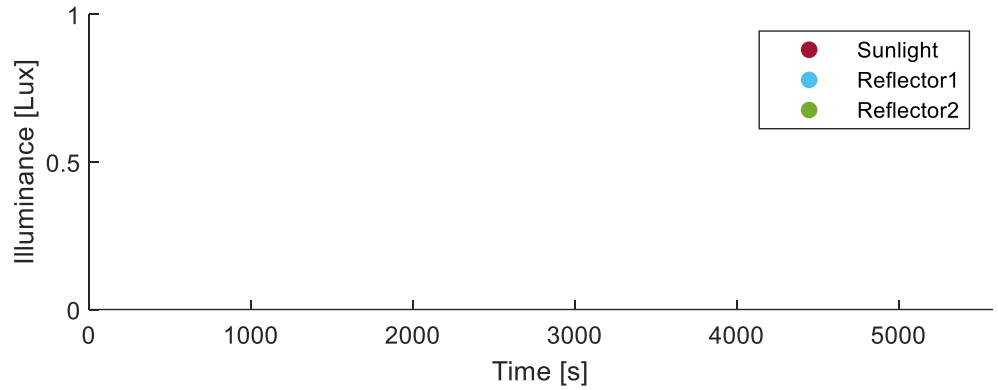
Illuminance [Lux]
1
0.5
0
0
1000
2000
3000
4000
5000
Time [s]
Sunlight
Reflector1
Reflector2

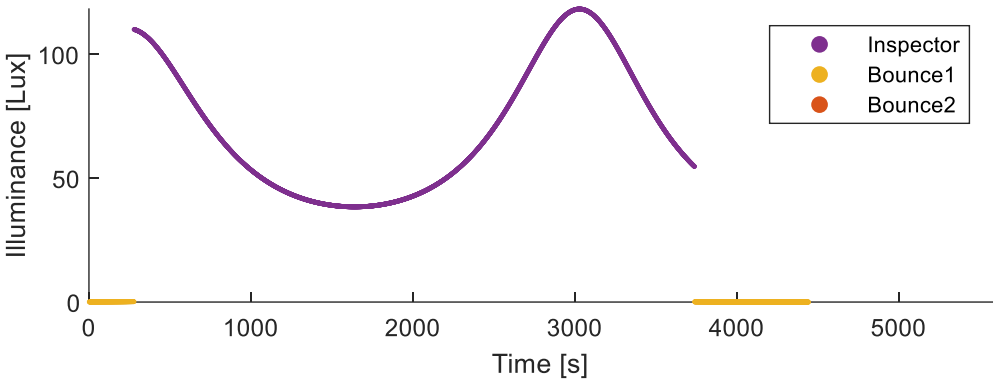
Illuminance [Lux]
100
50
0
0
1000
2000
3000
4000
5000
Time [s]
Inspector
Bounce1
Bounce2

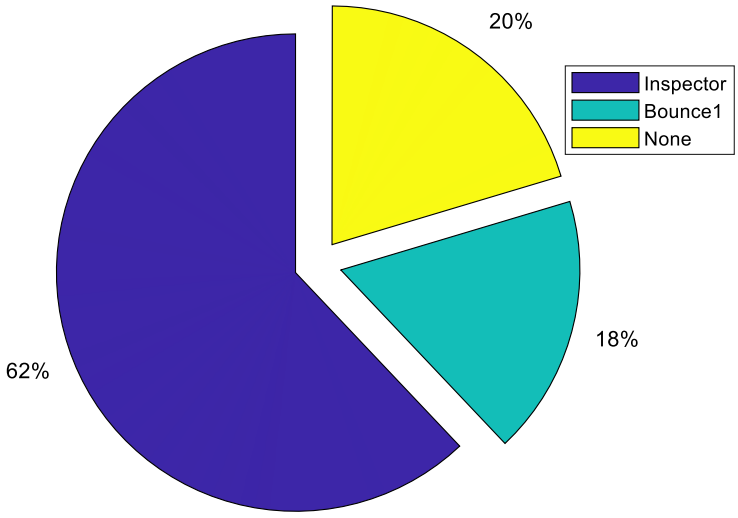
20%
18%
62%
Inspector
Bounce1
None

Trial 2:

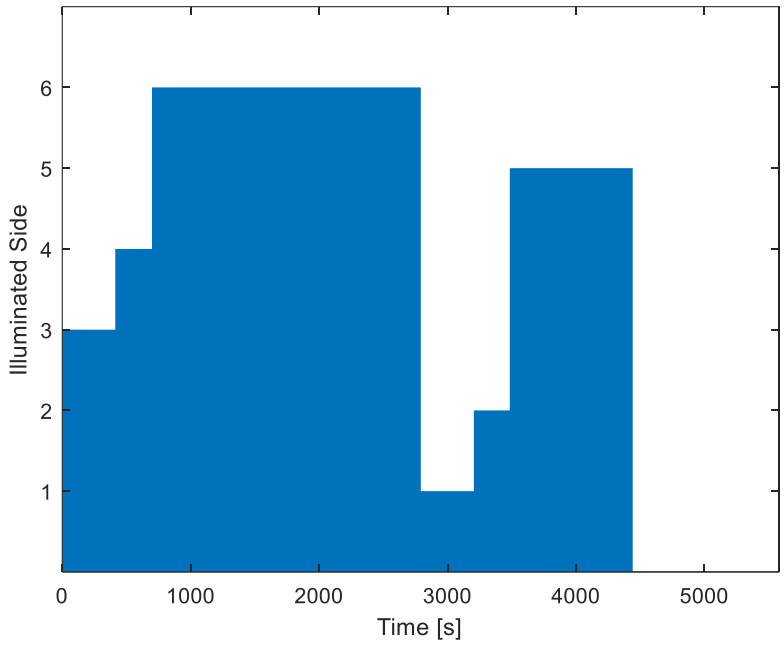
Illuminated Side
Time [s]
0
1000
2000
3000
4000
5000
1
2
3
4
5
6

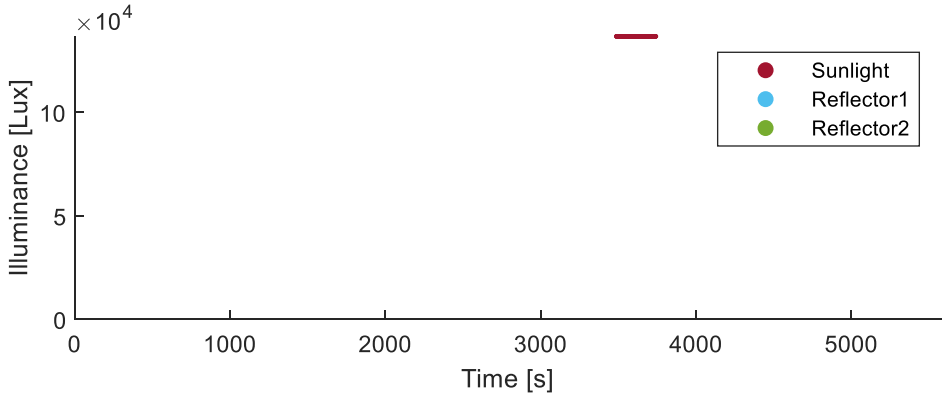
×10^4
Illuminance [Lux]
Time [s]
Sunlight
Reflector1
Reflector2
0
5
10

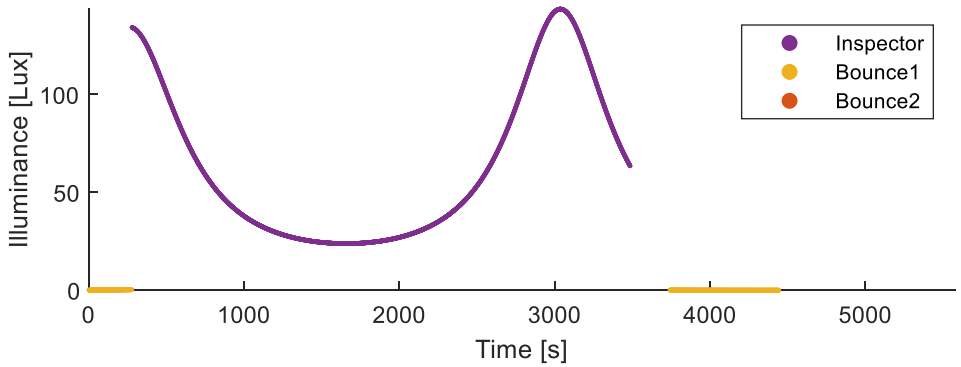
Illuminance [Lux]
Time [s]
Inspector
Bounce1
Bounce2
0
50
100

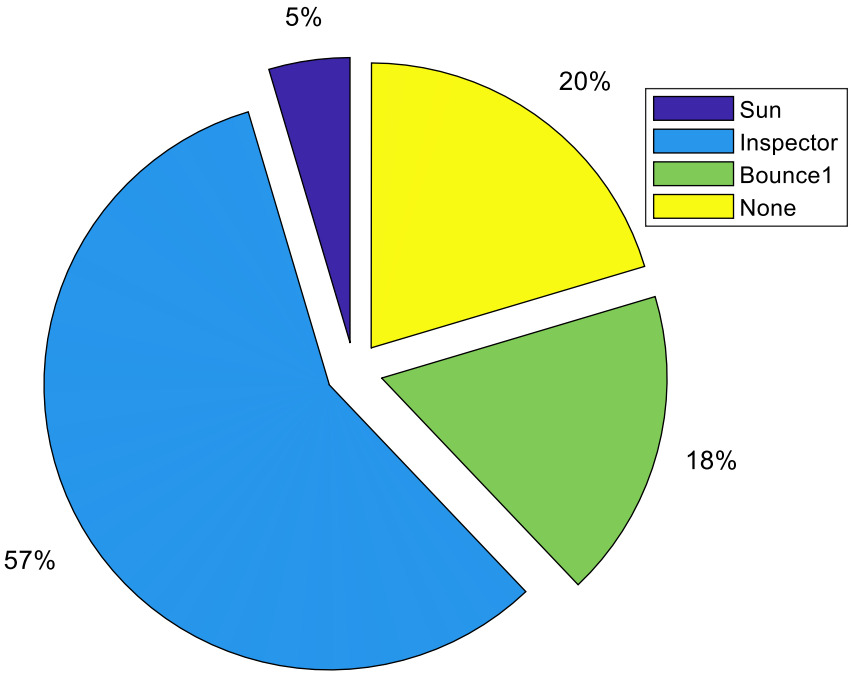
5%
20%
18%
57%
Sun
Inspector
Bounce1
None

Trial 3:

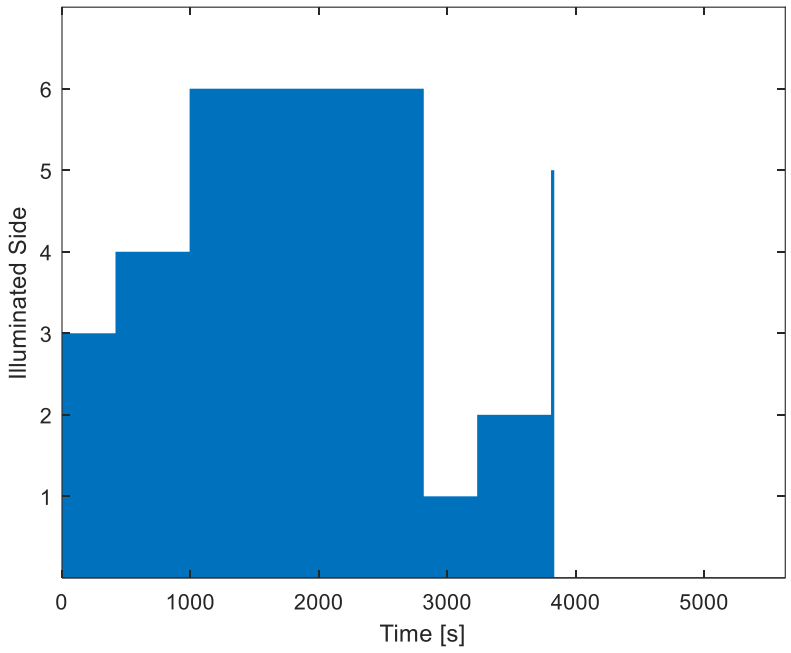
Illuminated Side
Time [s]
0
1000
2000
3000
4000
5000
1
2
3
4
5
6

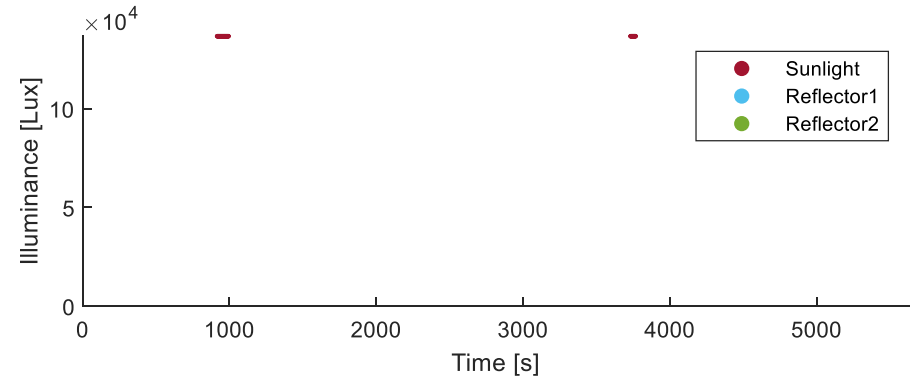
×10^4
Illuminance [Lux]
Time [s]
Sunlight
Reflector1
Reflector2
0
5
10

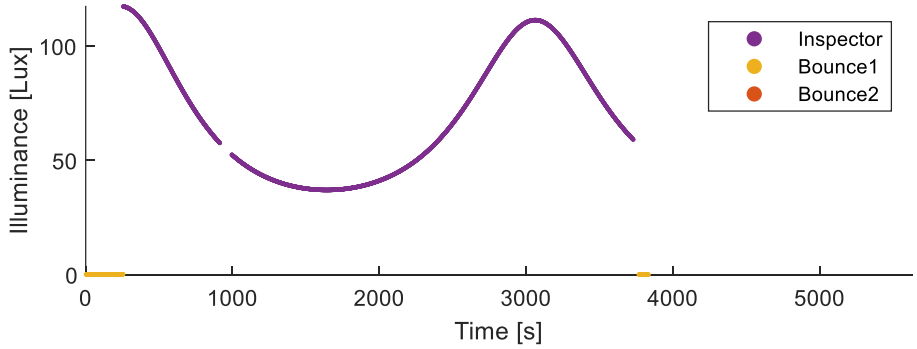
Illuminance [Lux]
Time [s]
Inspector
Bounce1
Bounce2
0
50
100

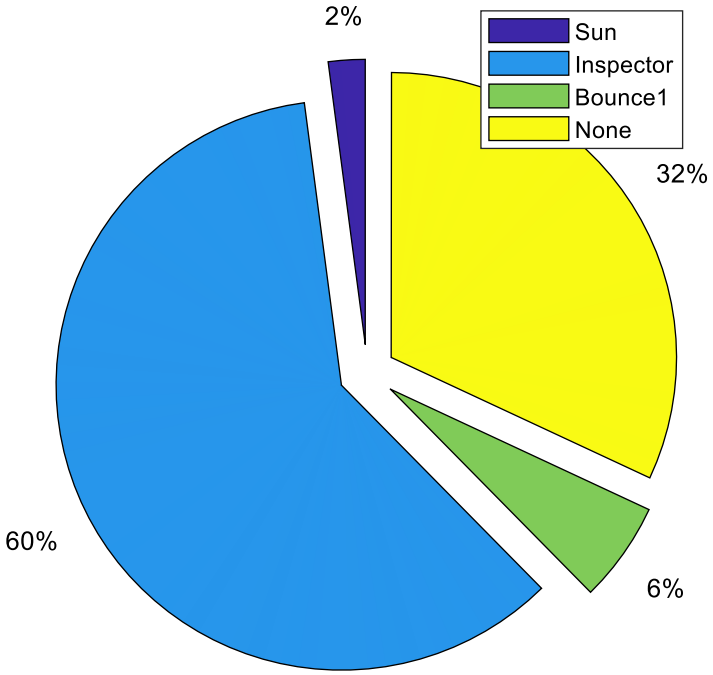
2%
Sun
Inspector
Bounce1
None
32%
60%
6%

Trial 4:

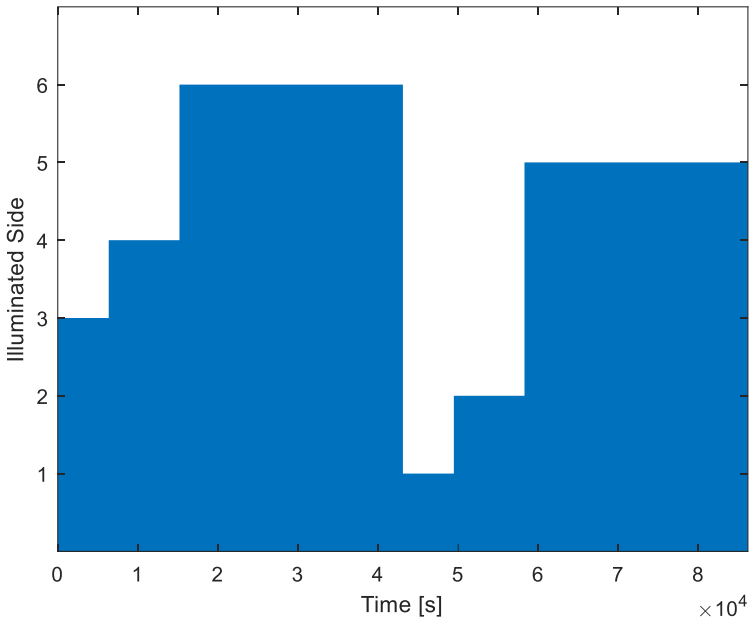
Illuminated Side
Time [s]
×10^4

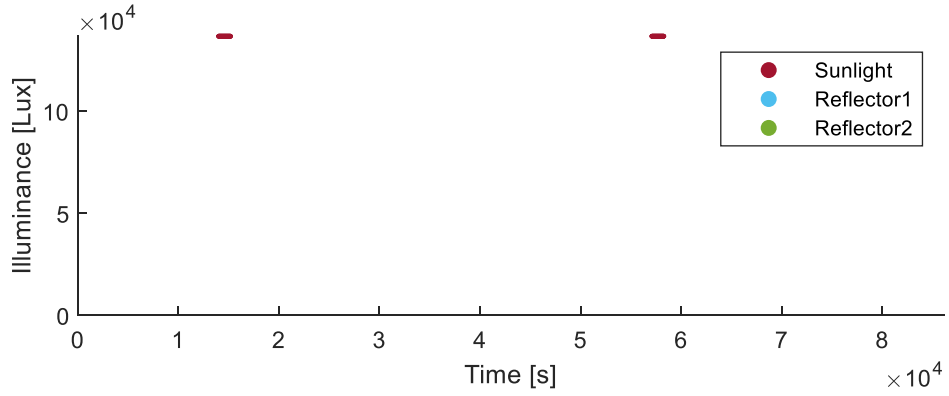
Illuminance [Lux]
Time [s]
×10^4
Sunlight
Reflector1
Reflector2

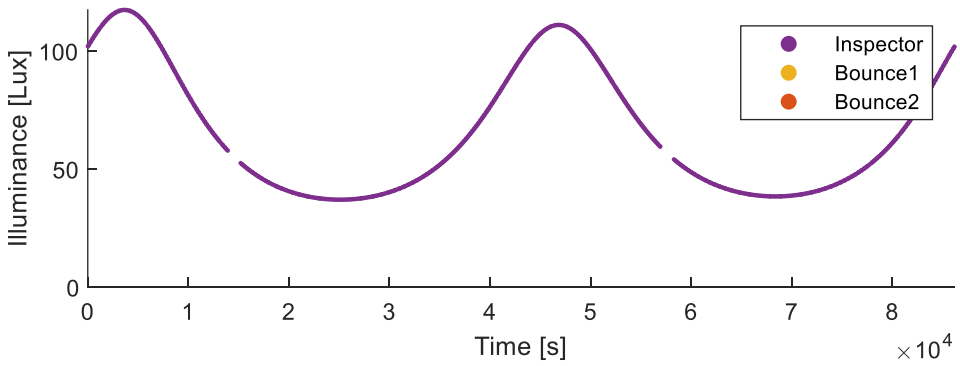
Illuminance [Lux]
Time [s]
×10^4
Inspector
Bounce1
Bounce2

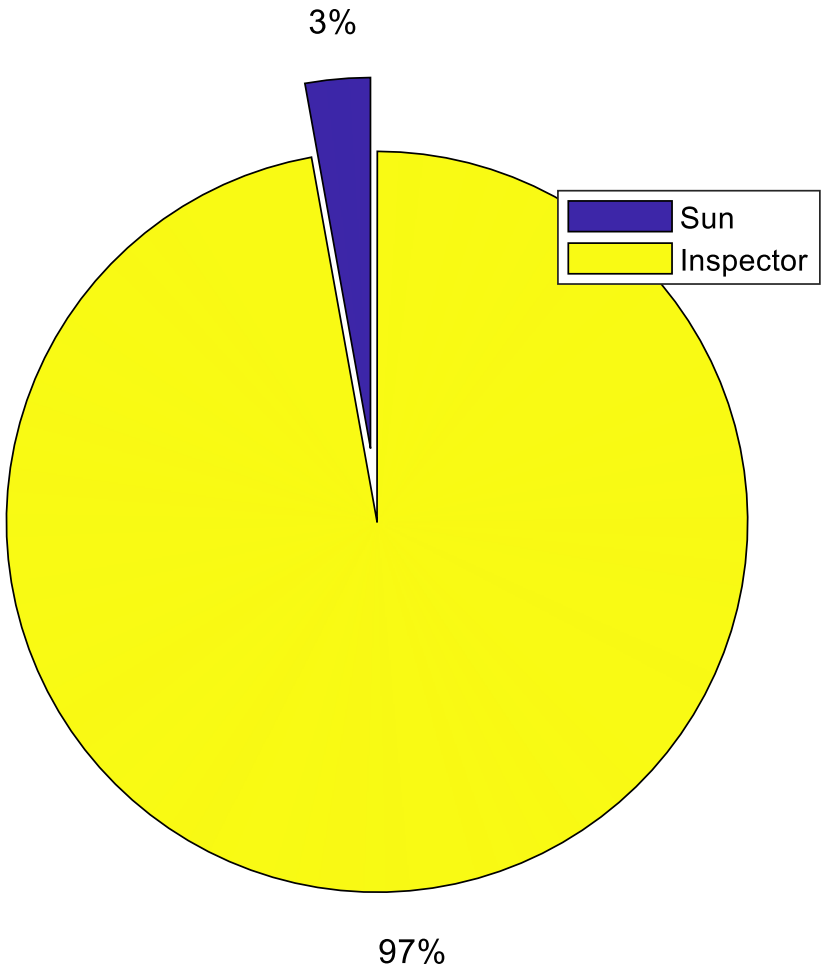
3%
Sun
Inspector
97%

Trial 5:

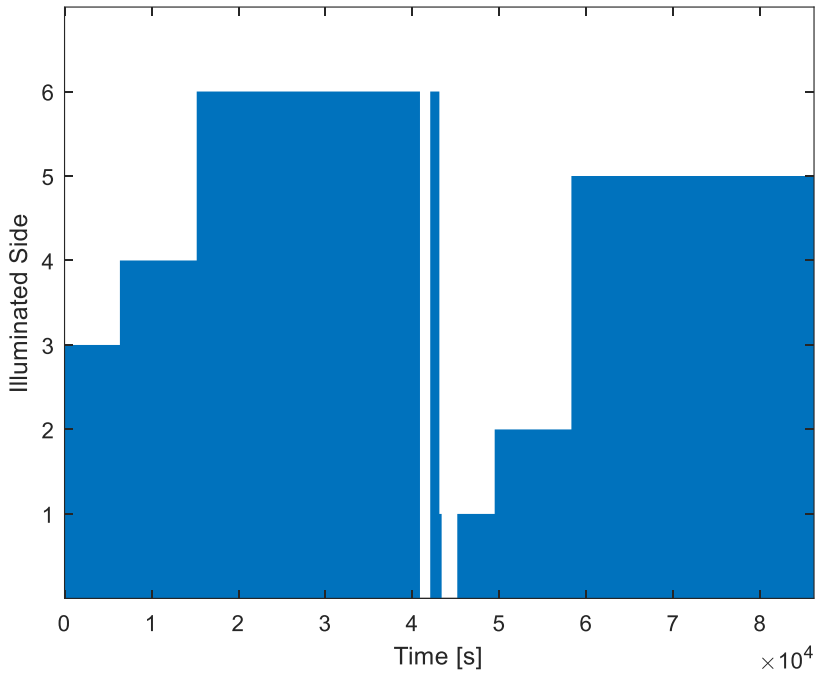
Illuminated Side
Time [s]
×10^4

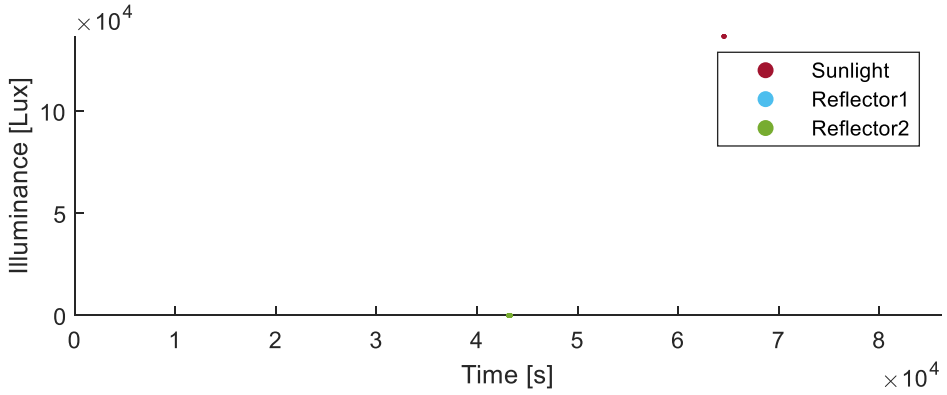
Illuminance [Lux]
×10^4
Sunlight
Reflector1
Reflector2
Time [s]
×10^4

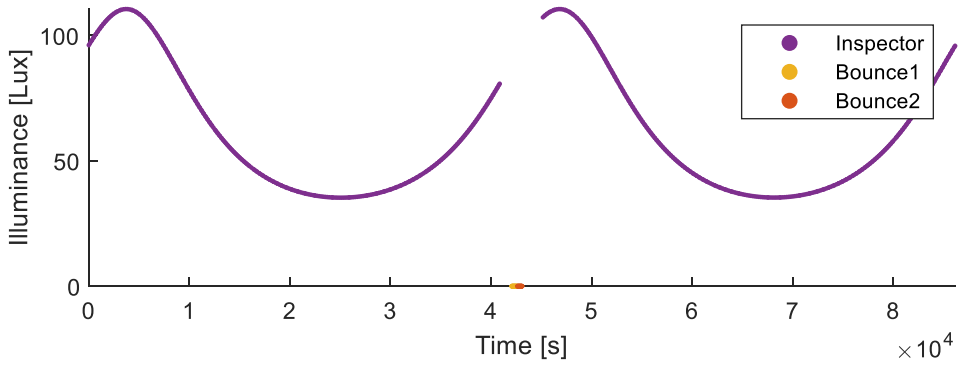
Illuminance [Lux]
Inspector
Bounce1
Bounce2
Time [s]
×10^4

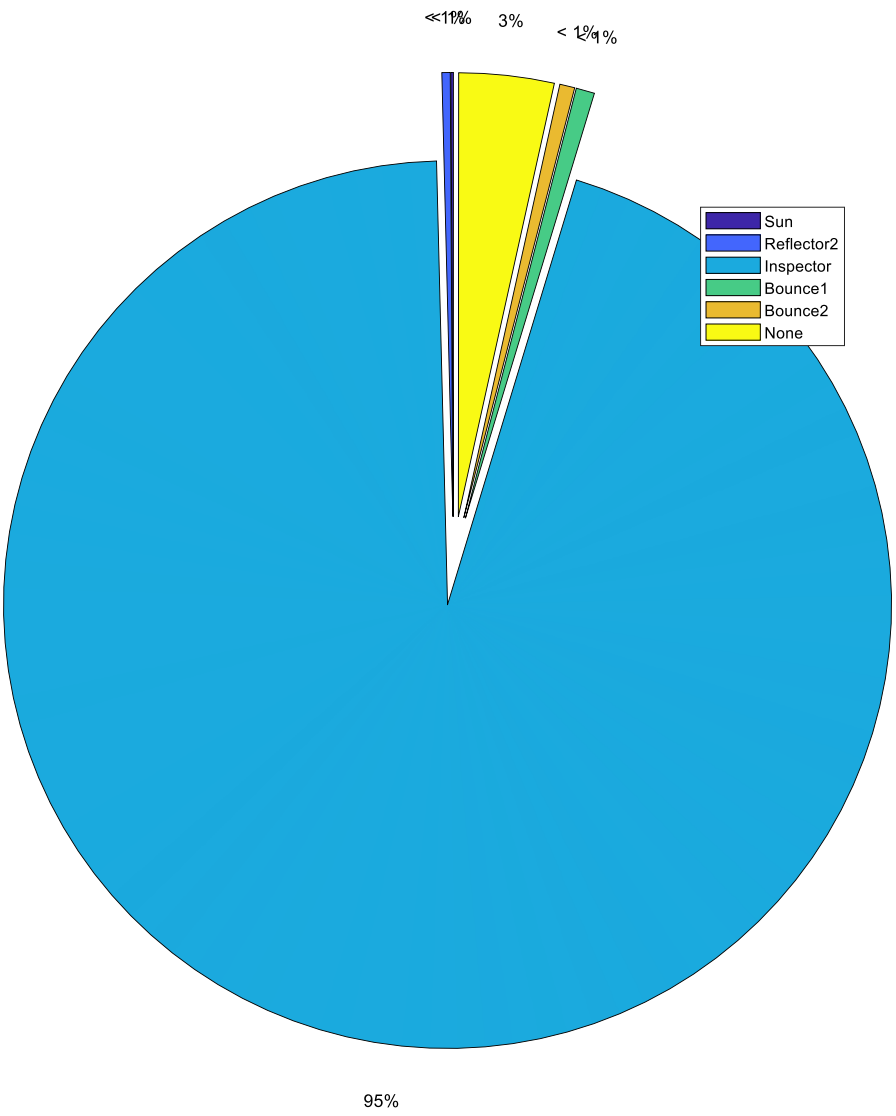
Sun
Reflector2
Inspector
Bounce1
Bounce2
None
95%

Appendix C: Which Side Logic Code

Contents


```
function [SideNumber] = WhichSide(VectorFromTargetToLightSource,DCM_fromIJK_toLVLH)
```

This function determines which side an illumination source is shining upon. Inputs are the vector from the target to that source and the DCM from the inertial frame to the chief's LVLH frame.

Ensure Collumn Vector

```
if ~iscolumn(VectorFromTargetToLightSource)
    VectorFromTargetToLightSource = VectorFromTargetToLightSource';
end
```

Unit vector between target and illuminator

```
sunVec.targettoILLUMINATORHat_LVLH = DCM_fromIJK_toLVLH*VectorFromTargetToLightSource;
```

Get angles between basis vector and 2D vector

```
if vecnorm(sunVec.targettoILLUMINATORHat_LVLH(1:2,1))<10^(-4)
    angle1 = 0;
else
    angle1 = atan2(sunVec.targettoILLUMINATORHat_LVLH(2),sunVec.targettoILLUMINATORHat_LVLH(1)); % XY angle
end

if vecnorm(sunVec.targettoILLUMINATORHat_LVLH(1:2:3,1))<10^(-4)
    angle2 = 0;
else
    angle2 = atan2(sunVec.targettoILLUMINATORHat_LVLH(3),sunVec.targettoILLUMINATORHat_LVLH(1)); % XZ angle
end
```

Ensure wrapped correctly

```
angle1 = wrapTo2Pi(angle1);
angle2 = wrapTo2Pi(angle2);
```

LOGIC

```
if (angle1>= 3*pi/4 && angle1 <= 5*pi/4) && ((angle2<=pi/4 || angle2>=7*pi/4) || (angle2>=3*pi/4 && angle2<=5*pi/4))
    SideNumber = 1; % Which side is illuminated
elseif (angle1> pi/4 && angle1 < 3*pi/4) && ((angle2<pi/4 || angle2>7*pi/4) || (angle2>3*pi/4 && angle2<5*pi/4))
    SideNumber = 2; % Which side is illuminated
elseif (angle1<=pi/4 || angle1>=7*pi/4) && ((angle2<=pi/4 || angle2>=7*pi/4) || (angle2>=3*pi/4 && angle2<=5*pi/4))
    SideNumber = 3; % Which side is illuminated
elseif (angle1>5*pi/4 && angle1<7*pi/4) && ((angle2<pi/4 || angle2>7*pi/4) || (angle2>3*pi/4 && angle2<5*pi/4))
    SideNumber = 4; % Which side is illuminated
elseif angle2>pi/4 && angle2<3*pi/4
    SideNumber = 5; % Which side is illuminated
elseif angle2>5*pi/4 && angle2<7*pi/4
    SideNumber = 6; % Which side is illuminated
else
    SideNumber = 'BROCKEN'; % Catch any errors, should ever be used due to all incluse logic statements
end
```

Published with MATLAB® R2020b

Appendix D: Is a Point Inside a Conical Shadow Code

Contents


```
function [outputstatement] = is_Point_X_in_Shadow_of_Y(X_vector,Y_vector,Y_radius,shadowAngle,VectorFromYtoSunHat)
```

This function determines if a point is in the conical shadow (i.e. umbral or (inclusive) penumbral shadow) of another spherical object. Inputs are the inertial position of object X inertial position of object Y the radius of Y the angle of divergenc of the light source the vector from point Y to the light source Outputs are a binary yes, no statement

Author: 2Lt Dan Dombrowski, AFIT ENY, October 2021

Ensure Collumn Vectors

```
if ~iscolumn(X_vector)
    X_vector = X_vector';
end
if ~iscolumn(Y_vector)
    Y_vector = Y_vector';
end
if ~iscolumn(VectorFromYtoSunHat)
    VectorFromYtoSunHat = VectorFromYtoSunHat';
end
```

Define Cone

```
cone.tip = (Y_radius/tan(shadowAngle)).*VectorFromYtoSunHat + Y_vector;
cone.dist = dot(X_vector-cone.tip,-VectorFromYtoSunHat);
```

Figure out if point X is in the cone of Y

```
if cone.dist > Y_radius/tan(shadowAngle)
    cone.radius = cone.dist*tan(shadowAngle);
    orthdistance = vecnorm(X_vector-cone.tip - cone.dist.*-VectorFromYtoSunHat);

    is_pt_inside_cone = (orthdistance<cone.radius);
    if is_pt_inside_cone == 1
        outputstatement = 'Dark'; % Shadow
    else
         outputstatement = 'Light'; % No shadow
    end
else
     outputstatement = 'Light'; % No shadow
end
```

```
end
```


Published with MATLAB® R2020b

Appendix E: Poster Presented at 14th Wernher von Braun Symposium

AFIT Air Force Institute of Technology

14th Wernher von Braun Memorial Symposium

American Astronautical Society

Preliminary Orbit Determination Using the Transit of Satellites in Front of Space-Based Illumination Sources

Daniel M. Dombrowski, Masters Student – Air Force Institute of Technology, Department of Aeronautics and Astronautics
Robert A. Bettinger, Ph.D., Faculty – Air Force Institute of Technology, Department of Aeronautics and Astronautics

Introduction

~ This research investigates a novel method of orbit determination through solution of a reverse occultation problem
~ Technique evolved from U.S. and Russian solar reflector research from 1960-2000
~ Objects passing in front of nadir pointing solar reflectors cast shadows onto Earth's surface
~ The absence of energy in these shadows contains pose information about the object causing the occultation

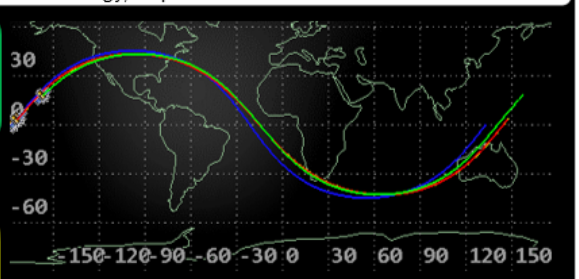

Geometry Technique

~ Computer vision techniques are used to analyze an input video frame and identify any shadows
~ The altitude of the RSO can be calculated using the semimajor axis of the shadow ellipse and the angle of divergence of the light source
~ The vector from the shadow ellipse centroid to the RSO can then be found by simultaneously solving the equations below

$$cos(\beta - 90^0) = \frac{h}{L} \text{ and } \frac{a}{sin(\alpha)} = \frac{L}{sin(180^0 - \alpha - \beta)} \text{ for } L \text{ and } \beta$$

$$\rho = \sqrt{a^2 + L^2 - 2aL\cos(\beta)}$$

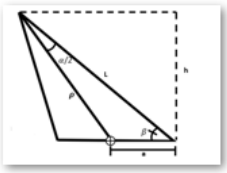

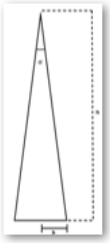

~ R can then be calculated using the known position of the illuminator, the shadow centroid's location in the 2D frame, and the calculated values
~ Noise is then filtered and reference frame rotations are applied to bring R into the inertial reference frame
~ V is then calculated using any number of traditional techniques such as Gibbs, Herrick-Gibbs, or any number of Lambert's problem solution techniques

Computer Vision Technique

~ Color image converted to greyscale
~ Otsu's thresholding algorithm is used to turn greyscale image to binary
~ Noise is filtered out using expected shadow size parameters
~ Having only the target RSO shadow remaining the ellipse semimajor, semiminor, and centroid dimensions are recorded for use in the IOD method

Original Color Image

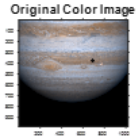

Grey Scale Image

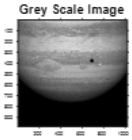

Binary Image

Binary Image (inverted)

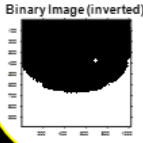

Binary Image w/Noise

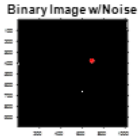

Final Binary Image

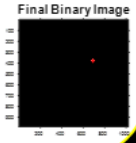

Testing and Key Findings

~ Method tested against three main trials of 25 tests each, varying the semimajor axis, eccentricity, and inclination

~ Accurate position estimate at point of observation
Current work is solely deterministic, could greatly benefit from statistical or state estimation techniques for more accurate velocity estimation

~ Circular assumption most accurately models orbital shape parameters

~ Linear and Herrick-Gibbs method most accurately models angular initial position

~ Current results retain a significant degree of error but show great promise for further development through short-arc, high data density techniques

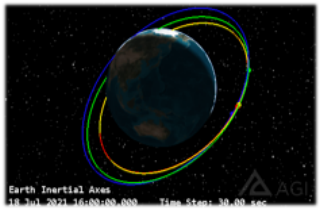

Impact and Applications

~ Conventional techniques involving visual observations (angles-only techniques) or radar (range-range rate techniques) have inherent ambiguities in determining the inertial position of the RSO

~ This novel technique does away with these ambiguities and provides a deterministic inertial position directly from shadow parameters

~ This method can overcome the inadequate results of traditional observation methods when combating environmental effects or non-cooperative targets

~ Low computational load solution to IOD problem

~ Allows tracking of multiple objects at once improving SSA in an increasingly congested and contested space environment

~ Can be utilized as an on-board position estimation technique for deep-space or interplanetary missions utilizing local planet solar eclipse

~ Novel modern missions, such as power beaming or solar reflectors, are already providing the energy point sources required, allowing these missions to be dual use

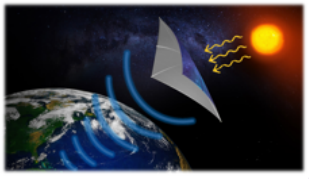

~ Further development has potential to yield a full pose estimation technique

U.S. AIR FORCE

Acknowledgements
Special thanks given to:
The Air Force Institute of Technology
The Center for Space Research and Assurance

Center for Space Research & Assurance AFIT

Bibliography

[1] NASA Office of Communications, "NASA Image and Video Library," 28 July 2005. [Online]. Available: https://images.nasa.gov/details-iss011e11029. [Accessed 19 October 2021].

[2] T. Carrico, T. Langster, J. Carrico, D. Vallado, M. Loucks and S. Alfano, "Proximity Operations for Space Situational Awareness".

[3] DARPA, "Orbital Express," Defense Advanced Research Projects Agency, [Online]. Available: www.darpa.mil/about-us/timeline/orbital-express.. [Accessed 29 September 2021].

[4] C. J. Dennehy and J. R. Carpenter , "A Summary of the Rendezvous, Proximity Operations, Docking, and Undocking (RPODU) Lessons Learned from the Defense Advanced Research Project Agency (DARPA) Orbital Express (OE) Demonstration System Mission," NASA, 2011.

[5] A. G. Buckingham and H. M. Watson, "Basic Concepts of Orbiting Reflectors," *Journal of Spacecraft and Rockets,* vol. 5, pp. 851-854, 1968.

[6] J. E. Canaday and J. L. Allen, "Illumination from Space with Orbiting Solar-Reflector Spacecraft," NASA, 1982.

[7] L. M. Fraas, "Mirrors in Space for Low-Cost Terrestrial Solar Electric Power at Night," in *38th IEEE Photovoltaic Specialists Conference*, 2012.

[8] L. M. Fraas, G. A. Landis and A. Palisoc, "Mirror Satellites in Polar Orbit Beaming Sunlight to Terrestrial Solar Fields at Dawn and Dusk," in *IEEE 39th Photovoltaic Specialists Conference*, 2013.

[9] J. M. Hedgepeth, R. K. Miller and K. Knapp, "Conceptual Design Studies for Large Free-Flying Solar-Reflector Spacecraft," NASA, 1981.

[10] N. Lior, "Mirrors in the Sky: Status, Sustainability, and Some Supporting Materials Experiments," *Renewable and Sustainable Energy Reviews,* vol. 18, pp. 401-415, 2013.

[11] C. Garner, B. Diedrich and M. Leipold, "A Summary for Solar Sail Technology Developments and Proposed Demonstration Missions," NASA, 1999.

[12] V. Syromiatnikov, "General Information," Space Regatta Consortium, [Online]. Available: www.old.space-regatta.ru/page_30e.htm. [Accessed 2 October 2021].

[13] R. Garner, "Hubble Space Telescope Observatory - Optics," NASA, 19 December 2017. [Online]. Available: www.nasa.gov/content/goddard/hubble-space-telescope-optics-system. [Accessed 2 October 2021].

[14] "JWST – Technical Details," Northrop Grumman, 7 May 2020. [Online]. Available: www.northropgrumman.com/space/jwst-technical-details/. [Accessed 2 October 2021].

[15] "James Webb Space Telescope," NASA, [Online]. Available: www.jwst.nasa.gov/. [Accessed 2 October 2021].

[16] Space Telescope Science Institute, "NASA's James Webb Space Telescope: Optics," [Online]. Available: www.stsci.edu/files/live/sites/www/files/home/jwst/about/history/flyers/_documents/JWST-Optics.pdf. [Accessed 2 October 2021].

[17] M. Ulmer, "Further Development of Aperture," NASA, 10 May 2016. [Online]. Available: www.nasa.gov/feature/further-development-of-aperture-a-precise-extremely-large-reflective-telescope-using-re/. [Accessed 2 October 2021].

[18] Pi Piezotechnology, "DuraAct - Piezoelectric Patch Transducers Industry and Research," [Online]. Available: https://www.pi-usa.us/fileadmin/user_upload/pi_us/files/catalogs/PI_Catalog_DuraAct_Piezo_Patch_Transducer_Piezo_Composite_C1.pdf. [Accessed 4 Nov 2021].

[19] M. P. Ulmer, V. L. Coverstone, J. Cao, Y. W. Chung, M. C. Corbineau, A. Case, B. Murchison, C. Lorenz, G. Luo, J. Pekosh, J. Sepulveda, A. Schneider, X. Yan and S. Ye, "APERTURE, A Large Telescope Using Magnetostriction for Post Deployment Corrections," NASA, 2016.

[20] M. Ulmer, "Aperture: A Precise Extremely large Reflective Telescope Using Re-configurable Elements," 7 May 2015. [Online]. Available: https://www.nasa.gov/feature/aperture-a-precise-extremely-large-reflective-telescope-using-re-configurable-elements/. [Accessed 2 October 2021].

[21] R. M. Fitzgerald, "Autonomous Spacecraft Orbit Determination from Incident Light Intensity via Eclipse Transient Timing," *Journal of Guidance Control Dynamics,* vol. 44, no. 9, pp. 1621-1637, 2021.

[22] "What Is an Occultation?," International Occultation Timing Association, 30 January 2021. [Online]. Available: occultations.org/occultations/what-is-an-occultation/.. [Accessed 2 October 2021].

[23] M. W. Buie and et. al., "Size and Shape Constraints of (486958) Arrokoth from Stellar Occultations," *The Astronomical Journal,* vol. 159, no. 4, 2020.

[24] D. A. Vallado and W. D. McClain, Fundamentals of Astrodynamics and Applications, 4th ed., Microcosm Press, 2013.

[25] J. e. a. Choi, "Characteristics of Orbit Determination with Short-Arc Observation by an Optical Tracking Network, OWL-Net," *International Journal of Aerospace Engineering,* pp. 1-11, 2018.

[26] D. A. Vallado and S. S. Carter, "Accurate Orbit Determination from Short-Arc Dense Observational Data," *The Journal of the Astronautical Sciences,* vol. 46, no. 2, pp. 195-213, 1998.

[27] P. Schlyter, "Radiometry and photometry in astronomy," 05 March 2017. [Online]. Available: http://stjarnhimlen.se/comp/radfaq.html#10. [Accessed 13 10 2021].

[28] A. Pears, "A Report for Environment Australia," Sustainable Solutions Pty Ltd , Brighton, 1998.

[29] Occupational Safety and Health Administration, US Dept of Labor, "Illumination - 1926.56 Regulations (Standards - 29 CFR)," 2009.

[30] D. D. MacInnis, P. B. Williamson and G. P. Nielsen, "Sun Position and Twilight Times for Driver Visibility Assessment," *Journal of Passenger Cars,* vol. 104, no. 6, pp. 759-783, 1995.

[31] Aerospace Corporation, "CubeSats Get Close: Proximity Operation with Interesting Implications," 22 July 2020. [Online]. Available: https://aerospace.org/article/cubesats-get-close-proximity-operation-interesting-implications. [Accessed 2 11 2021].

[32] K. T. Alfriend, S. R. Vadali, P. Gurfil, J. P. How and L. S. Breger, Spacecraft Formation Flying: Dynamics, Control and Navigation, Butterworth-Heinemann, 2010.

[33] Apgar, Henry; et. al., Space Mission Engineering: The New SMAD, Torrance, CA: Micocosm Press, 2018.

[34] D. A. Vallado, "Astrodynamics Software by David Vallado," CelesTrak, 18 November 2020. [Online]. Available: celestrak.com/software/vallado-sw.php. [Accessed 3 October 2021].

[35] N. Otsu, "A Threshold Selection Method from Gray-Level Histograms," *IEEE Transactions on Systems, Man, and Cybernetics,* vol. 9, no. 1, pp. 62-66, 1979.

[36] "Io in Front of Jupiter," NASA: Jet Propulsion Laboratory: California Institute of Technology, 20 December 2000. [Online]. Available: https://www.jpl.nasa.gov/images/io-in-front-of-jupiter. [Accessed 3 October 2021].

[37] MathWorks Help Center, "How Is a Moving Average Filter Different from an FIR Filter?," MathWorks, [Online]. Available: https://www.mathworks.com/help/dsp/ug/how-is-moving-average-filter-different-from-an-fir-filter.html. [Accessed 3 October 2021].

[38] MathWorks Help Center, "Movmean," MathWorks, [Online]. Available: https://www.mathworks.com/help/matlab/ref/movmean.html. [Accessed 3 October 2021].

[39] Air Force Research Laboratory, United States Air Force, [Online]. Available: https://afresearchlab.com/technology/space-power-beaming/. [Accessed 4 11 2021].

[41] "CelesTrak," [Online]. Available: http://www.celestrak.com/Norad/elements/table.php?tleFile=science&title=Space%20%26%20Earth%20Science%20Satellites&orbits=0&pointsPerRev=90&frame=1. [Accessed 12 10 2021].

[42] Patent Dombrowski, D. M., Bettinger, R. A., "Spacecraft Orbit Determination System," AFD-2224, U.S. Provisional Patent No. 17/467,548, September 2021..

[43] "Dombrowski, D. M.; Bettinger R. A., "Preliminary Orbit Determination Using the Transit of Satellites in Front of Space-Based Illumination Sources," 2021 Advanced Maui Optical and Space Surveillance Technologies Conference (AMOS), Maui, HI, September 2021.".

[44] "Dombrowski, D. M.; Bettinger, R. A., "Preliminary Orbit Determination Using the Transit of Satellites in Front of Space-Based Illumination Sources," 46th AIAA Dayton-Cincinnati Aerospace Sciences Symposium (DCASS), Dayton, OH, March 2021.".

[45] "Dombrowski, D. M., Bettinger, R. A., "Investigation of Mirror Satellite Concept to Provide Augmented Lighting for Dim Space-Based Objects," 2022 IEEE Aerospace Conference, Big Sky, MT, March 2022.".

[46] "Dombrowski, D. M., Bettinger, R. A., "Preliminary Orbit Determination Using the Transit of Satellites in Front of Space-Based Illumination Sources," 14th AAS Wernher von Braun Memorial Symposium, Huntsville, AL, October 2021.".

Vita Section

2nd Lieutenant Daniel M. Dombrowski graduated high school in 2016 and received an appointment to the United States Air Force Academy. At the Academy, Lt Dombrowski earned a Bachelor of Science degree in Astronautical Engineering. In the process Lt Dombrowski performed interagency research with the Department of Homeland Security and the Department of Defense on anomaly tracking in ground-based midcourse ballistic missile defense assets. He also worked with the FalconSat program working with ground operations for FalconSat-6, integration for launch of FalconSat-8, and radiation tolerance research and design for FalconSat-X. In addition to a heavy course load, Lt Dombrowski created time to enjoy airmanship activities, volunteering numerous hours as a glider instructor pilot and completing the basic freefall parachuting course.

After commissioning, Lt Dombrowski's first assignment was to the Graduate School of Engineering and Management at the Air Force Institute of Technology (AFIT). In addition to earning his graduate degree Lt Dombrowski also earned his civilian Commercial Pilot-Glider rating as well as his Certified Flight Instructor-Glider and volunteered many hours as an instructor at a local soaring club. Following completion of the Astronautical Engineering Master's program he will be attending Undergraduate Pilot Training at Laughlin AFB, Texas.

REPORT DOCUMENTATION PAGE

Form Approved
OMB No. 074-0188

1. REPORT DATE *(DD-MM-YYYY)*	2. REPORT TYPE	3. DATES COVERED *(From – To)*
23 Dec 2021	Master's Thesis	July 2020 – December 2021

TITLE AND SUBTITLE

Investigation of Mirror Satellite Concept to Augment Natural Lighting Conditions on Orbit

5a. CONTRACT NUMBER N/A
5b. GRANT NUMBER N/A
5c. PROGRAM ELEMENT NUMBER N/A

6. AUTHOR(S)

Dombrowski, Daniel M., Second Lieutenant, USAF

5d. PROJECT NUMBER N/A
5e. TASK NUMBER N/A
5f. WORK UNIT NUMBER N/A

7. PERFORMING ORGANIZATION NAMES(S) AND ADDRESS(S)
Air Force Institute of Technology
Graduate School of Engineering and Management (AFIT/ENY)
2950 Hobson Way, Building 640
WPAFB OH 45433-8865

8. PERFORMING ORGANIZATION REPORT NUMBER
AFIT-ENY-MS-21-D-065

9. SPONSORING/MONITORING AGENCY NAME(S) AND ADDRESS(ES)

Intentionally Left Blank

10. SPONSOR/MONITOR'S ACRONYM(S) N/A
11. SPONSOR/MONITOR'S REPORT NUMBER(S) N/A

12. DISTRIBUTION/AVAILABILITY STATEMENT
Distribution A: Approved for Public Release; Distribution Unlimited

13. SUPPLEMENTARY NOTES
The material is declared a work of the U.S. Government and is not subject to copyright protection in the United States

14. ABSTRACT
A method of augmenting on-orbit lighting conditions for rendezvous and proximity operations through the novel use of solar reflectors is presented. Natural lighting conditions on-orbit pose extreme challenges to these already complex missions. This research summarizes and applies the historical basis of solar reflectors to the proximity operations issues encountered today. Building on this past research, a simulation has been created to test the efficacy of a solar reflector constellation in facilitating less complex servicing/inspection missions. Initial testing has shown promising results for low mass membrane mirrors in augmenting illumination conditions with particular benefit in the geosynchronous orbital regime. Through the course of this research a novel method of initial orbit determination has also been developed. By observing the shadow of a RSO projected onto the surface of the Earth or a similar body, the inertial position vector of the RSO can be calculated analytically. A computer vision-based program was created and tested to examine the accuracy and applicability of this method. Initial results are promising; however, significant further work must be accomplished to filter and weight measurements.

15. SUBJECT TERMS
solar reflectors, mirrors; proximity operations, initial orbit determination, satellite navigation, inspection, spacecraft servicing

16. SECURITY CLASSIFICATION OF:			17. LIMITATION OF ABSTRACT	18. NUMBER OF PAGES	19a. NAME OF RESPONSIBLE PERSON
a. REPORT	b. ABSTRACT	c. THIS PAGE			Robert A. Bettinger, Ph.D, Maj (Advisor)
FOUO	UU	UU	UU	134	19b. TELEPHONE NUMBER *(Include area code)* (937) 255-6565, ext. 4578 (Robert.Bettinger@afit.edu)